A study on effects of geometry on internal ballistics of multiple BATES grain Solid Rocket Motors

Thesis Report

J.A.B.J. van den Wijngaart

Technische Universiteit Delft

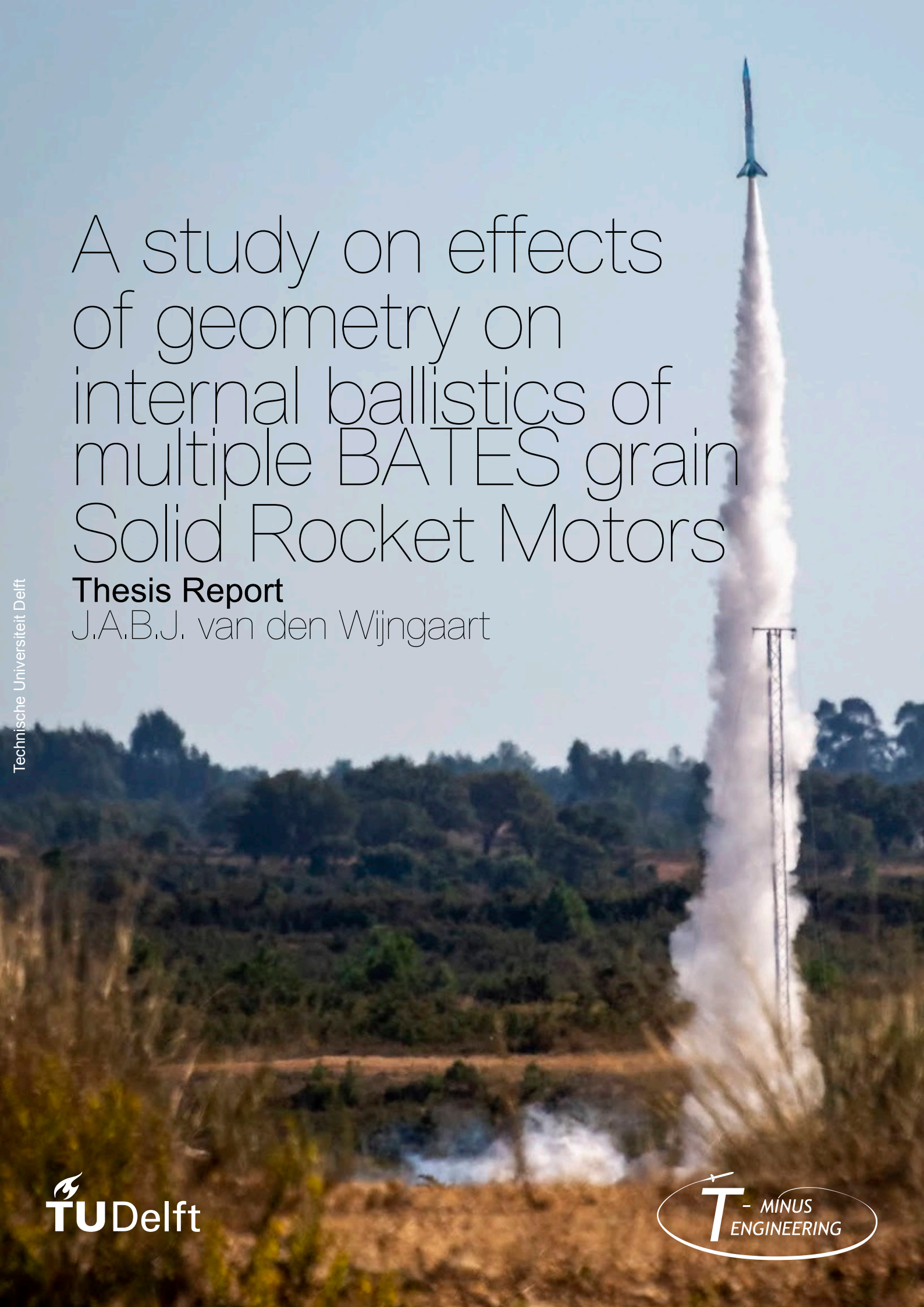

TU Delft

T- MINUS ENGINEERING

A study on effects of geometry on internal ballistics of multiple BATES grain Solid Rocket Motors

Thesis Report

by

J.A.B.J. van den Wijngaart

at the Delft University of Technology,

Student number: 4440463

Thesis committee:

Prof. Dr. A. (Arvind) Gangoli Rao,	Chair	TUDelft
Dr. B.V.S. (Botchu) Jyoti,	External examinator	TUDelft
Dr. G.A. (Alexis) Bohlin,	Responsible supervisor	TU Delft and LTU
H.W. (Hein) Olthof, MSc. ,	External supervisor	T-Minus Engineering B.V.

This thesis is confidential and cannot be made public until June 29th, 2024.

Title cover image courtesy of Nathaniel P. Stebbins Dahl

TU Delft

T- MINUS ENGINEERING

Version Log

Author	Description	Version	Date
Jeije van den Wijngaart	First draft	1	15th of May, 2022
Jeije van den Wijngaart	Second draft after green light meeting	2	8th of June, 2022
Jeije van den Wijngaart	Final version	3	14th of June, 2022

Date of download: June 25, 2022
Version: 3

Preface

Solid rocket motor design is the art of finding the balance between a smoke bomb and a pipe bomb. This has become very clear for me during the last few years. In 2016 I started working on Solid Rocket Motors in Delft Aerospace Rocket Engineering (DARE) and this immediately sparked a passion for rockets and their motors. During this time I developed and tested motors successfully, but also had multiple explosion leaning slightly too far toward the pipe bomb. These explosions had a higher than expected operating pressure, sometimes due to poor propellant batches, but also due to erosive burning. I learened quickly that a high core velocity can increase the burn rate significantly. During my further academic development in my master the lectures on combustion made me wonder what the mechanism behind erosive burning was, which escalated in a preliminary proposal to Hein at T-Minus Engineering and Alexis at the TUDelft.

The initial ambition of developing a physics based model for erosive burning was relatively quickly abandoned during my literature study and so was applying laser diagnostics, the research field of Alexis, to the propellant surface due to practical issues and resource limitations. Eventually coming to the effects of internal geometry due to questions on changing the amount of grains in the DART motor. Originally this would only include modelling work using test data from previous motor tests as validation data, however, I found it incredibly hard not to do any experiments. I found during my time in DARE, but also during my internship at RFA that I have a particular taste for testing rocket engines. This resulted in including a low-cost minimum invasion test technique on some DART booster tests aimed to give valuable validation data with multiple measurement locations along the length of the motor. In the end the whole project took longer than expected, which in general is true about my entire Bachelor and Master at the TUDelft. I would mostly want to blame this on the great time I had designing and launching rockets at DARE.Even during my thesis project I designed, build and tested a rocket. Then I went to Portugal with a team to participate at the European Rocket Challenge with this rocket, which can be seen on the cover of this document.

I want to thank some people that helped me along this road starting with the previously already mentioned Alexis Bohlin and Hein Olthof who have guided me in the academic and solid propellant world respectively with helpful discussions and giving inspiration. The colleagues at T-Minus Engineering helping with help during tests, programming and wonderful lunch/coffee breaks. To my girlfriend, my family and friends listening to me complaining about thesis and helping to proofread. These past 7 years of studying I could not have done without all this help.

Jeije van den Wijngaart
Delft, June 2022

Abstract

Solid rocket motors provide access to the upper atmosphere by providing impulse to sounding rockets that sense the atmosphere in the gap between weather balloons and satellites. The thrust provided by solid rocket motors is determined mostly by their internal geometry. BATES grains are propellant segments shaped like thick-walled cylinders which burn from the inside, the top, and the bottom. BATES grains are used due to their ease of production and development and can easily be designed to have a near-constant pressure during their burn. Due to considerations of drag and total impulse for sounding rockets, solid rocket motors tend to be slender.

Slender rocket motors which are long with respect to their diameter generally experience erosive burning. Erosive burning is a longitudinal effect and changes the burn rate in different places along the length of the motor. It augments the burn rate at the propellant surface by increasing the heat feedback to the surface which causes the propellant surface to regress faster and more gas to be produced. The increase in heat feedback is generally agreed upon to be caused by an increase in turbulence due to high mass flux which increases mixing in the diffusion flames in the flame front.

Multiple BATES grain motors can be easily modified due to their modular nature. In order to be able to leverage this advantage first the effect of changing the internal geometry must be known. Given that most solid rocket motor models are not validated with test data of multiple BATES grains and are not freely available a goal was set to develop a model considering especially longitudinal variation.

There is an absence of validation data for multiple BATES grains with multiple locations along the length. This does traditionally require purpose-built test hardware, which induces extra costs and risks. Therefore, it was set out to acquire validation data at multiple stations along the length of the motor without changing the motor design with strain gauges.

Tests were done with four strain gauges placed along the length of the motor. The data of these tests showed good agreement with the reference pressure sensor at ambient temperatures, however, when the surface temperature of the combustion chamber started to increase the signal started drifting to values corresponding to compression. The temperature was recorded to compensate but no clear relation was present. Higher frequency changes in pressure could still be recognised in time, suggesting local effects or anomalies can be located and identified. The method was useful to find the amplitude of the pressure drop during the 0.5 seconds of the burn when the chamber surface did not change in temperature yet finding a pressure drop of the initial peak of 10% at 77% of the length of the motor. However, the method still needs further research to compensate for the changing temperature of the chamber and could not be used as validation data for the model.

Instead for this study the pressure data at the forward closure of the DART booster of T-Minus Engineering B.V. is used to validate the developed model, this is deemed sufficient as the model uses constant pressure over the length of the chamber. The developed model is a quasi-one-dimensional model that is governed by one state variable and derives the mass flow from the location of gas creation assuming steady flow for each time step. The grain burn-back model considers burning in two dimensions as asymmetry is assumed during the burn. An erosive burning model using mass flux derived from the mass flow and port area from the grain burn-back model determines the erosive burning augmentation on the normal propellant regression mainly determined by pressure. When comparing the model results to the validation data it is deemed sufficiently accurate to validate it for the use of this study.

This study used the developed model to perform a sensitivity study on the changes in internal geometry by changing the aspect ratio, truncation, and elongation of grains in the DART motor, a multiple BATES grain solid rocket motor. This showed that very low aspect ratios tend to have very high pressures. A lower aspect ratio for a given amount of propellant increases the initial burning surface which increases the mass flux in the core of the motor and increases the burn rate modification due to erosive burning. Furthermore, it showed that when keeping the throat area constant, truncation and elongation has a big impact on both the peak and the mean operating pressure of the motor. Truncation

and elongation with constant throat do not impact the tail-off length significantly but do change the slope of the initial phase of the burn with a longer motor being more regressive. Lastly, when changing the throat area to keep the initial burning area to throat area ratio constant the mean pressure is nearly unaffected by changes in motor length but the peak pressure increases for longer motors due to their higher mass flow in the core leading to erosive burning.

For the DART booster, it is recommended to increase the aspect ratio of the grains from 4 to 4.5 to make the pressure trace slightly more progressive which would keep the chamber pressure constant during the majority of the burn. This would cause higher performance as most of the propellant burns at the higher more efficient pressure and make the burn-out shorter and more defined making the trajectory more predictable.

Contents

List of Figures

List of Tables

1

Introduction

Solid Rocket Motors (SRM) are used to power sounding rockets, providing access to the upper atmosphere which is otherwise inaccessible. Sounding rockets, which take their name from the nautical term “to sound”, meaning to take measurements, can take in-situ measurements in the upper atmosphere or mesosphere and (lower) thermosphere inaccessible to weather balloons or satellites. This region has unresolved discrepancies in climate research [1]. T-minus Engineering developed the DART, a low-cost rapidly deployable sounding rocket for research at altitudes between 50 and 120km filling the research gap. Motor development is usually time-consuming and resource-intensive. BATES (BAllistic TESt) grains are used to determine propellant performance. T-Minus Engineering decreased development time and production cost by using multiple BATES grains. The internal geometry determines the pressure curve and the thrust curve which determines the largest acting force on a rocket. Therefore, it is important to investigate the effects of internal geometry on multiple BATES grain motors to increase access to atmospheric research.

A sounding rocket needs to minimise drag while maximising the impulse gotten by its motor, this usually leads to a slender rocket with a long motor. The rocket motor for the DART rocket system is a booster of 118 [mm] diameter and a length of 2.3 [m] using an ammonium perchlorate aluminium composite propellant. Rocket motors with a high length over diameter experience erosive burning as the gasses in the combustion chamber move at a high velocity through the motor. The DART motor is considered to have a high L/D and therefore erosive burning plays a significant role. Erosive burning is the burn rate augmentation by the flow field due to an increase in turbulence[2]. This generally increases the speed at which propellant is consumed which increases combustion pressure. According to Kreidler [3] erosive burning can result in uneven burnout and possibly a damaged motor casing. This is why the effects of erosive burning need to be modelled when further optimising solid rocket motors by changing the grain aspect ratio or motor length.

A multiple BATES grain motor consists of a cylinder of propellant cut into segments. Both changes in aspect ratio and elongation and truncation are easy changes to make to a solid rocket motor. Therefore, the effect of these changes is relevant to optimise the thrust profile. These effects are not trivial due to the effect of erosive burning for motors with high mass flux in the core. Ideally, a fully unsteady one-dimensional model considering both ignition and erosive burning with high fidelity would be used. While some models are developed like SPP [4] and SPINBALL [5], [6], none are freely available and therefore require developing new models or adapting models available to the author. Therefore, it was decided to work towards an unsteady model considering ignition and erosive burning effects in one dimension that is validated for a multiple BATES grain motor.

The road towards this validated model contains both modelling work, and experimental work. The experimental path that was set out is focused on achieving a set of data on the pressure over the length of the motor. This must be done while making minimal intrusions to the motor casing to keep the motor as representable as possible giving an accurate result similar to the motor used for flight and while keeping the impact on budget and timeline to a minimum. The method aimed to be used

was earlier reported by Gudu et al.[7] using strain gauges placed along the motor to infer the static pressure in the combustion chamber. Figure 1.1 shows the steps required to develop this experimental method, starting with a verification test at ambient conditions using water to pressurise the casing. Then performing a hot fire test with the strain gauges attached while recording the temperature, and lastly performing a hot fire test with temperature compensation by using an active dummy gauge under no strain as a reference and a model accounting for the potential stiffness degradation of the motor.

The second path on the road map in Figure 1.1 shows the development steps of the model. This development can also be split up into two different parts, one part concerning the grain burn back and the other the gas flow. The grain burn back model started from an analytic model in zero-dimensions describing the burn area as a function of propellant distance burned. Then it progressed into the model used in this work, a two-dimensional model considering different regression over the length of the motor. This model does assume the geometry to stay axis-symmetric. The three-dimensional model does not make this assumption making it suitable for example star cores, however, this comes with an increased computational cost. SPP[8] is an example of a three-dimensional model. For a multiple BATES grain motor two dimensional with axis-symmetric burning is sufficient and less computationally expensive, therefore, a two-dimensional model is considered for this thesis.

The second part of the model concerns the gas flow, zero dimensions should be sufficient if homogeneous gas properties are assumed in the combustion chamber. This fails to consider erosive burning, in most models for erosive burning (see list of expressions by Radzan[9]) this requires at least the mass flux. Assuming steady flow this gas flow property can be gotten from a zero-dimensional model, which gives an approximation of the actual mass flux along the length of the motor. This was used to achieve a model that is computationally inexpensive, making it more suited for sensitivity studies. However, for motors with a higher volume, start-up transient would be less instantaneous and generate more errors when taking this approach. Therefore the end goal of the road map would be to implement a model using a one-dimensional gas flow simulation.

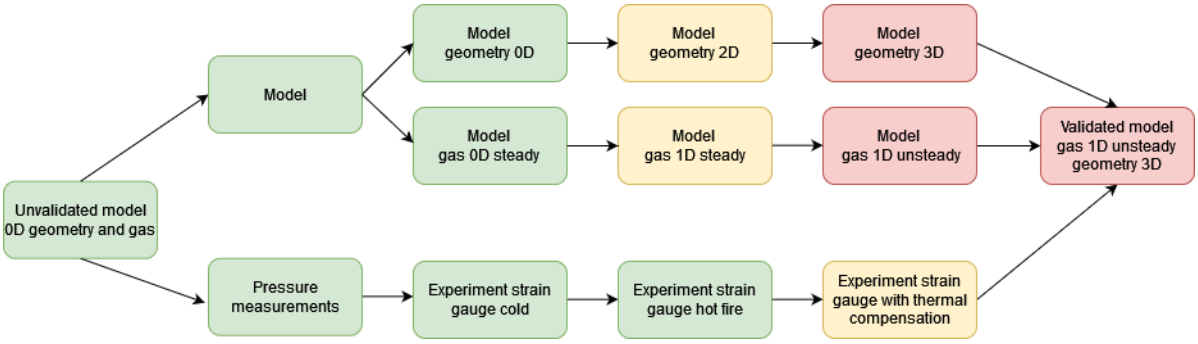

Figure 1.1: Road map showing previous completed steps in green, the relevant parts for this thesis in yellow and recommendations for future research in red.

Research Objective

In order to improve access to atmospheric research the effect of geometry to optimise multiple BATES grain motors requires research. Therefore, the main research objective of this thesis is:

> **”Analyse the effect of changes of internal geometry of solid rocket motors in aspect ratio and motor length on the pressure over time. By developing, validating and using a model for medium-sized solid rocket motors using a multiple BATES grain design which takes into account spatial variation along the length of the motor.”**

The value of the conclusions made from a model is only valuable if the results from the model are validated. Validation data for solid rocket motor models are almost exclusively provided in the form of single-point pressure measurement, usually at the forward closure. A high fidelity gas dynamic model considers the flow field of the gas along the entire motor length. Validation data with pressure along the motor is required to validate these models considering. However, this is expensive as this requires

dedicated tests with intrusive instrumentation. Therefore a second objective is added to acquire validation data during static hot fires of solid rocket motors in a non-intrusive way using strain gauges, similar to the method from Gudu[7].

Structure

The report structure is based on the IMRaD structure (Introduction, Methods, Results, and Discussion), but added a specific conclusion and recommendation chapter and a literature review chapter to provide background. In the introduction the research question is presented after presenting the relevance of the topic. Then the literature review in chapter 2 gives background on the fundamentals of solid rocket motors, some explanation on the combustion characteristics of ammonium perchlorate propellants and a short overview of erosive burning models. chapter 3 discusses the methodology for both the experimental effort and modelling effort, the experimental method describes the use of strain gauges to infer static pressure along the length of the motor and the model section lays out the sub-models for the geometry and the gas dynamics. These models are verified and validated with analytical data and experimental data in chapter 4. In chapter 5 the results the sensitivity study on aspect ratio, truncation and elongation are presented as well as the results gained from the experiment. These results are then discussed in chapter 6 in the same order as they are presented in the result chapter. Lastly, the conclusions in chapter 7 reflect on whole work drawing conclusions on the model and experimental work as a whole and in chapter 8 some recommendations for future work are left.

2

Literature Review

This chapter presents some literature to serve as a background for the rest of the work. It goes over the fundamentals of solid rocket motors in section 2.1, then internal ballistics split into the geometry and gas dynamics in section 2.2 and section 2.3 respectively. Then it goes more in-dept on the combustion in section 2.4 to provide some background on the next topic of erosive burning in section 2.5. Lastly, the verification cases and comparison cases from literature are introduced in section 2.6.

2.1. Solid Rocket Motors Fundamentals

This section will give a brief history of solid rocket motors in section 2.1. Then go over the basic equations for the thrust of a solid rocket motor in Figure 2.1 and further in dept on the nozzle in Equation 2.1 and finish giving an introduction to propellant types itself in Figure 2.1.

Brief history

Solid rocket propellant started with black powder, a mixture of saltpetre (KNO3), sulfur and charcoal, in ancient China (220 BC) [10] and took a big growth spurt of performance in the ’40s and ’50s see Figure 2.1 [10]. This is when composite propellants were introduced, with usually a salt as an oxidiser with a binder that provides the structure and acts as a fuel, like polysulfide, asphalt etc.. The technology matured with the introduction of hydroxyl-terminated polybutadiene (HTPB) as matrix/binder that produces combustion products with low molecular mass and explosives replacing the oxidiser like CL-20, RDX and HMX.

Basic equations

The basic principle of a rocket is simple, something is ejected from a rocket at high velocity, creating a force that propels the rocket in the opposite direction. A solid rocket motor converts chemical energy from burning solid propellant to kinetic energy by means of a nozzle. A schematic representation of this can be seen in Figure 2.2.

$$F = C_F \cdot A_t \cdot p_c \tag{2.1}$$

The thrust of a solid rocket motor is mostly determined by the pressure of the gasses leaving the combustion chamber. Equation 2.1 shows this relation between F thrust, A_t the throat area, p_c chamber pressure and C_F the dimensionless thrust coefficient [11], further explained in Equation 2.1.

$$\frac{d(\rho_g V)}{dt} = \dot{m}_g - \dot{m}_d \tag{2.2}$$

$$\dot{m}_g = r \cdot \rho_p \cdot A_b \tag{2.3}$$

$$\dot{m}_d = \frac{A_t \cdot p_c}{C^*} \tag{2.4}$$

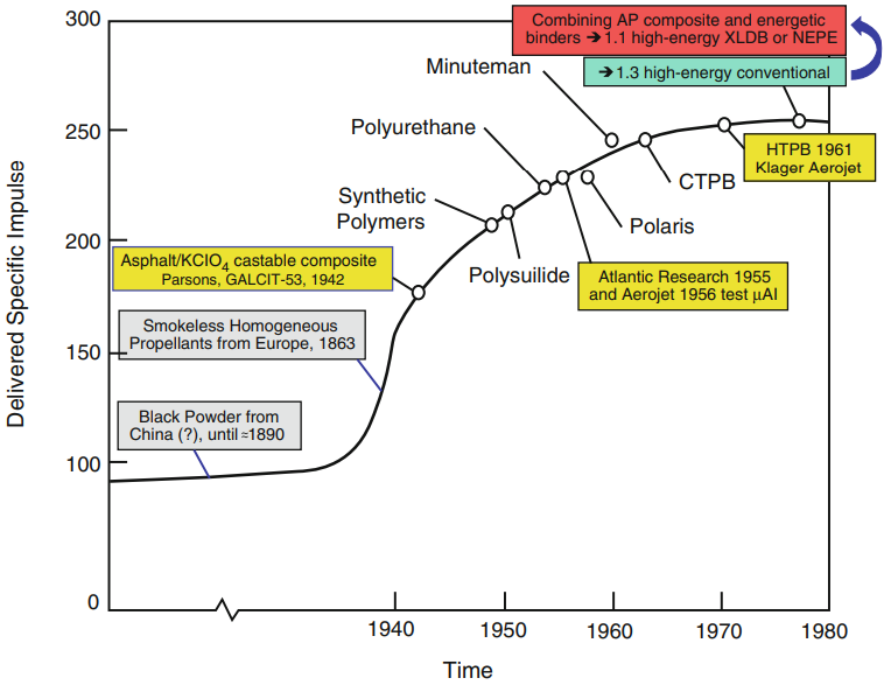

Figure 2.1: The delivered specific impulse over the last century illustrates the development of solid rocket propellants well. It started with black powder, with a specific impulse of around 100, and really started growing significantly during the forties when rockets were used to assist jet take-off. The performance increase mostly flattened after the eighties and similar technology is still widely used today [10].

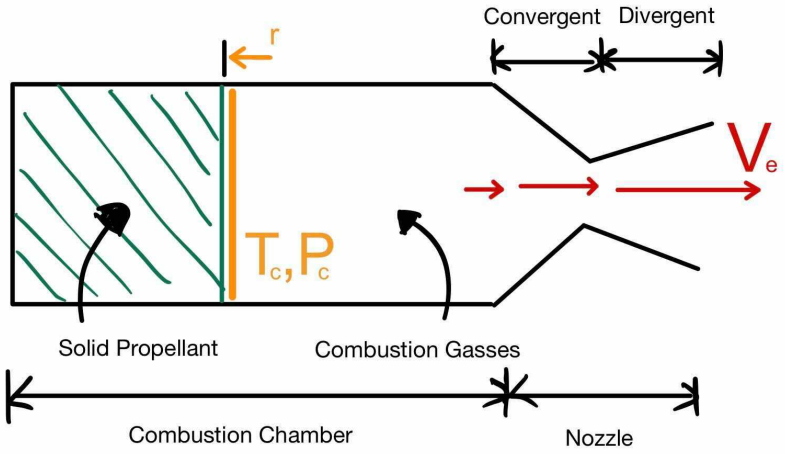

Figure 2.2: A schematic view of a rocket motor shows the solid propellant which regresses with a regression rate (r). The rest of the chamber contains the reaction products of the combustion at the surface of the solid propellant and is at a certain chamber pressure and temperature. This temperature and pressure energy is converted by the nozzle into kinetic energy, the convergent part of the nozzle accelerates the gasses to Mach 1 and the divergent part of the nozzle increases the gas velocity further. Based on work from Kuo [11]

The mass balance, Equation 2.2, for the combustion chamber consists of the mass of gas generated by the burning of solid propellant and the discharge through the nozzle. The gas generated is determined by the regression rate of the solid propellant, Equation 2.3 gives, $\dot{m}_g$, the mass of the gas generated by, r, the regression rate, ρ_p, the propellant density and A_b, the burning surface. Equation 2.4 gives the discharge of a nozzle from A_t throat area, p_c chamber pressure and C^* characteristic velocity which is a function of the temperature, molecular weight and specific heat ratio and describes the quality of combustion. When combining Equation 2.2, Equation 2.3 and Equation 2.4 and assuming $\frac{d(\rho_g V)}{dt} = 0$ an

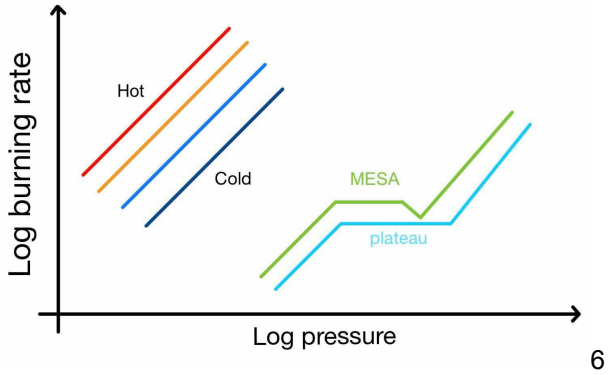

Figure 2.3: Effect of variation by temperature on the linear factor a in the Vieille law and variation in the power factor n by burn rate modifiers. Higher initial temperature increases the burn rate with a linear factor and lowers initial temperature vice versa. Plateau burning propellants burn at a constant burn rate for part of the pressure range and MESA in addition also decreases for part of the pressure range. Based on NASA report SP8039 [12]

equation for chamber pressure can be found, see Equation 2.5. When combining that with Equation 2.1, Equation 2.6 gives thrust from burning surface, burn rate, propellant density and coefficients

$$p_c = \rho_p \cdot r \cdot C^* \cdot \frac{A_b}{A_t} \tag{2.5}$$

$$F = C_F \cdot C^* \cdot \rho_p \cdot A_b \cdot r = I_{sp} \cdot \dot{m}_g \cdot g_0 \tag{2.6}$$

The regression rate r of solid propellant is the most important variable for internal ballistic simulation. It is most dependent on the pressure in the combustion chamber. Equation 2.7 assumes the burning rate proportional to the nth power this is called St. Robert's or Vieille's law.

$$r = a \cdot P^n \tag{2.7}$$

In Equation 2.7 a is a linear factor mostly dependent on temperature and P chamber pressure with n the exponent. In Figure 2.3 a log-log plot of pressure and regression rate is shown. The effect of temperature on a cold makes it slower and hot faster [12]. Vieille's law is not always valid over the entire range of operating pressures, as different effects can influence the burn rate with changing pressure, an example would be a catalyst or inhibitor that would start taking part in the combustion at a certain pressure. This could change the power n from a positive to a zero or even negative, typical burn rate characteristics are platue and MESA where the burning rate stays constant for a pressure range or decreases locally, see Figure 2.3 [12].
The Vieille's law is often used in preliminary solid rocket motor design as the regression rate is a function of pressure it should be removed from Equation 2.5 to be used for design purposes. This gives Equation 2.8 where $\frac{A_b}{A_t}$ is the burning area over the throat area, ρ_p the propellant density and C^* which is a function of the temperature of the gas in the combustion chamber, specific gas constant and specific heat ratio see Equation 2.9 and Equation 2.10.

$$P_c = \left(C^* \cdot a \cdot \rho_p \frac{A_b}{A_t} \right)^{\frac{1}{1-n}} \tag{2.8}$$

$$C^* = \frac{\sqrt{RT_c}}{\Gamma} \tag{2.9}$$

$$\Gamma = \sqrt{\gamma} \left(\frac{2}{\gamma + 1} \right)^{\frac{\gamma+1}{2(\gamma-1)}} \tag{2.10}$$

Nozzles

The nozzle, as depicted in Figure 2.2 is the part of the solid rocket motor that accelerates the gasses. They accelerate the gasses first to sonic condition by converging the flow and after that diverge the flow to bring it supersonic. The performance of the nozzle is given by C_F, the thrust coefficient. The dimensionless thrust coefficient is the ratio between the pressure force on the combustion chamber just from the absence of a wall at the throat and the actual thrust which is higher due to the nozzle decreasing the pressure force in the converging section and increasing it in the divergent section[11]. The top situation of Figure 2.4 shows the situation when the thrust coefficient would be unity with just a simple hole as nozzle constant pressure in the chamber and fully gaseous exhaust. The bottom situation in Figure 2.4 shows the situation when the thrust coefficient is higher due to the acceleration of the gasses which results in a higher resultant force on the rocket. The thrust coefficient also becomes lower when the ambient pressure increases as the gas can be accelerated less.

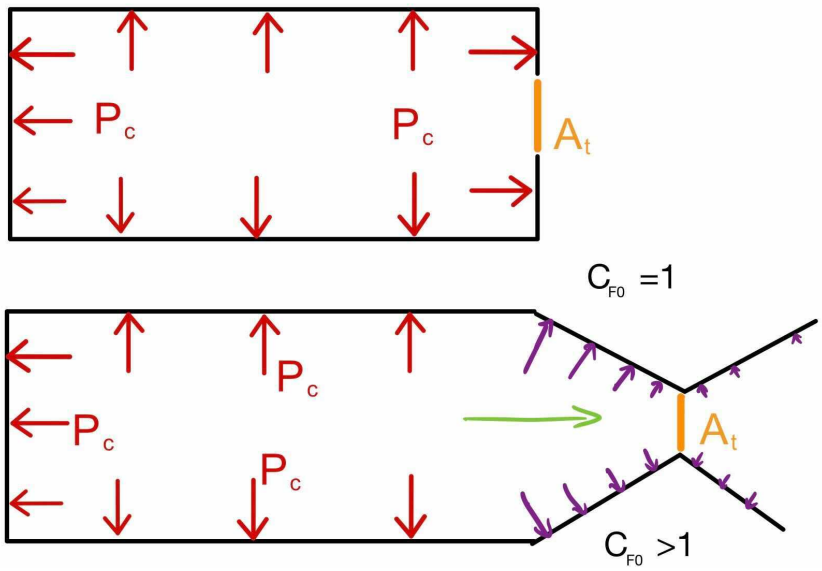

Figure 2.4: Top situation shows the situation with $C_F = 1$, where the thrust is equal to the chamber pressure times the throat area as all the resulting forces cancel with the opposite wall except for the wall opposite to the nozzle. In the situation below $C_F > 1$ due to the acceleration of the flow which decreases the pressure opposite to a greater part of the chamber. Based on work by Kuo [11]

The thrust coefficient in solid rocket motors also contains the decrease in thrust due to solid and liquid particles in the exhaust. As liquids and solids do not compress like gasses they do not get accelerated by the nozzle and only accelerate due to the drag from the gas that is flowing through the nozzle. In addition, the liquid and solid particles could transfer heat to the surrounding gas. Reality lies somewhere in the middle, but it is clear that it provides losses due to solid particles in the exhaust [13].

For small rocket motors nozzles are often made out of graphite entirely, this is due to the high temperature of the exhaust gasses. For bigger diameter motors nozzles are often made out of a combination of materials with often graphite in the throat. Figure 2.5 shows an example of a small rocket motor nozzle made of linen phenolic composite outer shell with a graphite core.

Propellant types

As can be seen in ,Figure 2.1 there have been different kinds of solid propellants developed over the years. Solid propellants are divided in two main categories, homogeneous propellants and heterogeneous propellants. Double base propellants contain both fuel and oxidiser in one molecule and therefore are homogeneous, they do usually still contain some additives but the main chemical energy comes from ingredients that are energetic by themselves. Composite propellant consists of crystalline structures surrounded by a binder that also acts as fuel. Composite propellants can best be classified by their crystalline oxidiser as the choices are relatively limited and define a lot of the final propel-

Figure 2.5: Small single-use nozzles made from linen phenolic with a graphite throat give an idea of what a nozzle of a (smaller) solid rocket motor can look like. [14]

lant properties. A non-exhaustive list of typical ingredients for composite propellants can be found in Table 2.1.

The industry standard currently is ammonium perchlorate, often in multiple sizes, with either HTPB or PBAN as a rubber binder and aluminium as fuel. Ammonium nitrate propellants are used when no hydrogen chloride is wanted like in gas generators to start turbo pumps. Both ammonium dinitramine and CL-20 are propellants that are researched for their extra efficiency and beneficial exhaust products against launch detection.

Typical solid rocket motor

A solid rocket motor is described by its physical design and its performance in form of pressure or thrust trace over time. Figure 2.6 shows a typical thrust or pressure trace from Sutton[15]. The figure first shows an initial pressure peak associated to the igniter followed by an ignition delay, before the combustion chamber is filled with gas and ramps up during the rise time. The burn time is defined from the point of 10% thrust of maximum or the thrust that is needed to lift the vehicle. The maximum thrust is often in the beginning, which is desired as the vehicle is heaviest then. Erosive burning often contributes to the maximum thrust due to the smaller initial core and high mass flow.

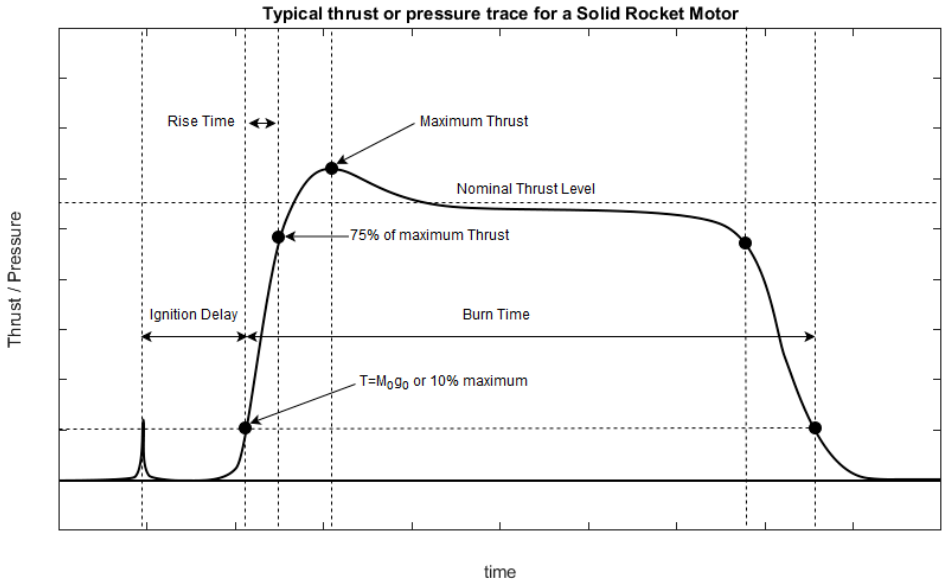

Figure 2.6: Typical pressure or thrust trace of a solid rocket motor showing definitions for burn time, nominal thrust level, ignition delay, rise time and maximum thrust from Sutton [15]

The typical solid rocket motor consists of propellant, pressure vessel, nozzle and a bulkhead. The propellant can be case bonded and cast right into the pressure vessel or free standing and be cast

Composite propellant oxidizer	
AP:	ammonium perchlorate
AN:	ammonium nitrate
ADN:	ammonium dinitramide
NP:	nitronium perchlorate
KP:	potassium perchlorate
KN:	potassium nitrate
Explosive filler	
RDX:	cyclotrimethylene trinitramine
HMX:	cyclotetramethylene tetranitramine
CL-20:	Hexanitrohexaazaisowurtzitane
Binder	
PS:	polysulfide
PVC:	polyvinyl chloride
PU:	polyurethane
CTPB:	carboxyl terminated polybutadiene
HTPB:	hydroxyl terminated polybutadiene
PBAN:	polybutadiene acrylonitrile
Curing and/or crosslinking agents	
PQD:	paraquinone dioxime
TDI:	toluene-2,4-diisocyanate
MAPO:	tris(l-(2-methyl) aziridinyl) phosphine oxide
ERLA-0510:	N,N,0-tri (1,2-epoxy propyl)-4-aminophenol
IPDI:	isophorone diisocyanate
Bonding agent	
MAPO:	tris(l-(2-methyl) aziridinyl) phosphine oxide
TEA:	triethanolamine
MT-4:	adduct of 2.0 moles MAPO, 0.7 mole azipic acid and 0.3 mole tararic acid
HX-878:	Cyanoethylated Polyamine
HX-868:	Polyfunctional Aziridine
HX-752:	1, 1′-isophthaloyl bis(2-methylaziridine)
Plasticizer	
DOA:	dioctyl adipate
IDP:	isodecyl pelargonete
OOP:	dioctyl phthalate
Burning rate catalyst	
Fe203:	ferric oxide
FeO(OH):	hydrated-ferric oxide
nBF:	n-butyl ferrocene
DnBF:	di-n-butyl ferrocene
LiF:	lithium fluoride
Metal fuel	
Al:	aluminum
Mg:	magnesium
Be:	beryllium
B:	boron
Combustion instability suppressant	
Al:	aluminum
Zr:	zirconium
ZrC:	zirconium carbide

Table 2.1: Common ingredients for composite propellants modified from the original by Kou [11]

separately from the pressure vessel and later assembled. Figure 2.7 shows a solid rocket motor in which propellant segments are free-standing from the pressure vessel and with the top and bottom of each grain able to burn, this is called a BATES configuration further elaborated on in section 2.2.

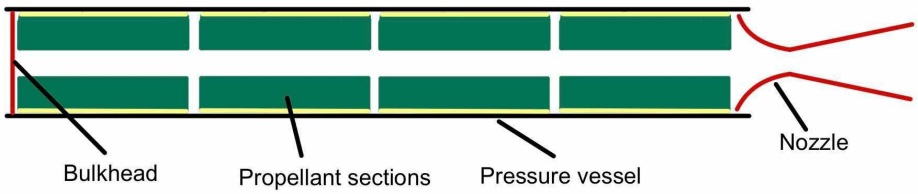

Figure 2.7: Typical free standing solid rocket motor with BATES grain propellant sections showing the main components: nozzle, propellant sections, pressure vessel and bulkhead.

2.2. Internal Ballistics: Geometry

Internal ballistics is the study of the interaction of propellant combustion and chamber pressure. Internal ballistics is a subgroup of ballistics, the study of projectiles. For guns it studies the interaction of powder burning, the pressure developed and the motion of the projectile along the bore of the gun. With respect to solid rocket motors, it refers to the interaction of chamber pressure, regression rate, etc..

Modelling the internal ballistics can be split up into two parts, the grain burn back model, which model the grain geometry over time and the gas-dynamic model. So first in section 2.2, the possible grain geometries and their influence will be discussed followed by Figure 2.2 about how best to model the internal geometry. The second part of internal ballistics, about modelling the internal flow field and gas dynamics, will be discussed in section 2.3.

Grain geometry

In section 2.1 it was shown how the thrust over time can be found when assuming steady-state and homogeneous conditions in the combustion chamber. Even when using this steady-state analytical method the ratio between burning surface and throat area (also referred to as Klemmung) should be known over time. Often this is done by creating a function of area ratio versus web thickness or burn distance.

$$k_n(klemmung) = \frac{A_b}{A_t} \tag{2.11}$$

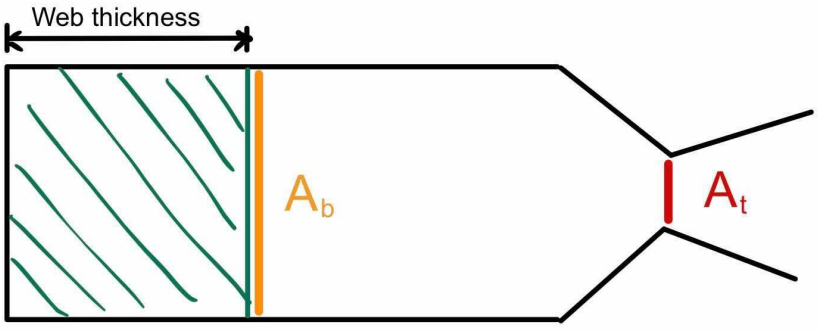

Figure 2.8: Burn area and throat area, the ratio between these areas is known as the Klemmung and is the most important characteristic for the operating pressure.

The Klemmung predominately determines the pressure and thrust level of the motor and therefore the design of the Klemmung over time takes the biggest role in designing the thrust profile. This Klemmung over time can be influenced by changing the core geometry or by exposing the propellant grains in

different directions like BAllistic Test and Evaluation System (BATES) grains. BATES grains are grains which during the burn keep their burning surface area approximately equal, they were developed to compare the performance of different propellants [16]. Figure 2.9 shows a BATES grain and how it regresses, these grains can also be stacked and made into a longer engine, however, this will increase the mass flux through the core and at some point result in erosive burning.

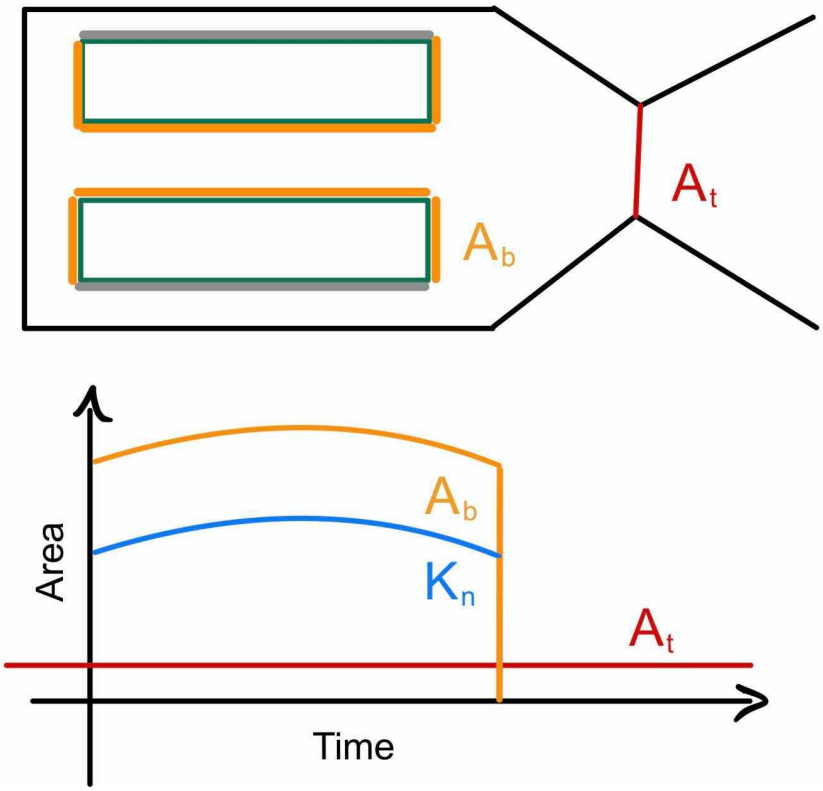

Figure 2.9: BATES grains and the resulting burning area over time including its resulting Klemmung which shows that the BATES grains burn close to a neutral profile (note that this is a ratio, not an area).

The only way to control the thrust of a solid rocket motor with one propellant is during the grain design with the grain geometry. In Figure 2.10 some different kinds of thrust profiles that are possible are shown [17]. The design of these shapes is described in depth in NASA SP-8076 [18]. Another way the thrust is controlled instead of geometry is by using multiple propellants with different burn rates. A bi-propellant star is discussed in the NASA report NP-8076[18] with fast-burning star arms in a faster-burning propellant.

Burning area accounting

Keeping track of geometry over time of a solid rocket motor is an integral part of simulating the performance and pressure trace of a solid rocket motor during the quasi-steady state between ignition and tail off. There are three main ways to keep track of the geometry of the solid rocket motor: analytically, Lagrangian approach and Eulerian.

Analytic method

Analytical methods differ fundamentally from the Lagrangian and Eulerian approaches as they usually assumed one burn rate over the entire geometry and makes it impossible to use in combination with local burning modifiers like erosive burning. In analytical methods, analytical equations are used to determine the burning area of a solid propellant grain like in Figure 2.9 as a function of web thickness. This web thickness can then be marched through with the regression speed or burning rate found. The easiest example is a circular grain with only a burning core the burning area is then simply π multiplied by the length and diameter see Equation 2.12.This can also be done for multiple sections allowing for different burn speeds over the length of the motor. Troy Prideaux developed an excel sheet that

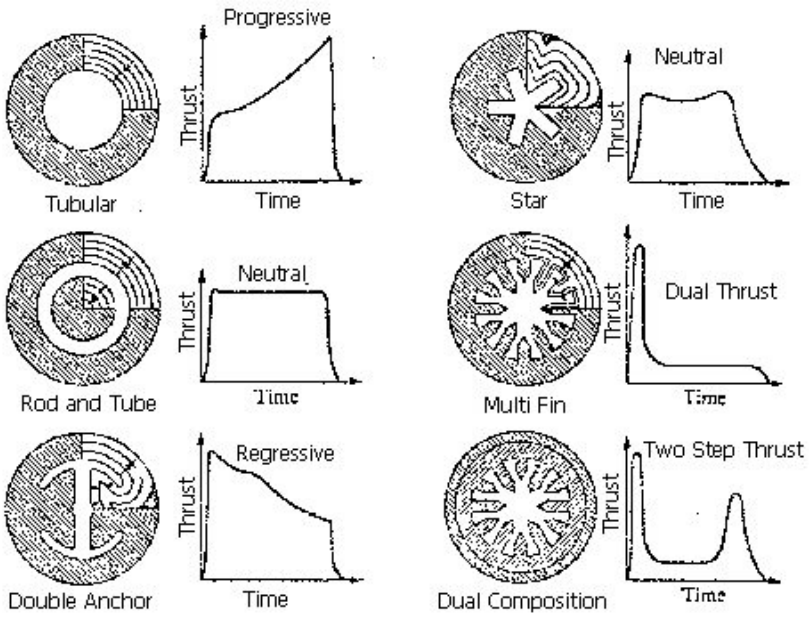

Figure 2.10: Different thrust over time can be created by manipulating the initial grain shape. [17]

includes analytical approaches to determine the burning area of quite a range of geometries[19]. His work calculated the burning area for star cores, cross cores, duel circle cores, moon cores, Pacman cores, D-shaped cores, C slot cores and finocyls see Figure 2.11 and did this all analytical for each time step.

$$A_b = L_{grain} \cdot \pi \cdot d_{core} \tag{2.12}$$

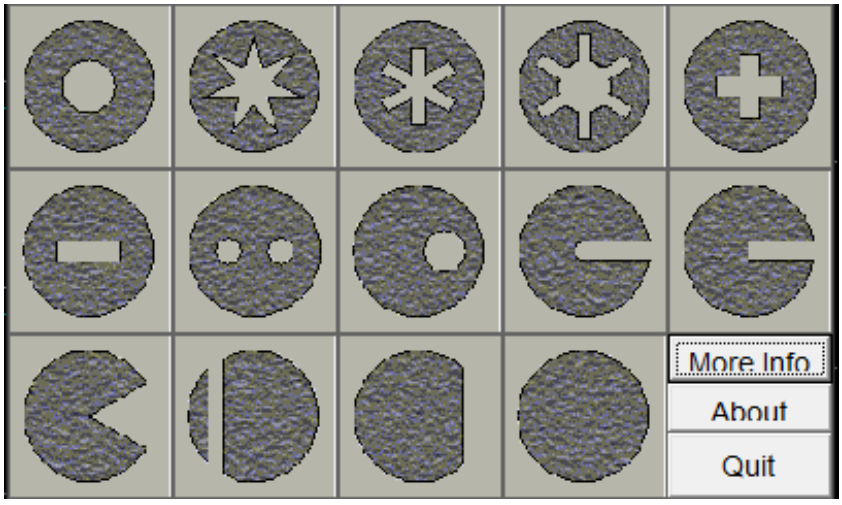

Figure 2.11: Screenshot from excel program from Troy Prideaux showing the different grain shapes to give an overview of possible shapes [19]

Minimum distance function

The specific method used in this thesis is the minimum distance function. This is due to its ability to describe the surface with a sub grid precision. This ability is even better achieved by the level set method as used by Cavallini [5], however, this method requires complex mathematical operations to

which increase development time.

The minimum distance function describes the surface by giving the minimum distance from the surface for each grid point. Figure 2.12 shows how the burning surface is located between the positive and the negative values. Surface evolution can easily be calculated by subtracting the burn rate times the time step from all the initial minimum distance functions and this reduces the computational time a lot when compared to the previous methods[8]. Figure 2.13 shows how the burning surface moves with subtracting the burn distance. This does mean that only burning normal to the surface can be simulated.

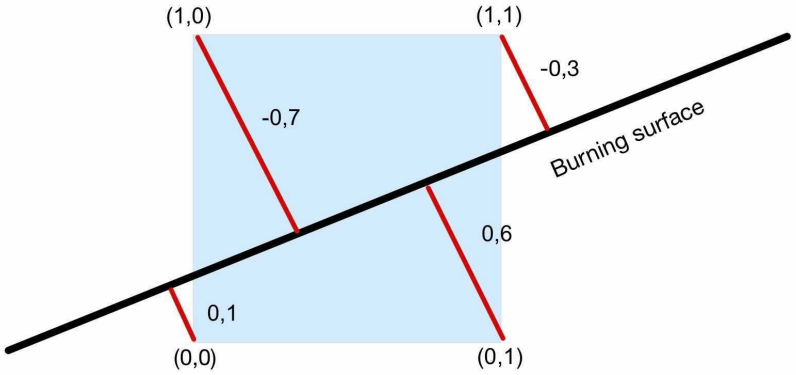

Figure 2.12: Example of burning surface in between grid points with associated minimum distance values. Based on Willcox [8]

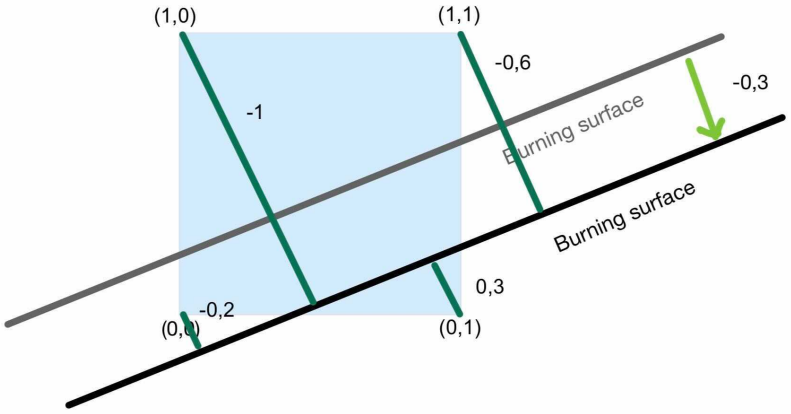

Figure 2.13: Example of two-dimensional burning surface evolution of -0.3 with associated minimum distance values. Based on Willcox [8]

Willcox implemented this model in rocgrain[8] and reported surface area errors of less than 0.5% for a sufficiently large number of grid points (500).

2.3. Internal Ballistics: Modelling gas dynamics

Gas dynamics is the accounting of the gasses in the chamber towards the outside and in internal ballistics, it plays a vital role to connect the propellant grain with a thin zone of combustion on its surface to the nozzle which discharges the combustion gasses. There are multiple ways of accounting for these combustion products that range from a simple mass balance as presented in Equation 2.2 till numerical simulations that take into account compressible, viscous, and reacting flow. In industry, 1-D simulations are generally the standard[4], but 0-D models are still useful for motors with insignificant

influence by 1-D effects like pressure drop and erosive burning[8].

Dimension

In reality, a solid rocket motor has three spacial dimensions, however, this can be simplified in order to keep computational costs down. The cheapest model is zero-dimensional where all the volumes are lumped up and the combustion chamber has one temperate, pressure and mass. Then this can be increased to one dimension where the pressure drop and velocity of the flow can be assessed along the length of the motor, these are important for the modelling of erosive burning. The dimension that is chosen for one-dimensional simulations is along the motor longitudinal axis or the z-axis in Figure 2.14. 2D and 3D models are used much more often for computational fluid analysis, as a result the meshing and solving techniques are easily accessible and mature, like open-source CFD solvers SU2 and OpenFoam [20], [21]. These 2D and 3D models, in general, are harder to modify due to their complexity. For two dimensional models either the y or x-axis is taken as a two-dimensional system that assumes axis symmetry.

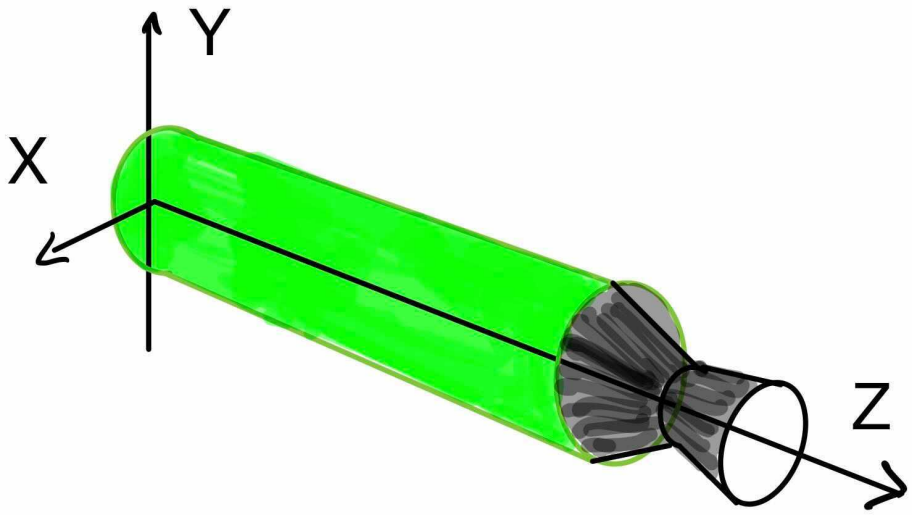

Figure 2.14: Picture showing the reference frame for the axis in the motor with the z-axis being used for 1-D simulations.

Zero-dimensional

Equation 2.13 and Equation 2.14 show the mass and energy balance of a zero-dimensional or lumped sum of the combustion chamber. When m_{in} is defined by Equation 2.7 and when the nozzle is choked m_{out} is also defined by Equation 2.4 and during ramp up a discharge coefficient can be assumed.

$$\frac{dp}{dt} = \frac{RT}{V}\left(\dot{m}_{in} - \dot{m}_{\text{out}}\right) + \frac{p \cdot dT}{T \cdot dt} - \frac{p \cdot dV}{V \cdot dt} \tag{2.13}$$

$$\frac{dT}{dt} = \frac{RT}{pV}\left[\gamma\left(\dot{m}_{in}T_{in} - \dot{m}_{out}T\right) - \left(\dot{m}_{in} - \dot{m}_{out}\right)T\right] - \frac{RT \cdot dV}{C_v V \cdot dt} - \frac{q}{C_v} \tag{2.14}$$

Zero-Dimensional models inherently assume a constant temperature and pressure with respect to the position in the combustion chamber. In Equation 2.13 and Equation 2.14 adiabatic and non-reactive flow is also assumed. This model can be made into a quasi-1D model if the knowledge about the area of the cross-section is combined with the mass flow from all grains this can then give a good estimate of the velocities. A zero-dimensional model can be used for solid rocket motors with insignificant one-dimensional flow effects like pressure drop and erosive burning and with fast enough flame spreading that instantaneous ignition of all surfaces can be assumed.

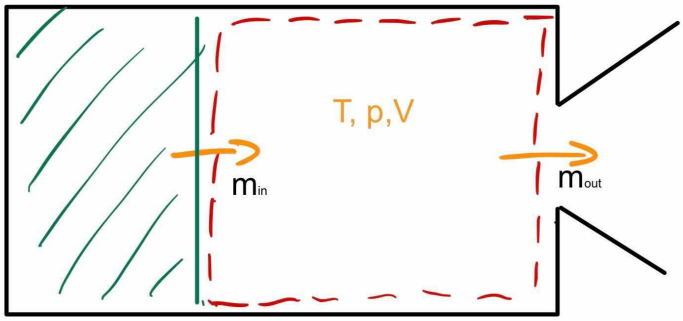

Figure 2.15: Zero-Dimensional lumped sum model with control volume boundaries just above the reaction zone and at the nozzle throat.

Steady vs non-steady state

There are two parts of the model which require a discussion on assuming steady or unsteady, namely for the geometry and for the gas dynamics. When looking at the geometry it seems to be quite clear that the assumption of steady-state is valid when looking at the gas dynamics. In Table 2.2 the velocities of burn rate (change in geometry) and velocity of the gasses after combustion radially and the expected velocities of cross-flow are shown.

Description location	Typical velocity
Burn rate AP/HTPB/Al	6mm/s
Gas velocity leaving the surface	1.4 m/s
Gas velocity	>300m/s

Table 2.2: Velocities from different parts of the internal ballistics.

For the gas dynamic model the thermodynamic properties of the gases in the chamber could also be seen as the evolution of quasi-steady states. In Equation 2.5 this quasi-steady state is assumed, and this can be done for one, two and three-dimensional cases too running steady-state solutions as an evolution after each other.

Then lastly the combustion itself can be assumed steady-state or not, this is something that Zeldivich and Novozhilov[22] looked at extensively with unsteady burning. Additionally, combustion instabilities can only be modelled when combustion is not steady.

Nozzle modelling

The nozzle is an important part of the solid rocket motor when determining its performance. Different levels of fidelity can be chosen when integrating a nozzle in a model of a solid rocket motor. In Figure 2.1 the nozzle is described in the model only with a discharge term with an assumed C^*, characteristic velocity, and in order to translate this to thrust an additional assumption on C_F, the thrust coefficient, is needed.

An alternative for using the thrust coefficient, which in reality changes significantly with chamber pressure, is to include the nozzle in the numerical simulation. Cavallini includes the nozzle in his one dimensional unsteady Euler simulation but does include a friction coefficient[23]. Willcox uses discharge coefficient or isentropic choked nozzle relations for both zero and one-dimensional simulations[8]. Both do not go into particular detail about the basis of their choice. It seems to be somewhat more accurate to include it in a one-dimensional simulation, as the effect of the boundary layer on the effective nozzle area is modelled instead of assuming isentropic flow without friction or reduced mass flow due to the boundary layer. Two-dimensional nozzle simulation would potentially add even more fidelity if the viscosity is taken into account, Hermanth reports 5% lower exit velocity with k-ϵ model versus isentropic (simulation done on a nozzle with a throat diameter of 11mm)[24].

2.4. Combustion of Composite Propellants

Combustion in solid rocket motors and underlying mechanisms vary greatly, especially the difference between the double base and composite propellants is noteworthy. Double base propellants are a mixture of propellants that can both be mono-propellant, composite propellants are made up of oxidiser salt crystals in a matrix with fuel. Most of the solid rocket motors flown today are composite propellants made from ammonium perchlorate in a rubber matrix and this will be what this chapter will mostly be focused on.

Oxidizers

In Table 2.1 a list of common oxidisers is already shown. Ammonium perchlorate (AP) is used most often, because of its high performance while being relatively safe to handle. In Figure 2.16, the performance of ammonium perchlorate with HTPB is compared to different oxidisers with HTPB (CL-20 and ADN could potentially be better but are still considered too unstable for practical uses). For the specific impulse two important factors, the molecular weight of the combustion products and the temperature of the combustion products play a role. Together they determine the specific impulse that a propellant can achieve. Usually, there are other design criteria like handling, stability, mechanical strength or burn stability that result in a different choice of oxidiser concentration than what would be optimum for specific impulse.

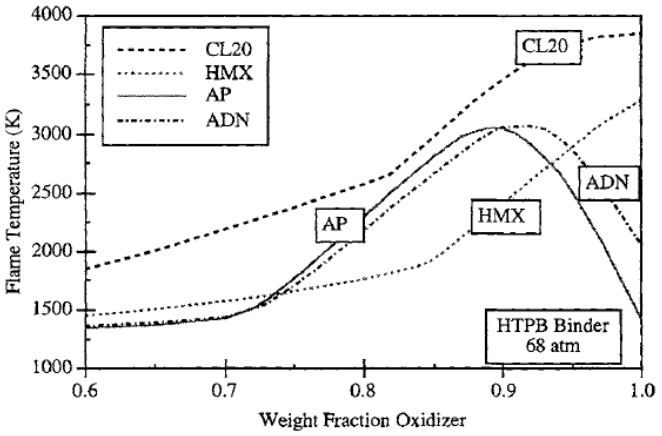

Figure 2.16: Performance of oxidiser with HTPB as binder measured in specific impulse. By Beckstead [25]

Ammonium dinitramide (ADN) and CL-20 are still two promising oxidisers to increase performance and make the exhaust products more favourable against detection as well as get rid of corrosive HCl currently in AP propellants. The table in Figure 2.17 shows how the different oxidisers compare to each other when used as monopropellant. Notable is that AP and Cl-20 perform best with respect to density and that the flame temperature of AP as monopropellant is relatively low.

Ammonium Perchlorate

Ammonium Perchlorate is a salt that can act as a mono-propellant. It exothermically decomposes into ammonia and perchloric acid see Equation 2.15. On the surface, there is a layer with molten ingredients. Before combustion, this layer is relatively thin as the thermal penetration depth is quite shallow with a surface temperature of between 630K to 900K for AP [26]. A higher surface temperature correlates with a higher burn rate and AP has an activation energy of 30 Kcal/mol[26].

$$NH_4ClO_4(s) \rightarrow NH_3 + HClO_4 \tag{2.15}$$

Furthermore, ammonium perchlorate is white and has a density of 1.95 g/cm3 which is one of the more dense oxidisers only being challenged by CL-20 with 1.96 g/cm3[25]. The heat of combustion is -295.8 kJ/mol and its monopropellant flame temperature is 1405K which is quite low in comparison with other oxidizers at a molecular weight of combustion products of 27.9 kg/mol [25].

Ingred.	Density (g/cc)	ΔH_f (Kcal/mole)	Equilibrium products, 1000 psi (mole fractions) T_f, K	MW	O_2	H_2O	CO	CO_2	H_2	N_2	HCl
Nitrates											
ADN	1.72	−35.8	2062	24.8	0.20	0.40				0.40	
AN	1.73	−87.3	1247	22.9	0.14	0.57				0.29	
Perchlorate											
AP	1.95	−70.7	1405	27.9	0.29	0.38				0.12	0.20
Nitramines											
CL-20	1.96	90.0	3571	27.4	0.02	0.14	0.23	0.10	0.03	0.37	
HMX	1.90	18.1	3278	24.3		0.23	0.25	0.09	0.09	0.33	
RDX	1.82	14.7	3286	24.3		0.23	0.25	0.09	0.09	0.33	
HNF	1.86	−17.2	3090	26.4	0.10	0.33	0.02	0.12	0.01	0.35	
Nitrate Esters											
NG	1.60	−90.7	3287	28.9	0.07	0.28	0.11	0.28	0.01	0.18	
TMETN	1.47	−106	2839	23.1		0.26	0.36	0.10	0.14	0.14	
DEGDN	1.39	−103.5	2513	21.8		0.25	0.37	0.08	0.19	0.11	
NC	1.65	−61.4	2425	28.4		0.21	0.43	0.12	0.13	0.11	
Azides											
BAMO	1.28	53.3[a]	1725	15.2			0.11		0.48	0.39	
GAP	1.27	2.85[a]	1570	15.7		0.01	0.19		0.43	0.32	
AMMO	1.26	4.32[a]	1536	12.2		0.01	0.13		0.58	0.23	

[a] Kcal/100 g

Figure 2.17: Mono propellant performance of oxidisers [25]

Fuels and binders

For ammonium perchlorate composite propellants a metal fuel is most efficient as it increases the flame temperature significantly. But a composite propellant also needs a matrix to sit in for its mechanical strength. This section will go over binders first and then aluminium specifically as a metal fuel.

Binders

There are inert and active binders, most binders for composite propellants are inert as they release a lot less heat. Active binders are binders like glycidyl azide polymer which add a modest increase in performance while still serving as a binder and hold the other ingredients[15]. Inert binders really only act as the matrix or structural glue for the solid ingredients. They are usually polymers that are mixed in liquid form as pre-polymer with solid ingredients.

Polyurethane (PU) and polyvinylchloride (PVC) are still used in legacy engines, but most composite propellants use polybutadiene rubbers like HTPB, PBAN, CTPB and PBAA [15]. Which polymer and in combination with what plasticizer and crosslinker influence the mechanical properties to a great extent.

Aluminium combustion

When Aluminium is included in a propellant it is usually in between the bigger oxidizer particles together with the smaller oxidiser particles and binder, these particles are usually in the range of 10-40μm[26]. When combustion takes place the heat penetrates the surface and heats up the aluminium particles, then when the binder around the particles pyrolysis the particle bubbles up from the fuel-rich binder surface[27]. The particle stays stuck to the surface either by surface tension or by being partly stuck into the binder it melts together and accumulates or coalesces into large droplets called agglomerates, typically in the range 50-200μm[27]. These agglomerates have an oxide cap on one side (see Figure 2.19 and usually take between 10-100 ms to completely burn up, this has little influence on the burn rate of the propellant itself because it happens further from the surface and also only reaches this higher temperature further from the surface see Figure 2.20. In the end the aluminium burns up into small smoke particles of aluminium oxide.

The path of these agglomerates is not set after they are created as they can be ignited on the surface after they grew big but still are attached to the surface, ignited when they are still small and attached to the surface, ignite when small but in the flow detached from the surface and also big detached from the surface. Both big cases can lead to residue and incomplete combustion. Figure 2.18 shows an example of how the agglomerates build-up still attached to the surface until ignition occurs and all agglomerates melt together and leave the surface as a big burning aluminium droplet [27].

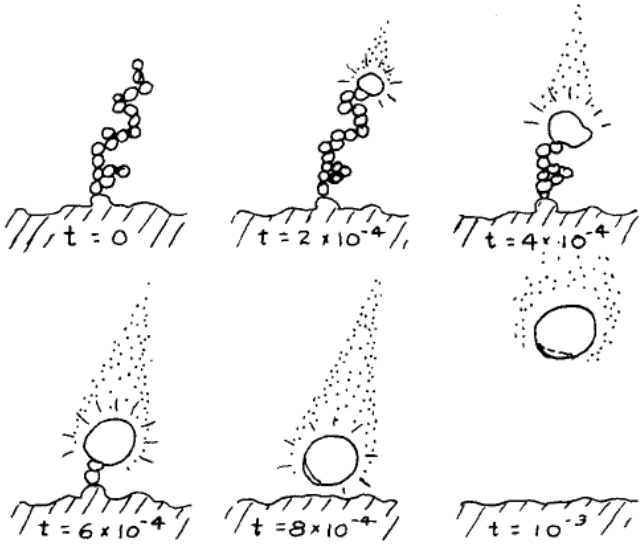

Figure 2.18: Sketches of the different stages of aluminium ignition agglomeration where the hottest particle ignites and consumes the rest of the droplets. By Price[27]

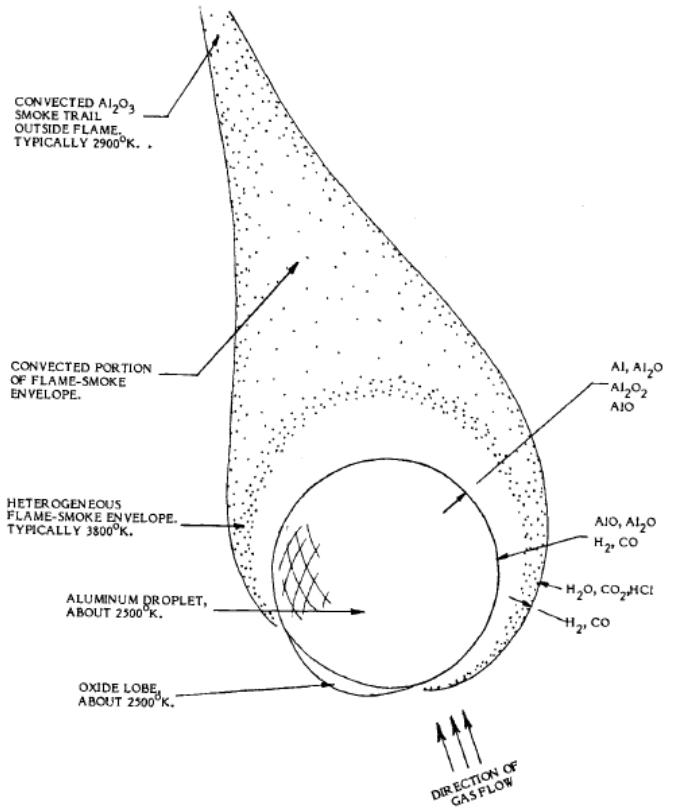

Figure 2.19: Aluminium droplet and drawn combustion zone in a mild convective flow. By Price[27]

Aluminium adds a considerable performance in three major ways it increases the combustion temperature as can be seen in Figure 2.20, it decreases the molecular mass of the combustion products as it binds with oxygen in H_2O and CO_2 (see flame zone around droplet in Figure 2.19) to form H_2 and CO, but also Al_2O_3 and lastly, it increases the density of the propellant due to its density of 2.7 g/cm3.

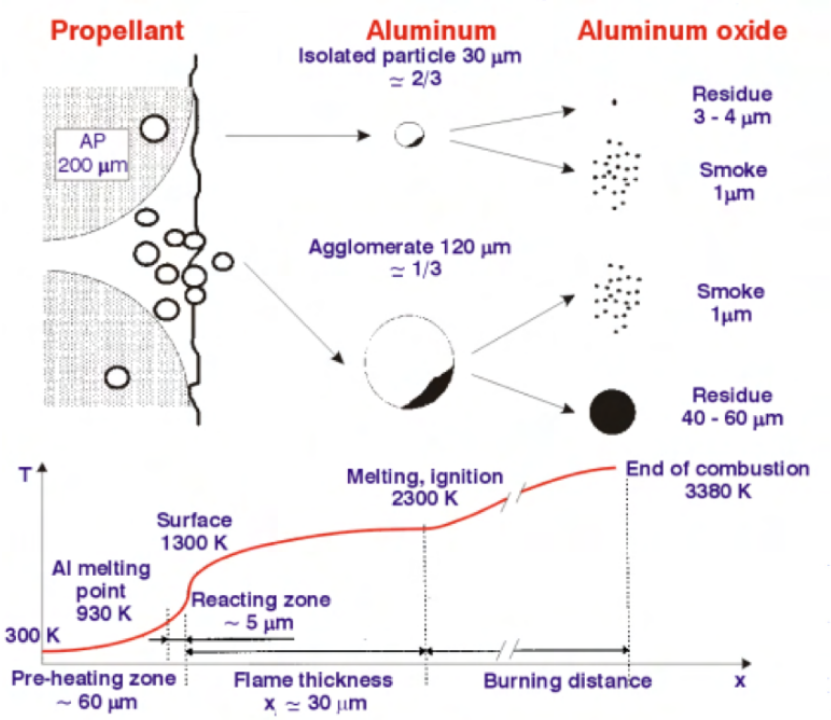

Figure 2.20: Diagram showing aluminium combustion in solid rocket propellant by Fabignon[28]

Flame structure

The flame structure is the most important part in determining the burn rate and finding the underlying mechanism. However, researchers can not see what the flame actually looks like and this model in Figure 2.21 is a concept proposed by Beckstead [26] on composite propellant flame structures. The figure shows different speculative flames that interact with each other.

In Figure 2.21 an AP crystal can be seen in the middle which has a very thin condensed layer on its surface where the decomposed gasses from AP burn in a monopropellant flame close to the surface. In the area where the AP crystal borders the binder a primary diffusion flame burns this is believed to have the biggest impact on the burn rate as it feeds more heat back into the surface due to its proximity[26].

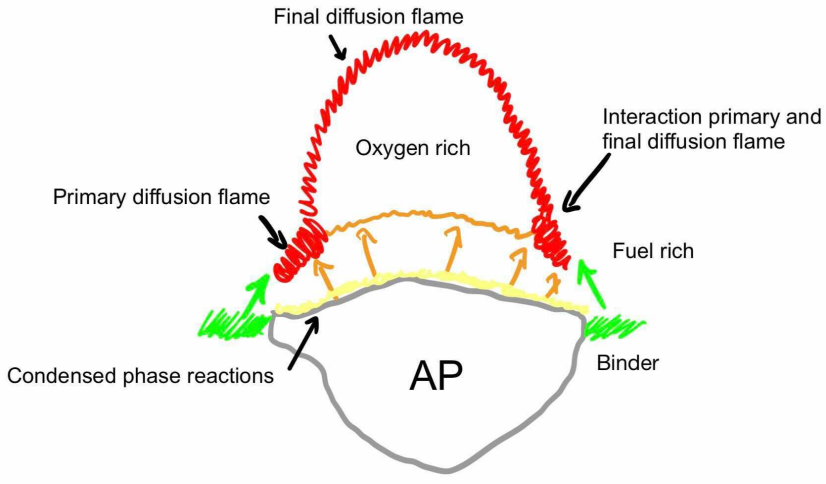

Figure 2.21: Structure of the flame of an ammonium perchlorate composite after Beckstead[25]

The distance between these primary diffusion flames is determined by the size of the AP crystals which then determine how fast the propellant burns. Smaller particle size AP results in the primary

diffusion flames being closer together and when the AP is made small enough the flame approaches a premixed burning rate limit as can be seen in Figure 2.22. When the AP particle size goes up the diffusion flames are so sparse that the burn rate is limited by the heat feedback of the monopropellant flame as can be seen at the monopropellant flame limit in the same figure[26].

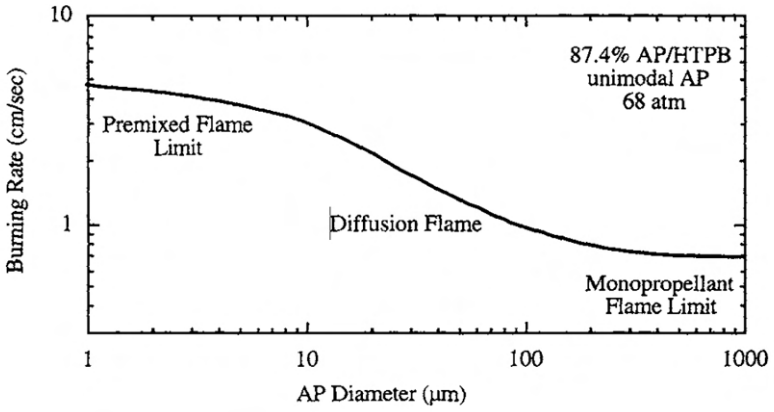

Figure 2.22: Burn rate for one size AP particles varying in size. By Beckstead [26]

Significantly higher above the surface the final diffusion flame resides which brings all the combustion gasses to their final temperature (if no aluminium combustion is present). This flame is usually of secondary importance but can be important in interacting with unstable combustion, motor cross-flow, high pressures or motor acoustics[26]. The general thermal profile above an AP crystal is shown in Figure 2.23 and shows that the primary and combined flame reach a much higher temperature close to the surface.

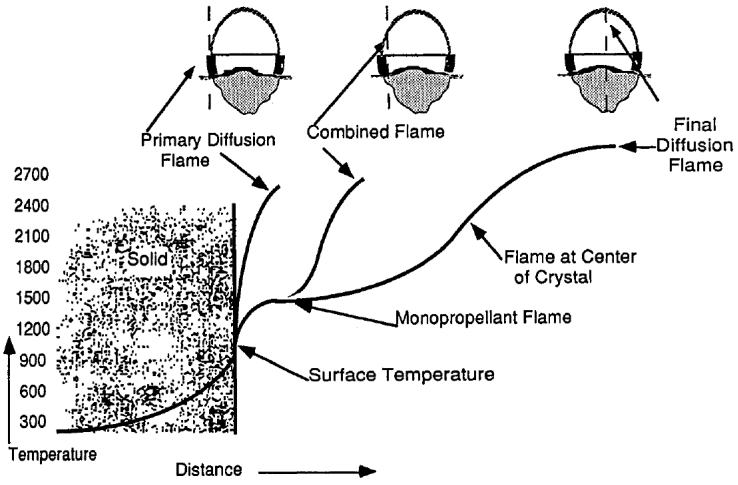

Figure 2.23: The temperature profile of the different flames above the AP crystal. By Beckstead[26]

The effect of pressure on the flame structure is depicted in Figure 2.24 and describes how the primary diffusion flame, monopropellant flame and final diffusion flame change. In general the higher the pressure the more the diffusion flame and monopropellant flame, move closer to the surface. At low pressures, the mono-propellant flame does not really exist at higher pressures the mono-propellant flame comes so close to the surface that it has the biggest influence [26].

Diagnostics

Plenty of attempts at diagnostics have been carried out on the flame structure of AP composite propellants [29]–[32], these diagnostics have been able to show the diffusion flame sheets between binder and oxidiser sandwiches and the temperature difference across this diffusion flame. However, the

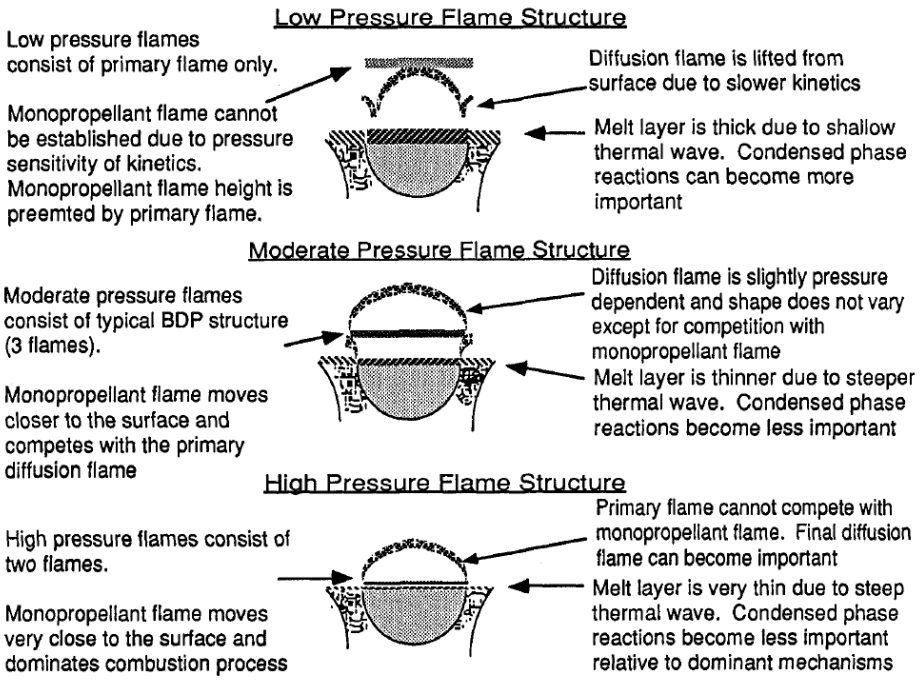

Figure 2.24: Effect of pressure on the flame structure by Beckstead [26]

temperature profile above the surface is hard to capture and that is where more numerical studies are focused. The main difficulties lie with actual propellants having an unknown matrix of AP crystals which means it is not known where the measurement measures in the flame structure beforehand and that the irregular surfaces block the view of the flame zone close to the surface. Both of these problems can be solved by using a laminate, but that does differ significantly from reality and is unsuitable for most complex studies (unsteady burning, instabilities or erosive burning).

Ignition

Ignition of a solid rocket motor consists of three phases 1)induction 2)flame spreading 3)chamber filling. Figure 2.25 shows these three phases and the interaction of erosive burning with the ignition transient. There are different kinds of igniters, most igniters consist of an initial electro-pyrotechnic device called a squib which takes an electric signal and then ignites some kind of small pyrogen, and a booster charge of some kind. Then depending on how big the motor is it can have a secondary or tertiary charge. Figure 2.26 shows a typical placing of solid rocket motor igniters.

Induction is the time lag between the ignition signal and the first ignition of the propellant surface. This is generally an empirical input or complex models are used, a survey of these models is given by Hermance [33]. This is also highly dependent on what kind of ignition system is used and what the igniter heat transfer and flow characteristics are.

Flame spreading is the phase between the first local ignition of the propellant surface and the ignition of the entire propellant surface. The location of the igniter is important for this phase as an igniter placed at the head end will ignite the downstream propellant, but an igniter placed in another place will need to travel both downstream and upstream with the downstream velocity being higher as downstream is the nozzle, an outlet for the gasses [34].

There are lumped sum zero dimension models which use general trends and one-dimensional models that usually use a critical surface temperature as ignition criteria [34]. For rocket motors that are short with respect to their diameter lumped sum models are generally sufficient, however, when the length increases with respect to the diameter then the flame spreading can usually not be described by general trends especially as there starts to be an interaction with erosive burning.

There are two methods that are used for flame spreading, one is using a constant speed for the flame and the other is using a critical surface temperature and calculating the heat transfer to the wall[34]. In

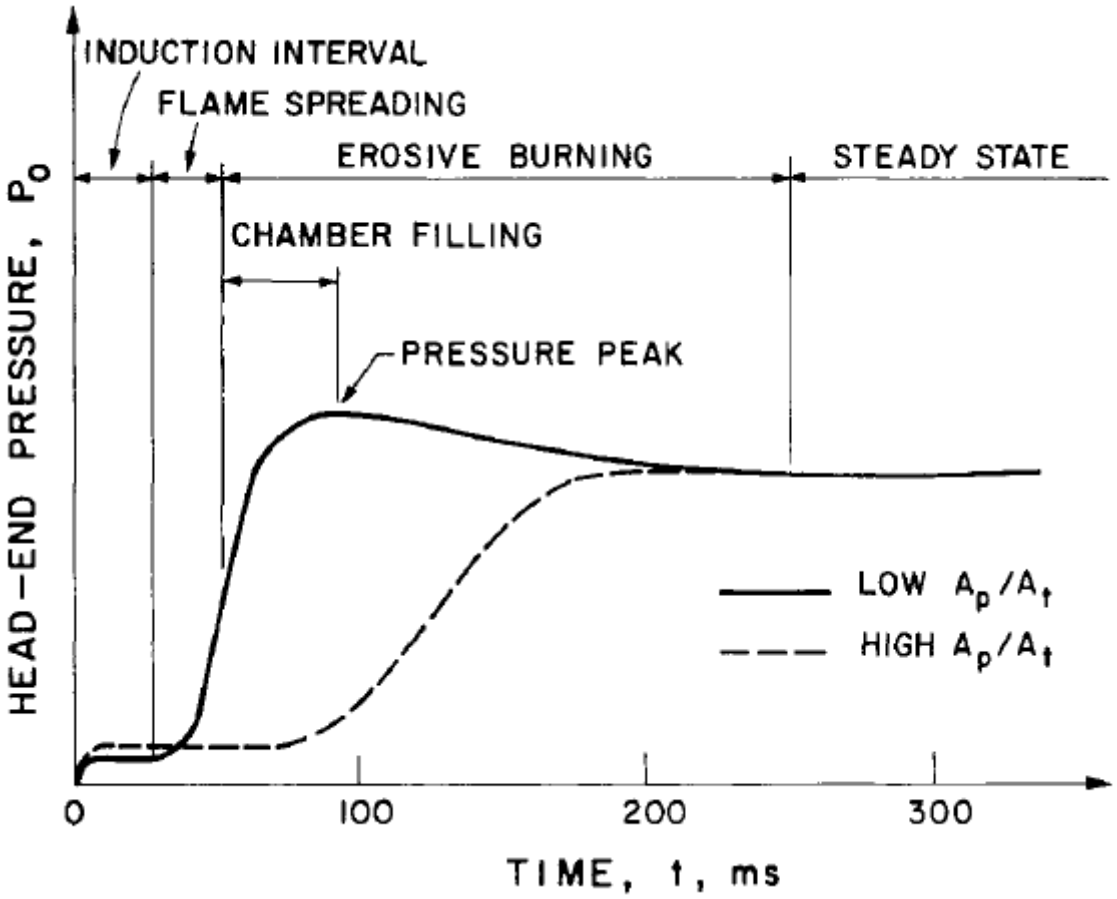

Figure 2.25: The three phases of ignition comparison of high area port and low area port [15]

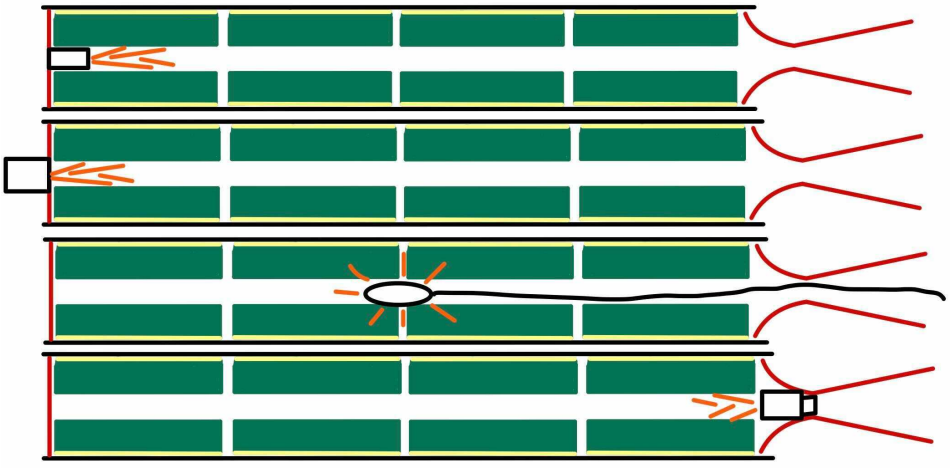

Figure 2.26: Four placements of igniters in solid rocket motors.

Figure 2.27 it can be seen that assuming a constant flame spreading, the temperature will ignore the slow initial spreading rate. Peretz et al. used a one-dimensional gas dynamic model in combination with an extra equation, Equation 2.16, to determine the wall temperature and make the surface ignite when it had reached its ignition temperature (700K in their case). For Equation 2.16 T_{ps} is the wall surface temperature, T_{pi} the initial propellant temperature and T the static gas temperature. h_c, local convective heat-transfer coefficient,is calculated analytically from geometry and gas properties by averaging the film temperature. α_{pr} and λ_{pr} the thermal diffusivity and thermal conductivity respectively. The line

labelled calculation in Figure 2.27 is achieved with this method.

$$\frac{dT_{ps}}{dt} = \frac{4\alpha_{\mathrm{pr}} h_c^2 \left(T - T_{ps}\right)^3}{3\lambda_{\mathrm{pr}}^2 \left(T_{ps} - T_{pi}\right)\left(2T - T_{ps} - T_{pi}\right)} \tag{2.16}$$

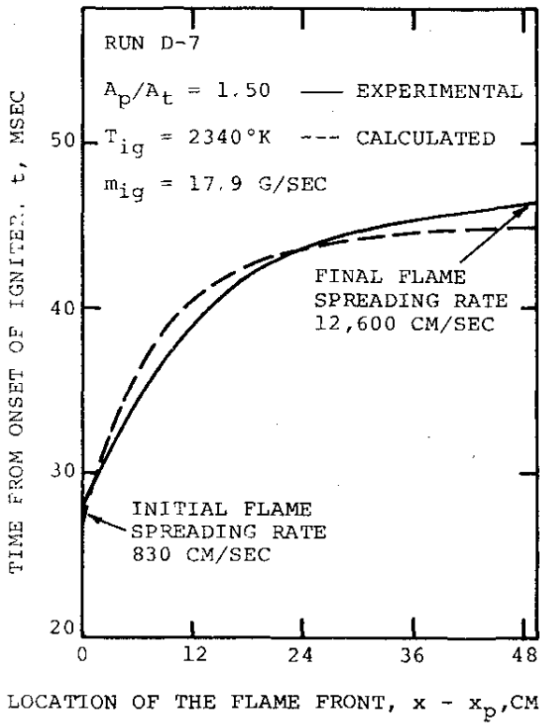

Figure 2.27: Ignition flame front location versus time from which speed is calculated by Peretz et al. [35]

Hump effect

The ”hump” effect is a burn rate modifier of the propellant that looks like a rounded protuberance along with the web thickness of the grain. In Figure 2.28 the simulated burn rate by Uhrig et al.[36] shows the rounded effect along with the web of the grain.

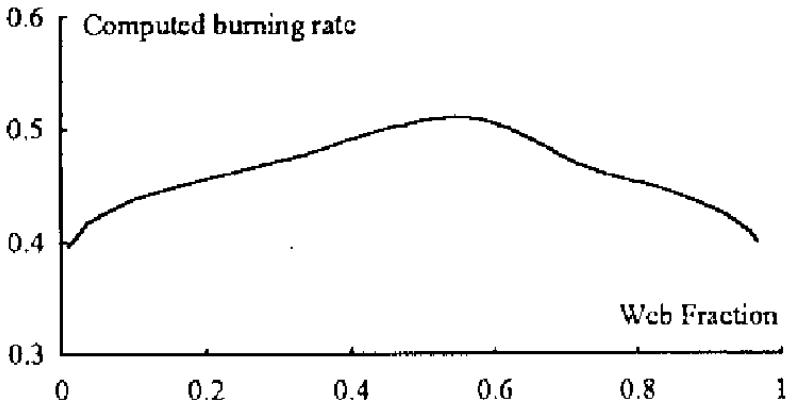

Figure 2.28: The ”hump” effect on the burning rate for cylindrical grains cast mid-web

The variation in burn rate of the ”hump” effect is considered to be due to non-uniformity’s from the casting process and is therefore highly dependent on the casting process[36]. One of the possible

hypotheses is that this is due to thin striations in the mid web of the propellant that speeds up the burning rate and this is supported by the work from Brauner et al. [37]. Brauner showed by simulating the flame front that burns in the same direction as the striations burn faster than when the striations are in the same plane as the flame front, where the striations were binder/fuel-rich layers.

Namah et al.[38] and Uhrig et al.[36] made numerical models to simulate the casting process and its resulting striations. Figure 2.29 shows a typical casting process and its resulting layers as found by the model of Breton et al. [39].

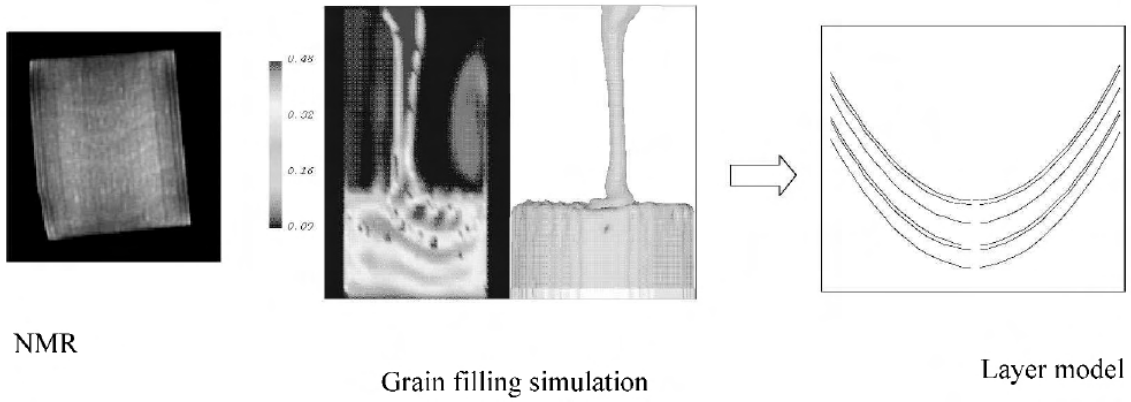

Figure 2.29: Left is a nuclear magnetic resonance scan of the grain. Then in the middle, the filling process of grains and right is the resulting layer model. All by Breton et al. [39].

The ”hump” effect can be modelled by means of casting simulation requiring intimate knowledge of the flow of the propellant during casting to get an idea of the striations. This knowledge would then be used to create a burn rate modifier over the web fraction by comparing the angle of the burning surface to the angle of the striations [39]. Uhrig et al. [36] published graphs for the burn rate modification for generic shapes like a cylindrical grain poured at the mid web, which can be used to predict the effect for similar grains.

2.5. Erosive Burning & Associated Modelling Approaches

While pressure is the most relevant parameter influencing the motor burn rate, there are also a number of other parameters that play a significant role, the most prevalent being erosive burning. Erosive burning is particularly present in long, slim motors. Erosive burning is the burn augmentation due to the influence of high-velocity flow crossing the burning surface. It occurs mainly at a low port to throat area ratio as this increases the speed of the flow in the core. It can lead to an increase in the pressure in the combustion chamber significantly or expose parts of the wall of the combustion chamber before burnout. Figure 2.30 shows how erosive burning can alter the pressure and thrust trace.

The erosive burning mechanism is believed to mainly work by increasing the heat transfer into the surface, accelerating the evaporation and decomposition of the surface by enhancing the mixing of the fuel and oxidiser on top of the diffusion flames on the surface of composite propellants [9], [40]. Many different models have been proposed for this complicated mechanism and many have done experiments to understand the phenomena better [41], [42].

Summary of erosive burning models

The majority of the internal ballistics models only use phenomenological heat-transfer theories and specific the Lenoir-Robillard expression. Even though this model is 60 years old it is still the most widespread used model. But there have been numerous attempts to replace it, Razdan and Kuo in the chapter about erosive burning in Fundamentals of Solid Propellant Combustion[43] have made a list with all the expressions from all the different models. They split the models into four big categories by the phenomena they use to describe erosive burning. These categories are briefly shown and explained below.

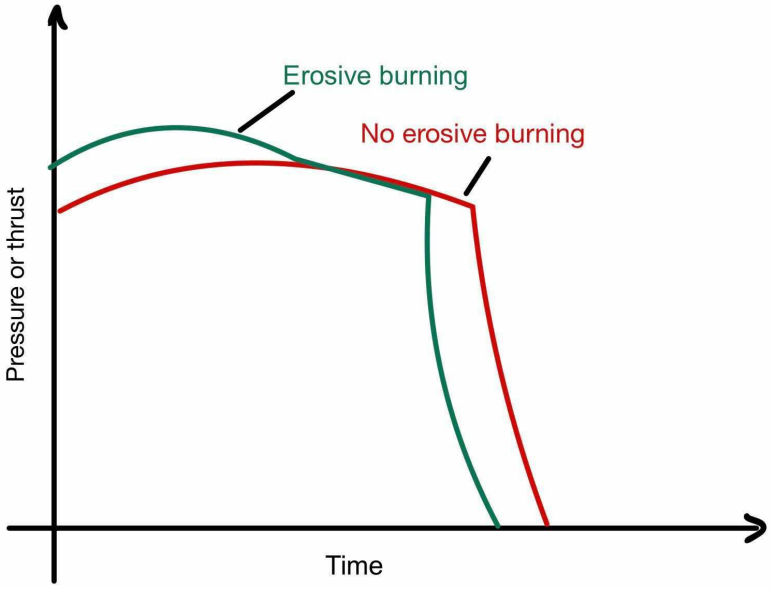

Figure 2.30: The difference in the thrust and pressure trace with and without erosive burning

1. **Phenomenological heat-transfer theories**
   These models state that the heat transfer back to the surface determines the burn rate and there is heat coming from the normal burning of the propellant and of convective heat transfer of the flow that is crossing the surface. The most used is the Lenoir-Robbillard expression but there are many models that model the heat transfer in different ways like Mukunda and Paul, Hasegawa and Dickinson and Ma et al. .

2. **Integral boundary-layer analysis**
   The integral boundary-layer analysis is based on an increase in heat transfer to the surface due to an increase in transport properties in the boundary layer caused by the turbulent cross flow. An example of an approach like this is the model from Lengelle [44].

3. **Modification of the propellant combustion mechanism**
   These models assume that the flame structure of the propellant changes which increases the rate of burning. The model from King [45] is an example where he assumes that the diffusion flame bends.

4. **Chemically reacting turbulent boundary-layer analysis**
   These methods are based on chemical and aerodynamic models and are direct numerical simulations or simplified situations which try to solve the problem by simulating the combustion itself in a boundary layer. The model from Razdan and Kuo [46] is a simplified 2D model of the boundary layer and the model from McDonald and Menon [47] is a direct numerical simulation considering a highly reduced set of chemical reactions.

The phenomena are evaluated by countless experiments ranging from probes in the propellant to X-ray movies of the core regression. These experiments give good agreement with all four methods, which is not extremely surprising as all of these methods use test data to some extent to calibrate their model. Therefore, it seems that the erosive burning effort is mostly about what kind of function to fit on data than anything else.

The general trends are clear, according to Landsbaum[41], 1) higher velocity leads to more turbulence at the surface and gives more erosive burning. 2) Erosive burning rate decreases when the base burn rate increases as it is more difficult to increase the heat flux of faster burning propellants. 3) Propellants with similar burning rates have similar erosive burning behaviour as the erosive burning rate is primarily dependent on flow conditions. 4) Erosive burning is lower in larger motors as the same gas velocity creates less turbulence at the flame zone in bigger motors. Lastly, Landsbaum also elaborates

on the threshold effect that this is most likely where the flow turns turbulent, however, this is hard to predict exactly and from an engineering point of view not interesting as this effect has little effect on the overall pressure of the engine[41]. The threshold effect does however make phenomenological heat-transfer theories make less physical sense, as they make erosive burning a function of the mass flux. These models try to solve this by including step functions. Below only the expression of Dickinson et al. is further elaborated on as this is the one used in the model.

Hasegawa and Dickinson

Dickinson et al. proposed a more simple expression than Lenoir and Robillard that is only a function of mass flow seen in Equation 2.17 [48]. In his paper, he also presented a relatively easy way to measure the burn rate in a solid rocket motor by using conduction probes.

$$\frac{r}{r_0} = 1 + K_d G \left(1 - \frac{G_{\text{cr}}}{G}\right) \tag{2.17}$$

Hasegawa changes Equation 2.17 to use non-dimensional mass-flux $\hat{G}$ instead of G dimensional mass flux, by dividing by the normal burning rate and propellant density (ρr_0), and makes erosive burning proportional to G^Y instead of G. He also adds the term D_p the hydraulic diameter and notes that K_1 is not constant for all motors even with the same propellant as erosive burning also depends on surface roughness, the curvature of the surface, port diameter, pressure gradient and local pressure[49]. Therefore, the expression proposed by Hasegawa seen in Equation 2.18 is not universal and relies heavily on empirical data for its coefficients and thus fails to fundamentally describe erosive burning. However, when experimental data is available the model is in good agreement with experiments [49].

$$\frac{r}{r_0} = \begin{cases} 1 + K_1 D_p^{-0.2} \left[G\left(1 - \frac{\hat{\sigma}_\sigma}{\hat{G}}\right)\right]^{1.2} & ;\hat{G} > \hat{G}_{\text{cr}} \\ 1 & ;\hat{G} \leq \hat{G}_{\text{cr}} \end{cases} \quad \hat{G}_{\text{cr}} = 10 \quad with \quad \hat{G} = \frac{G}{\rho_s r_0} \tag{2.18}$$

Highly aluminised propellant

Kamath et al. did measurements on erosive burning in highly aluminised composite solid propellent they concluded that agglomeration and retention of accumulates were not observed in high cross-flow conditions [50]. Furthermore, they noted that two-phase flow effects on erosive burning rate are not significant, and suggest this might be because of the dominance of surface heat release. In the study by Kamath et al. they conclude that a good burning rate correlation is found in terms of Mach number, axial distance and pressure, see Equation 2.19[50].

$$r_b(\text{ cm/s}) = r_b^0 + 0.849\left[M - 0.250P(MPa)^{-0.40}\right]^{0.886} \cdot P(MPa)^{0.901} \cdot \left[\frac{9.0}{x(cm)}\right]^{0.326} \tag{2.19}$$

2.6. Validation and Verification Cases

Experiments give valuable information for the characterisation and validation of models. This section will go over a few relevant experiments whose data will help validate the model described in chapter 3. Then chapter 4 will discuss the experimental data from tests of propellant for the DART solid rocket booster for pressure and erosive characterisation. Gudu et al. discuss a test with two pressure sensors that include strain gauges in between to get the pressure distribution along the motor length. The experiment from Gudu et al. is similar to the experiment done by the author discussed in chapter 3.

Olthof

Olthof at T-Minus Engineering B.V. has performed instrumented tests of their single grain and multi-grain motors [51]. The tests measure both the thrust with a load cell and the pressure with a pressure sensor at the head end bulkhead. They performed four single grain motor tests of which two fired nominally and provided a good baseline to determine the burn rate shown in Table 2.3. And some full-scale tests with different configurations, changing the total number of grains, this is data that therefore is suitable to determine the erosive burning characteristics.

Pressure coefficient a	$9.0x10^{-6}$ (m/s)
Pressure exponent n	0.40 (-)

Table 2.3: Burn characteristics propellant T-Minus note that this in SI units and thus has a reference pressure of 1 Pa [51]

The single grain motor tests operate between 5.5MPa and 6.5MPa and have a neutral burn progression. Figure 2.31 shows the pressure trace and shows that very good agreement between simulation is already found by Olthof[51]. As these single grain motors have no significant longitudinal effects the burn rate can be found by matching the model with the test data assuming the burn rate is only a function of pressure. This experiment also provides a good baseline to verify the grain burn back model together with the gas dynamic model for the ignition and trail off without erosive burning.

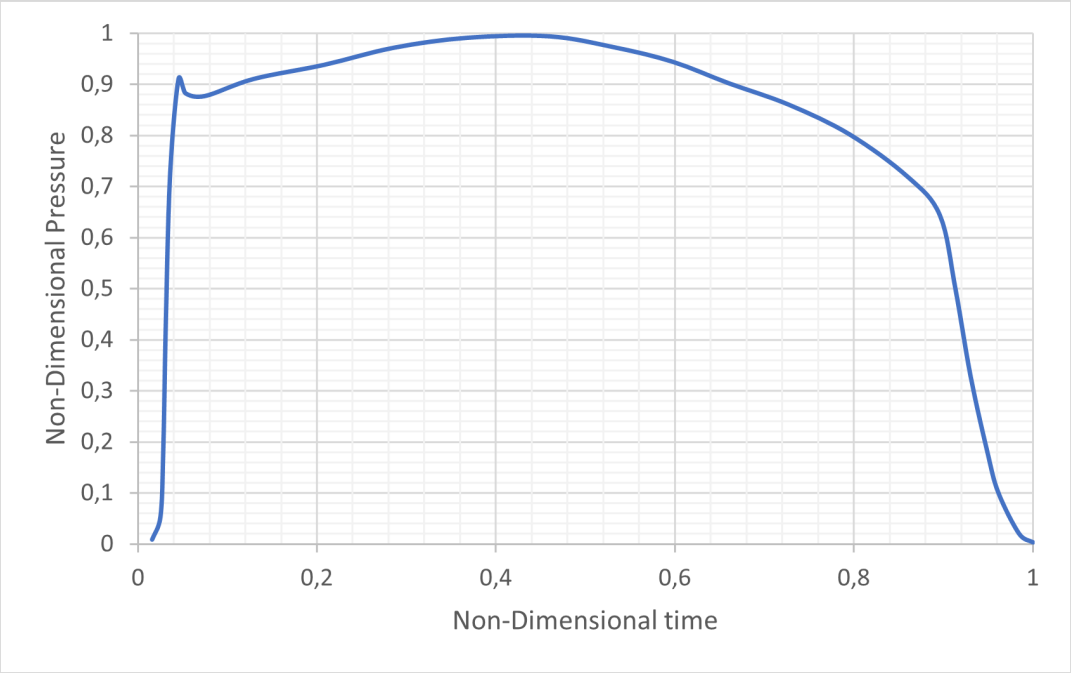

Figure 2.31: Pressure trace of the single grain test by T-Minus Engineering B.V. shows that for short motors the erosive burning effect is not present. Figure by Olthof[51]

For the multi-grain motor tests, erosive burning is clearly present and this provides validation data for a model that also considers longitudinal effects. The maximum pressure is significantly increased to a maximum of 8MPa and has a much longer trail off. Figure 2.32 shows the pressure trace of the full-scale motor which can be used as validation of the head end pressure in a one-dimensional model. It must be noted that a much better validation would be achieved if multiple pressure readings would be available to really validate the pressure drop over the motor. This is aimed goal of the experiment described in chapter 3.

Hasegawa et al.

Hasegawa et al. tested a rocket motor while investigating in detail the erosive burning phenomena in aluminised composite propellants using X-Ray diagnostics[49]. Using X-Ray they were able to fire the motor and accurately measure the regression over time. This is a valuable verification case for the erosive burning model and is especially usefull for the validation of the local burning rate as this can not be explicitly assessed from pressure data.

The data provided by Hasegawa et al. is especially valuable because the ignition gasses and the burn itself are separated and the erosive burning can be validated more separately. In Figure 2.34 the igniter, pressure can be seen to decrease already before full ignition of the motor. In addition Figure 2.34 shows the burn back of the propellant along the motor length. The test depicted on Figure 2.34 was done using propellant 1 from Table 2.4 with an initial gap between slabs of 5mm and a throat diameter

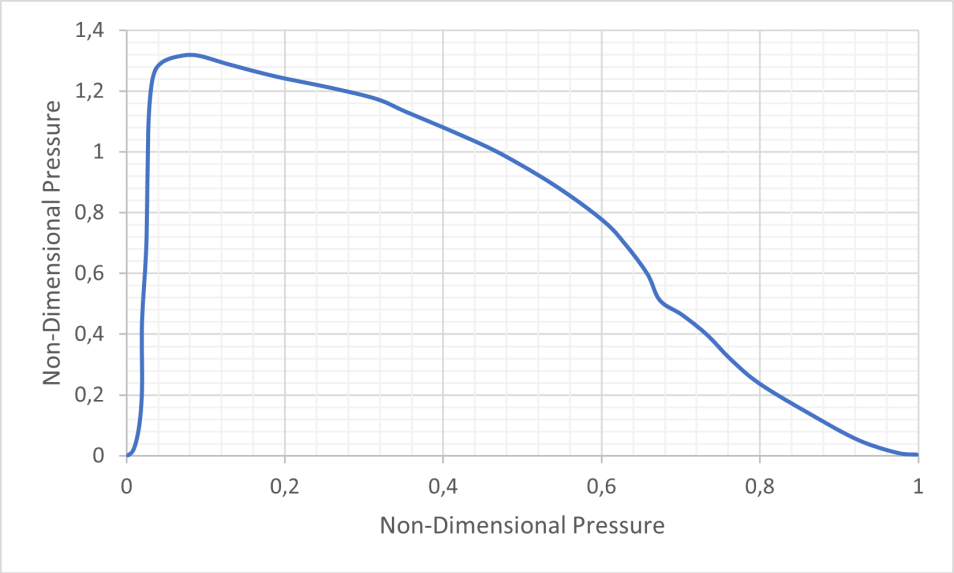

Figure 2.32: Pressure test of full-scale motor test 4 of T-Minus Engineering B.V. clearly shows erosive burning. The pressure trace would have looked similar to the single grain without erosive burning. Figure by Olthof [51]

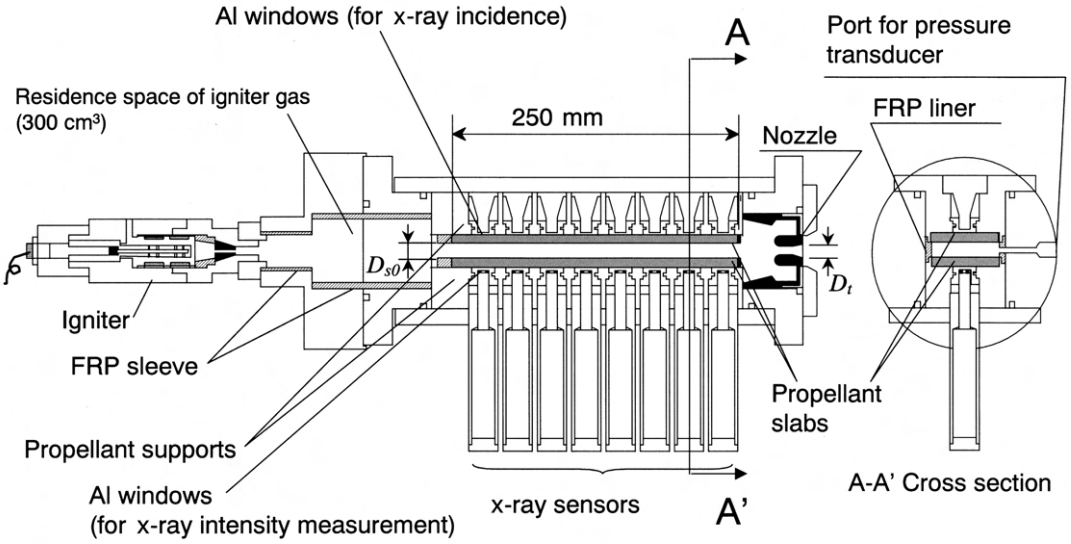

Figure 2.33: Test setup from Hasegawa et al. testing regression during motor burn using X-Ray intensity detectors. Figure by Hasegawa[49].

of 9.2mm. Erosive burning can clearly be seen in Figure 2.34 by the increased regression at the end of the motor where the mass flux is largest in this test at about 855 kg/m^2s.

Hasegawa et al. use a simple model from Dickinson [48] and were able to find the coefficient for Equation 2.17, however, they added a dependency to local pressure and hydraulic diameter. Equation 2.20 shows the parameters for the erosive burning coefficient.

$$
\begin{aligned}
K_1 &= K_2 \cdot P^{-0.7} \\
K_2 &= \begin{cases} 3.4 \times 10^{-4} & ;\ \text{propellant No. 1} \\ 7.0 \times 10^{-5} & ;\ \text{propellant No. 2} \end{cases}, \left[\mathrm{m}^{2.6}\ \mathrm{s}^{1.2}\mathrm{MPa}^{0.7}/\mathrm{kg}^{1.2}\right] \\
\frac{r}{r_0} &= \begin{cases} 1 + K_1 D_p^{-0.2} \left[G \left(1 - \frac{\hat{G}_{\mathrm{cr}}}{\hat{G}} \right) \right]^{1.2} & ;\hat{G} > \hat{G}_{\mathrm{cr}} \quad \hat{G}_{\mathrm{cr}} = 10 \\ 1 & ;\hat{G} \leq \hat{G}_{\mathrm{cr}} \end{cases}
\end{aligned}
\tag{2.20}
$$

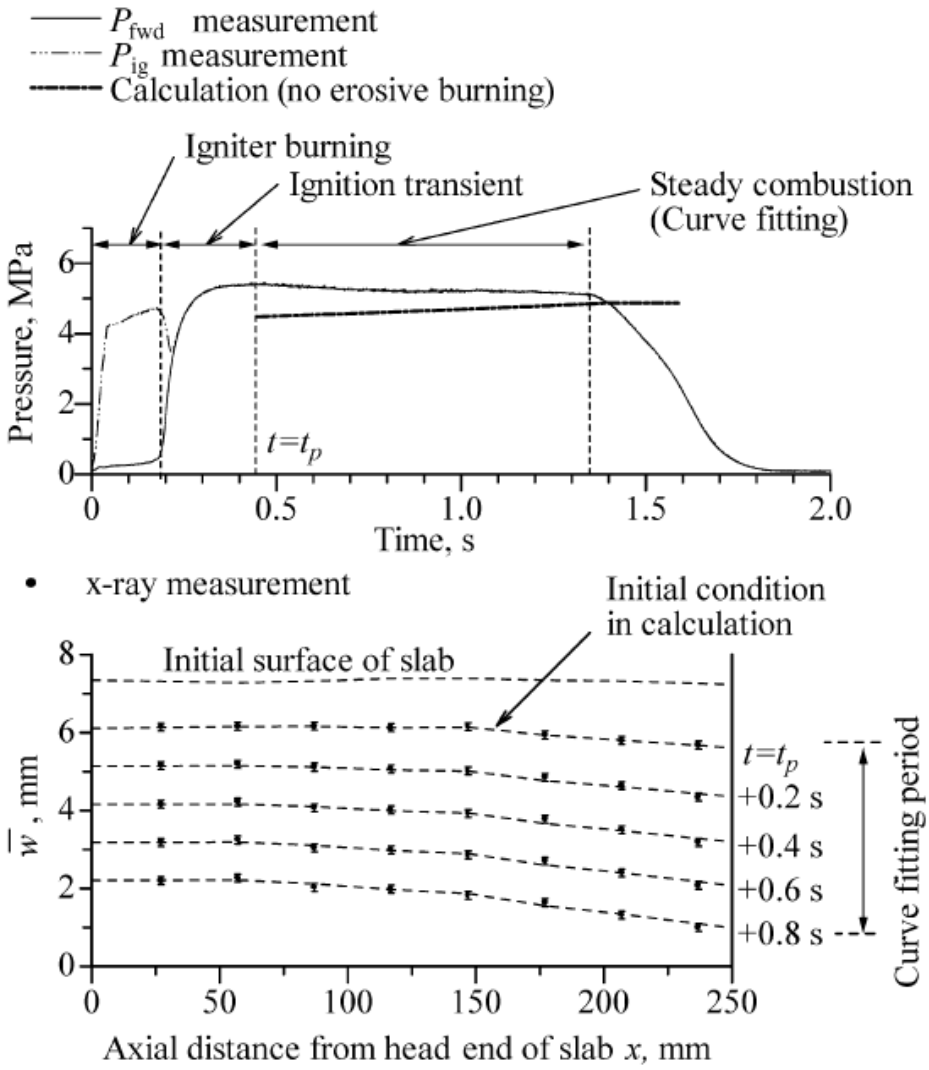

Figure 2.34: Pressure trace and grain burnback are measured by X-ray, which can be used to validate the geometry chance. Figure by Hasegawa[49].

	Propellant no. 1	Propellant no. 2
Composition, % by mass		
Oxidizer (AP)	69	68
Binder (HTPB)	17	12
Metal fuel (Al)	14	20
Additive (Fe_2O_3)	–	~ 0.5
Density ρ_s, g/cm^3	1.7	1.8
Linear burning rate r_0^a, mm/s	4.9	9.2
Pressure exponent n	0.3	0.4
Temp. sensitivity σ_p, %/K	0.155	0.076
Adiabatic flame temp [b], K	3041	3530
Mean molecular mass [b], g/mol	25.4	29.6
Specific heat ratio [b]	1.19	1.17

[a] 4.9MPa, 20deg.
[b] Frozen equilibrium calculation @ 5MPa.

Table 2.4: Propellant properties for the test to be used for validation. Table by Hasegawa et al. [49]

Gudu et al.

Gudu et al. static tested the SAGE-71 rocket motor and shows good agreement with their theoretical model using Razdan and Kuo's approach to predict erosive burning [7], [46]. With the strain gauges along the motor length, the pressure drop over the motor can be assessed at multiple points providing valuable information to validate the pressure over the motor from a gas dynamics model. The properties of the SAGE-71 are given in Table 2.5.

Weight	10.1kg
Length	1.28m
Diameter	71mm
Grain shape	star
Propellant	% weight
AP	71%
Al	16%
HTPB	9%
DOA	4%

Table 2.5: Properties of the SAGE-71 used by Gudu et al.[7]

Figure 2.35 shows the setup used for the static test with the SAGE-71 motor on erosive burning. Five strain gauges were placed to measure the expansion in diameter of the aluminium motor casing during firing. Figure 2.36 shows how the pressure trace can be recognised in the strain along the motor and the pressure drop along the engine can be seen.

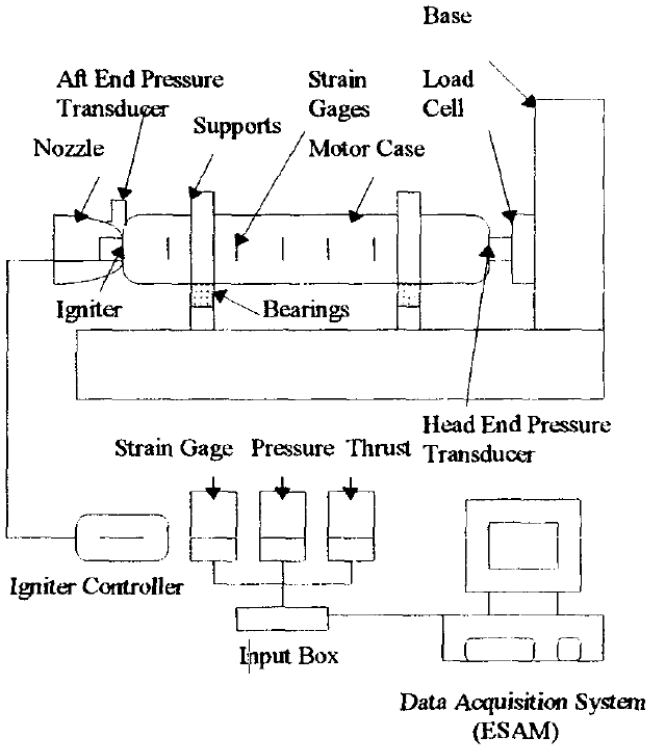

Figure 2.35: The static test system used in the study on erosive burning by Gudu et al.[7]

Gudu et al. do not provide the grain geometry specifically and therefore this data can not be used to validate the model. However, the provided pressure drop for a similar engine with a typical star grain can be compared. Possibly this can then be used to verify the gas dynamic model to an extent.

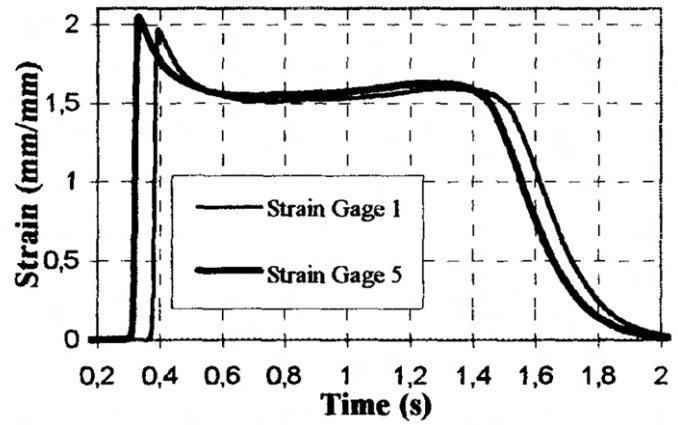

Figure 2.36: The strain at different points along the solid rocket motor shows the slight delay in pressurisation of the aft and front of the motor and the pressure drop over the motor. Figure by Gudu et al.[7]

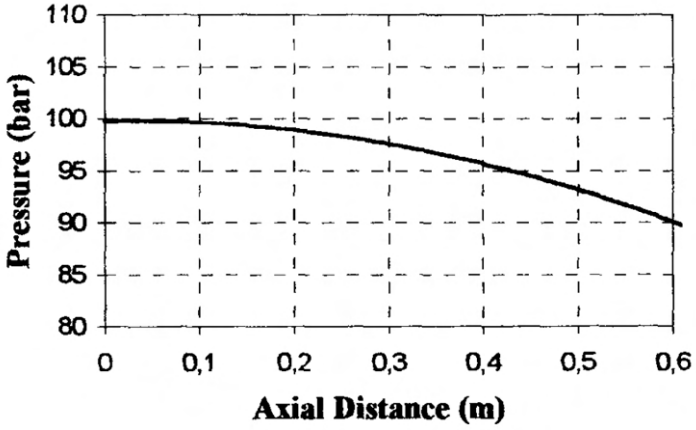

Figure 2.37: The pressure along the motor from the strain measurements and pressure sensors show the pressure drop over the motor. Figure by Gudu et al.[7]

3

Methodology

This chapter will go over the methodology taken to answer the research questions. The work of this thesis is roughly divided in a theoretical model and experimental work to be compared to each other.

3.1. Description Numerical Model

The model was made to assess the influence of grain length on erosive burning to answer the research question. First, a one-dimensional model for gas dynamics was considered like implemented by Cavallini [23]. A quasi zero-dimensional model was implemented as this shortened the development time and proved sufficiently accurate to answer the research question. In chapter 8 it is further elaborated on what a one-dimensional model could add.

The control volume of the model is bordered by the burning surface, motor casing and throat. The state variables for the gas-dynamic model are the chamber pressure and chamber volume. The state of the grain burn back model is determined by the minimum distance function entirely. The connection between the grain burn back model and the gas-dynamic model is made by providing the burn area and port area over the length over the motor to the gas dynamics module and the burn rates over the length over the motor back.

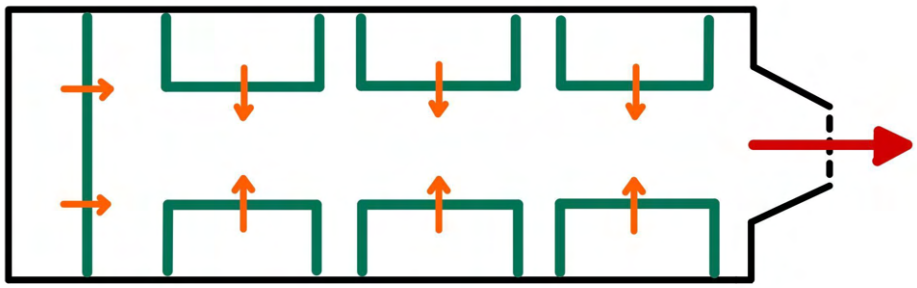

Figure 3.1: Control volume for the model with the green borders adding mass and the throat removing mass

The model is implemented in Python 3.9 and is split up into two modules, one modelling the burn back of the propellant and the other modelling the gas dynamics and burn speed. In Figure 3.2 a flowchart of the different steps and processes that are involved in finding the pressure in the motor chamber over time.

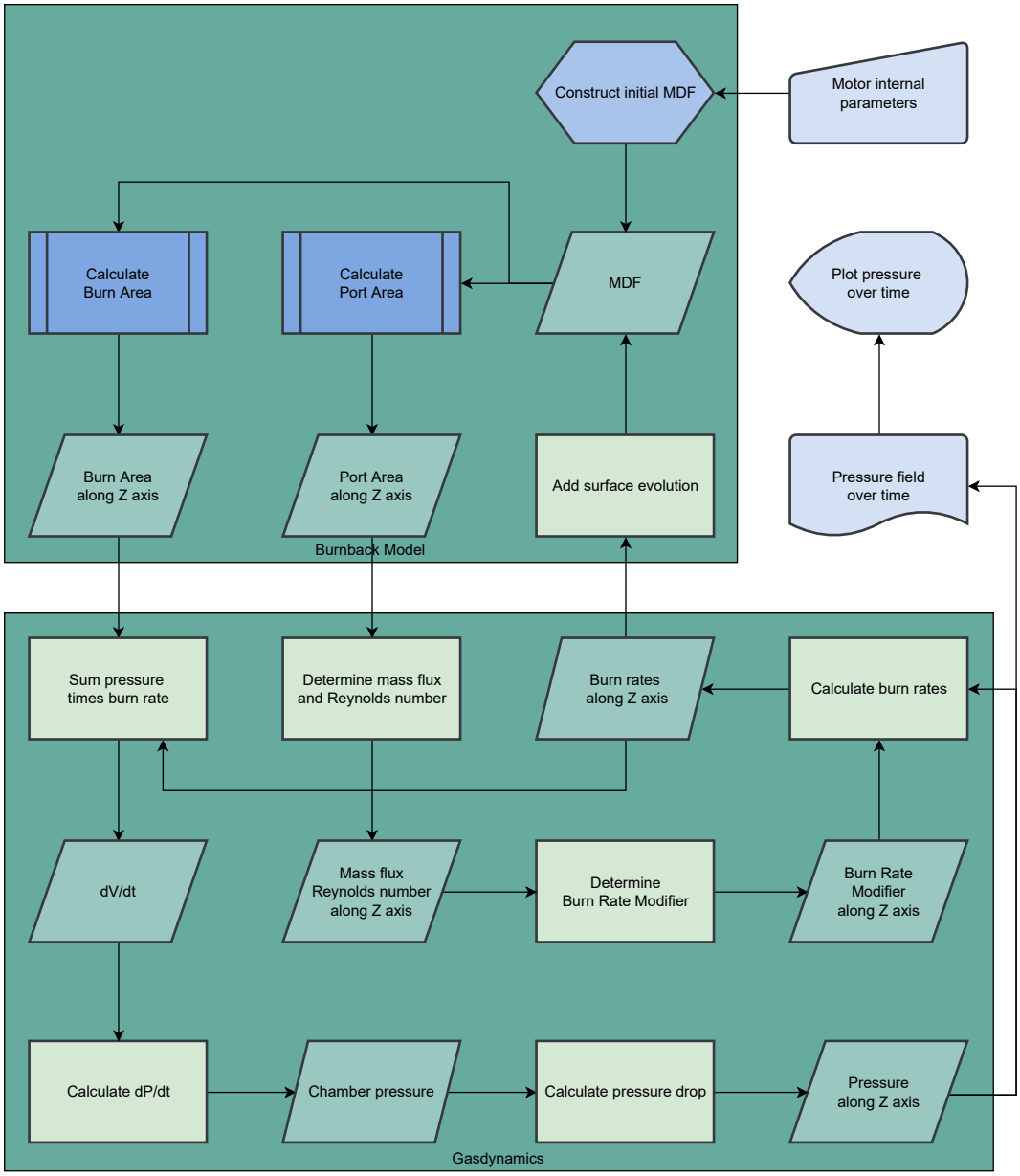

Figure 3.2: Flowchart of the program for modelling

3.1.1. Minimum Distance Function

The grain burn back model keeps track of how much propellant was burned and what the shape of the burning surface is over time. There are multiple possible models to keep account of these changes in this work the Minimum Distance Function (MDF) is used. In Figure 2.2 the MDF was already briefly introduced as an Eulerian approach to accounting for the location of the burning surface with respect to the Eulerian reference frame of the motor.

MDF is strong in surface evolution tracking, however, only surface evolution normal to the surface is possible. One of the downsides of using a MDF is that the properties of the grain geometry needed for the gas dynamics model, burn area and port area, are not directly given. Instead an algorithm is needed to evaluate the MDF to acquire the burn area and port area.

First, this section will briefly explain how the minimum distance function is initialised, then after the algorithm to find the burn area and port area, Equation 3.4 and Equation 3.5, are described.

Minimum Distance Function Initialisation

The initialisation of the minimum distance method is best explained by means of an example. In Figure 3.3 one smoke grain and two bates grains are shown as a test case.

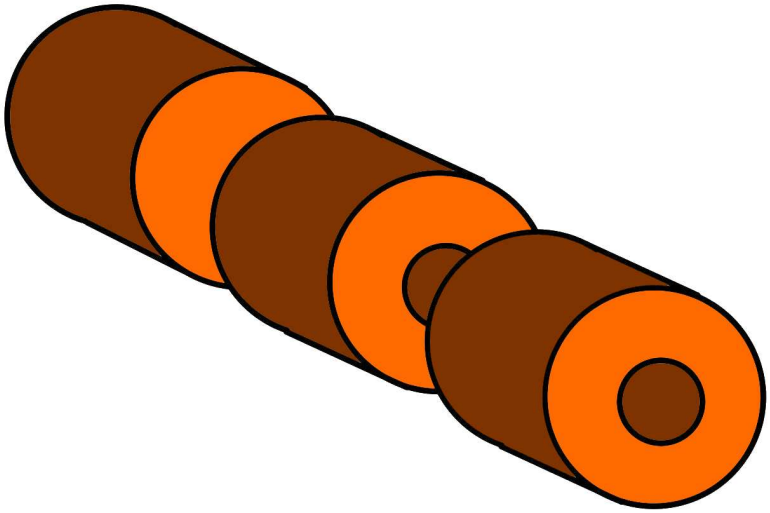

Figure 3.3: Test case for minimum distance function consisting of one smoke grain of 0.5m long at z = 0 and two BATES grains of 1m long with 0.05m spacing and a 0.5m diameter core, all with outer diameter 1m.

The geometry is then translated into a minimum distance function which for each point on the mesh finds has the value of the distance to the closest surface. This is done by creating a minimum distance function for each surface which is then combined by keeping the minimum value for each location. For example in Figure 3.4 the minimum distance from the inner cylinder is given by Equation 3.1 and in Figure 3.5 the distance from the surface of the smoke grain by Equation 3.2, when combined, taking the minimum value for each point, this gives Figure 3.6.

$$MDF_{cylinder}(x,z) = R_{cylinder} - x \tag{3.1}$$

Equation 3.1 takes the radius of the cylinder minus the x-coordinate to find the minimum distance from the cylinder at that location.

$$MDF_{surface}(x,z) = z - z_{surface} \tag{3.2}$$

Equation 3.2 takes the z-coordinate minus the z-coordinate of the surface to find the minimum distance from the surface.

$$MDF_{combination} = \text{if}(MDF_1 < MDF_2)\text{then}MDF_1\text{else}MDF_2 \tag{3.3}$$

Equation 3.3 finds the minimum distance to the combination of the two surfaces by comparing the MDF values and taking the lower value.

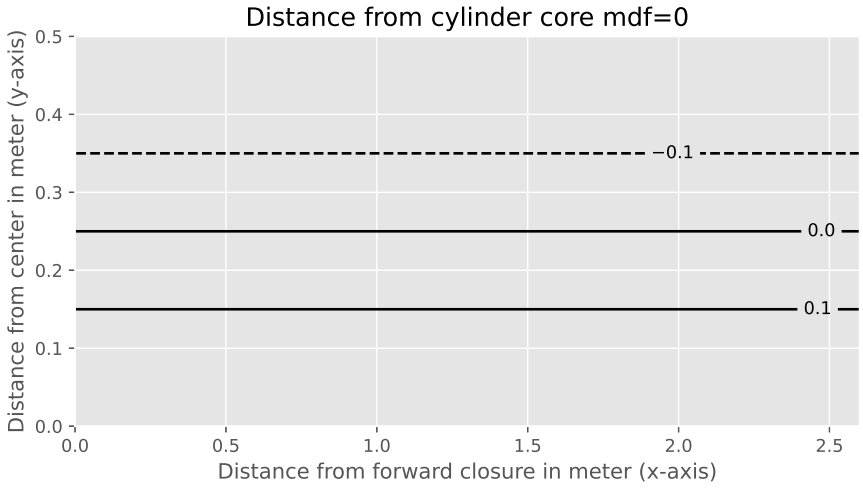

Figure 3.4: Surface from the core cylinder with a diameter of 0.5m.

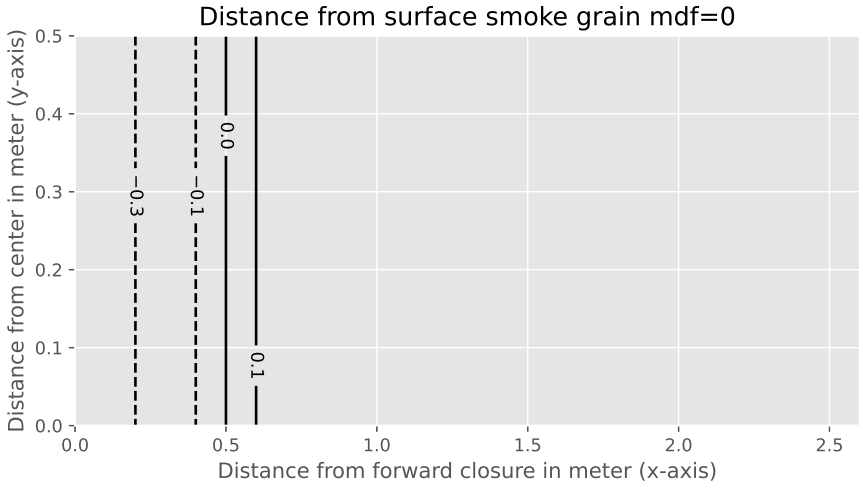

Figure 3.5: Surface from the smoke grain surface at z = 0.5m.

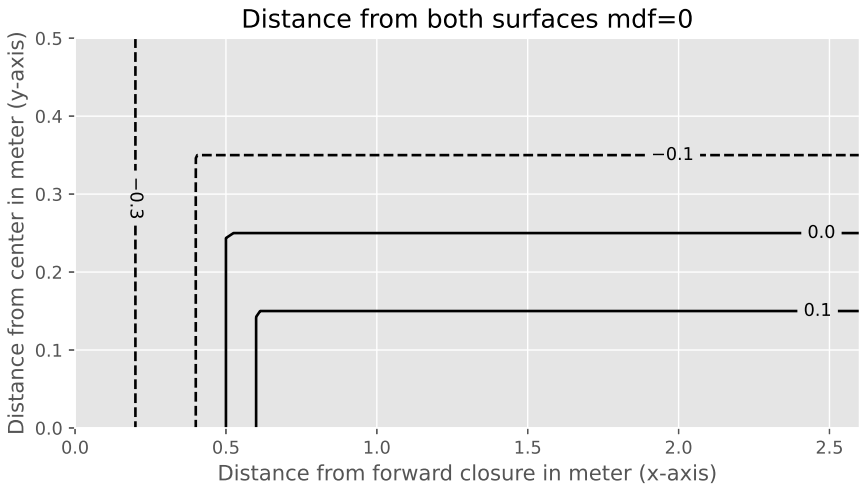

Figure 3.6: Combination of the minimum distance function of the surface of the smoke grain and cylinder.

To get to the test case the top and bottom surfaces of the grains are also added which results in the MDF that can be found in Figure 3.7. This shows how much the surface needs to regress to reach that location. The surface propagation is done by simply adding the amount of surface propagation to each value of the minimum distance function.

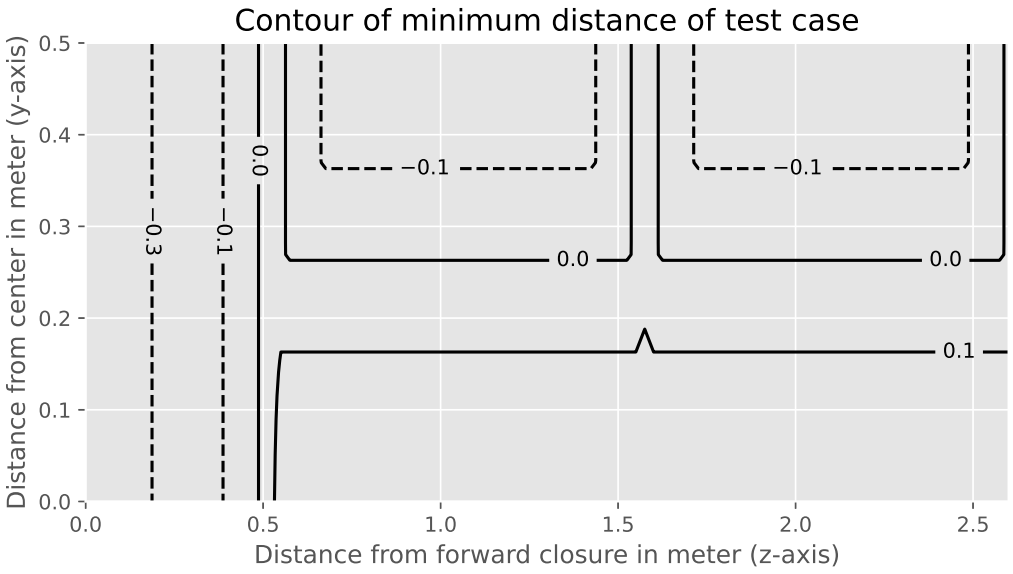

Figure 3.7: Minimum distance function of the test case.

Derive grain parameters from MDF

Equation 3.4 and Equation 3.5 are algorithms that find the burn area and port area for each slice of the motor along the z-axis like shown in Figure 3.8.

$$(A_b)_i = f(MDF(t), z_{i-1/2}, z_{i+1/2}) \tag{3.4}$$

$$(A_p)_i = f(MDF(t), z_i) \tag{3.5}$$

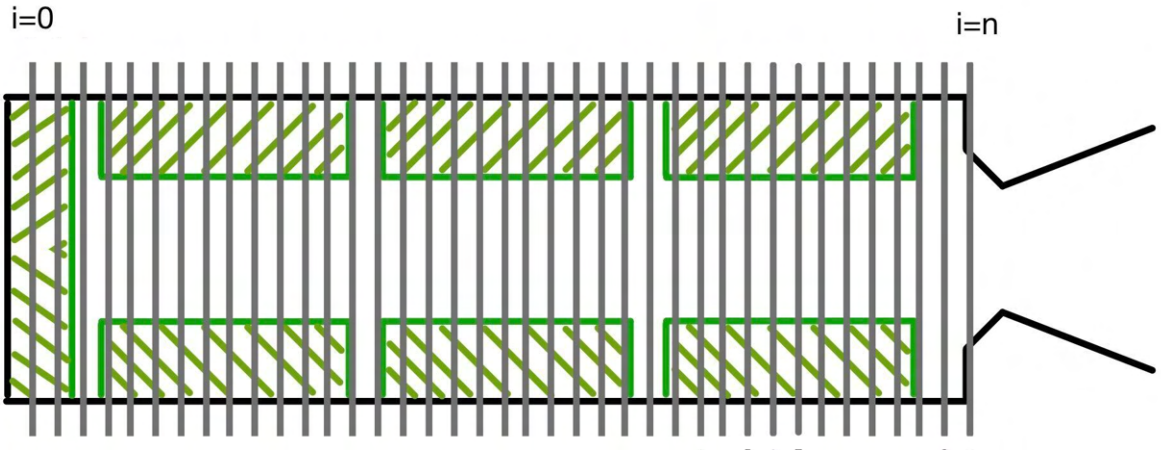

Figure 3.8: Motor divided up in slices where the properties burn area and port area are determined.

The algorithm made by Wilcox [8] works by walking through all mesh points in the minimum distance function and checking if the sign of the minimum distance function is different at the neighbouring cells. If the sign changes then Equation 3.6 and Equation 3.7 is used to determine the distance of the surface from the location of the mesh point.

$$x_{surface} = x_{meshpoint} + \Delta x_{distancetoneighbour} \cdot \frac{|MDF_{meshpoint}|}{|MDF_{meshpoint}| + |MDF_{neigbour}|} \tag{3.6}$$

$$z_{surface} = z_{meshpoint} + \Delta z_{distancetoneighbour} \cdot \frac{|MDF_{meshpoint}|}{|MDF_{meshpoint}| + |MDF_{neigbour}|} \tag{3.7}$$

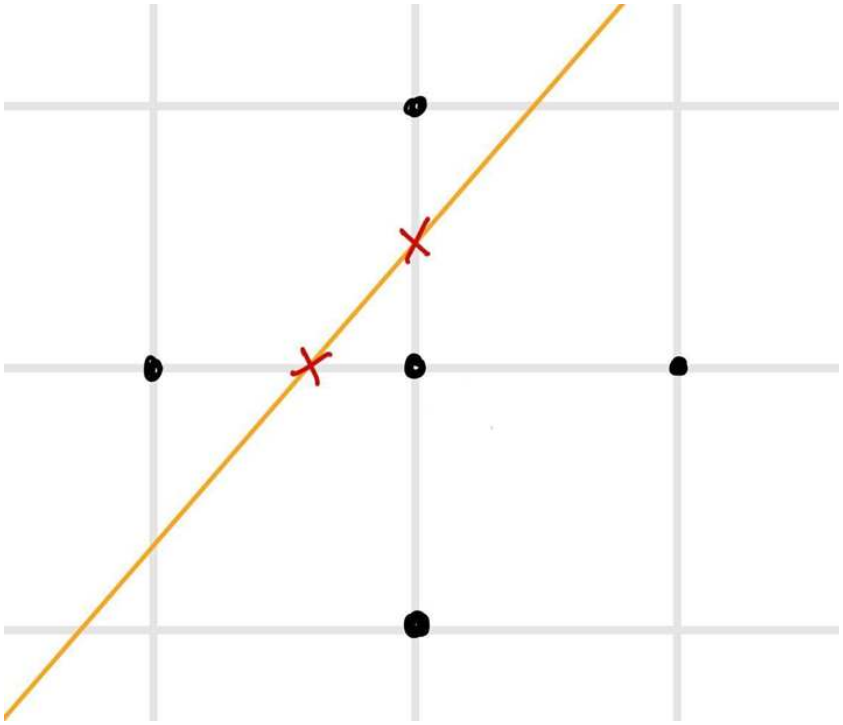

Figure 3.9: The mesh point with its neighbours with the intersections depicted with red crosses.

A list of these intersections is then made for each grain and then sorted such that by finding the distance between these intersections the surface can be found. These pieces of surfaces are each weighted with the radius to add up to the burn area see Equation 3.8. For the port area the average off the distance from the core off all points in that slice is taken which is equal to the x coordinate, see Equation 3.9.

$$(A_b)_i = \sum \left[\sqrt{(\Delta x)^2 + (\Delta z)^2} \cdot \pi \cdot x\right]_{points} \quad \text{for all points within } z_{i-\frac{1}{2}} \text{ and } z_{i+\frac{1}{2}} \tag{3.8}$$

$$(A_p)_i = \bar{x}_{points} \quad \text{for all points within } z_{i-\frac{1}{2}} \text{ and } z_{i+\frac{1}{2}} \tag{3.9}$$

3.1.2. Gas dynamics

The gas dynamics are modelled assuming one constant pressure over the entire chamber. The chamber pressure is the state variable using the mass input from the burning surfaces, the mass output of the nozzle and the change in chamber volume as inputs. Equation 3.10 shows how the gradient of the chamber pressure is found, the input for A_b, the burning surface, is gotten from the minimum distance function and the input for r_b, the burn rate, is gotten from the propellant burning rate.

Equation 3.10 is a mass balance translated to pressure with the ideal gas equation with the addition of pressure change with volume as the volume is not constant over time.

$$\frac{dP_0}{dt} = \frac{R \cdot T_c}{V_c} \cdot (\dot{m}_{nozzle} - \dot{m}_{nozzle}) - \frac{P_c}{V_c} \cdot \frac{dV_c}{dt} \tag{3.10}$$

The mass flowing out of the chamber when the pressure in the chamber is above the critical pressure, and the flow is supersonic is described by Equation 3.11.

$$\dot{m}_{nozzle} = P_c \cdot \frac{A_t}{c^*} \quad \text{for } P_c > P_a \cdot \frac{\gamma + 1}{2}^{\frac{\gamma}{\gamma - 1}} \tag{3.11}$$

Then Equation 3.12 for subsonic flow, an orifice model [52] approximates the mass flow through the nozzle assuming an orifice coefficient of 0.85.

$$\dot{m}_{nozzle} = C_{nozzle} \cdot A_t \cdot \sqrt{\frac{2 \cdot P_c}{R \cdot T_c} \cdot (P_c - P_a)} \quad \text{for } P_c < P_a \cdot \frac{\gamma + 1}{2}^{\frac{\gamma}{\gamma - 1}} \tag{3.12}$$

When the pressure is equal to or lower than the ambient pressure then the mass flow over the nozzle is set to zero to avoid negative values in Equation 3.12.

$$\dot{m}_{nozzle} = 0 \quad \text{for } P_c =< P_a \tag{3.13}$$

Equation 3.14 finds the mass addition of the burning of the propellant by multiplying the local burn area by the local burn rate, summing those together and multiplying by the density of the propellant.

$$\dot{m}_{burning} = \rho_p \sum_{i=0}^{n} (A_b)_i \cdot (r_b)_i \tag{3.14}$$

The change in volume over time is found by the velocity of the regression of the surface times the area in Equation 3.15

$$\frac{dV_c}{dt} = -\sum_{i=0}^{n} (A_b)_i \cdot (r_b)_i \tag{3.15}$$

The most important assumptions for this method are:

1. $\frac{dT}{dt} = 0$ the temperature of the gas in the chamber stays constant at the adiabatic flame temperature. After doing some simulations introducing Equation 2.14 it was found that the temperature mostly is constant except for the first 50 milliseconds.

2. $\frac{dP}{dx} = \frac{dT}{dx} = 0$ the pressure and temperature are equal over the motor using lumped parameters.

3. $C^* = Constant$ c-star varies with temperature as $C^* = \frac{\sqrt{RT_c}}{\Gamma}$ but due to the temperature being constant this is also constant even if the combustion temperature may vary with different pressures.

4. Combustion is instantaneous and the flow in the chamber is non-reactive.

5. Gas behaves like ideal gas, this is needed to translate the mass balance to a state equation for chamber pressure.

3.1.3. Propellant burning model

The base burn rate is determined with the St. Robert's or Vieille's law in Equation 3.16 with coefficients that are determined by single grain experiments.

$$(r_b)_i = \eta_i \cdot a_b \cdot (P_i)^{n_b} \tag{3.16}$$

Determine mass flux

All of the erosive burning models require mass flux in some way or form. Therefore this section describes the method used to model the mass flux over the motor. The main assumption required to get to a mass flux is steady-state mass flow through the motor, only moving in one direction out of the motor with uniform distribution over the port area.

$$G_n = \sum_{i=0}^{n} \left[(r_b)_i \cdot (A_b)_i \right] / (A_p)_n \tag{3.17}$$

Erosive burning: Dickens

This is taken from Hasegawa[49] who determined coefficients for the method originally proposed by Dickinson[48]. The method is based on mass flux, pressure, base burn rate and hydraulic diameter. The main reason for choosing this method over others is its simplicity

$$G_{cr} = 10 \cdot \rho_p \cdot r_{b0} \tag{3.18}$$

Equation 3.18 gives the critical mass flux from where erosive burning starts as a function of propellant density and base burn rate. This means that there will be erosive burning if the blowing of the main flow is ten times higher than the blowing of the surface without erosive burning.

$$\begin{aligned} K_2 &= 1.02e-3 [m^{2.2} s MPa^{0.7}/kg] \\ (K_1)_i &= K_2 \cdot (P_i/(1[MPa]))^{-0.7} \end{aligned} \tag{3.19}$$

Equation 3.19 has the coefficients as determined by Hasegawa [49] for their propellant formulation No. 1 which is similar to the propellant used in the DART Booster from T-Minus Engineering. Using this method changes the coefficient K_1 with pressure to have a smaller erosive burning coefficient with higher pressure.

$$\eta = \frac{r_b}{r_{b,0}} = K_1 \cdot D_h^{-0.2} \cdot (G - G_{cr}) \text{ when } G > G_{cr} \tag{3.20}$$

$$\eta_i = 1 + (K_1)_i \cdot (D_h)_i^{-0.2} \cdot (G_i - G_{cr}) \cdot (G_i >= G_{cr}) \tag{3.21}$$

Equation 3.20 by Dickens gives the total burning rate over the base burn rate also referred to as η. As the burn rate is not constant along the motor length Equation 3.21shows the implementation for each segment, where the hydraulic diameter and mass flux are taken locally from the port area and mass flow.

Flame spreading

Not all burning surfaces are ignited at once, some finite flame spreading speed as discussed in Figure 2.4. This is done by making a table of ignition timing for each z-location of the motor which then is compared, see Equation 3.23, to the time and turns on the burn rate at that location. Equation 3.22 was found by matching to the ignition behaviour observed during testing and does assume that no significant amount of gas is produced by the igniter. The ignition speed needed to get to this table is in the same order of magnitude as the flame speed in Figure 2.4.

$$t_{i,ignition} = \log\left(1 + 0.17 \cdot \frac{z_i}{z_{max}}\right) \tag{3.22}$$

$$(r_b)_i = (r_b)_i \cdot (t_{i,ignition} < t) \tag{3.23}$$

Hump effect

The hump effect is implemented in a simple lookup table, see Figure 3.10, that has a burn rate modifier depending on the web thickness of the grain by determining the coordinate of the burning surface.

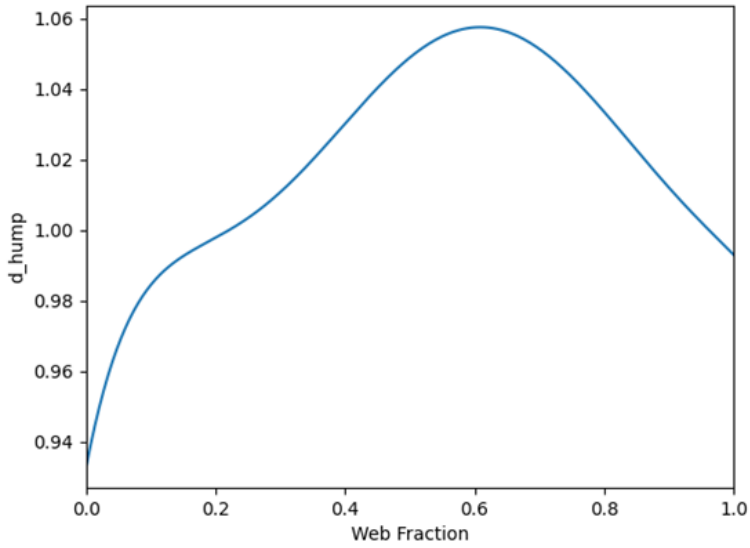

Figure 3.10: Graph of the lookup table for the burn modifier based on simulations form [36]

The shape and magnitude of the change in burn rate is taken from the data of Uhrig et al. [36] but it is non-dimensionalised, by dividing over the average burn rate, to be used as a modifier to be multiplied with the erosive burning modifier and base burn rate.

$$r_b = r_{b0} \cdot \eta \cdot \delta_{hump} \tag{3.24}$$

3.1.4. Pressure drop over motor

The model described above gives the area and mass flow over the motor. The model assumes constant pressure and density over the chamber, which would mean there would not be any pressure drop. However, in reality, there is and this can be up to 10% [6]. Two approaches are put forward, using the port area or mass flow and port area to approximate the pressure drop. The port to throat area ratio should give the Mach number if the gas was ideal and there was no mass or energy exchange. In reality, this is not true as there is significant mass addition in the chamber. This also assumes uniform flow in the chamber and a non-significant boundary layer.

$$\left(\frac{(A_p)_i}{A_t}\right)^2 = \frac{1}{M_i^2}\left[\frac{2}{\gamma+1}\left(1+\frac{\gamma-1}{2}M_i^2\right)\right]^{\frac{\gamma+1}{\gamma-1}} \tag{3.25}$$

$$\frac{(p)_i}{p_t} = \left(1+\frac{\gamma-1}{2}M^2\right)^{\frac{-\gamma}{\gamma-1}} \tag{3.26}$$

Equation 3.25 and Equation 3.26 can be used for analysis and comparison to the experimental data. However, this pressure drop does not work in conjunction with the erosive burning model as both influences the burning at higher Mach numbers. Therefore, it seems that current erosive burning models with exponents that are gotten experimentally account for both effects.

3.2. Experiment

Commonly with solid rocket motor testing the pressure at the forward closure, mostly because of easy access, however, this gives only a zero-dimensional view of the pressure field. In order to work towards a better understanding of the flow field in the solid rocket motor and provide one-dimensional verification for simulations for motors with high aspect ratio.

A test method is proposed using the expansion of the motor casing in order to derive the static pressure over the motor. The expansion of the motor is measured using strain gauges. This provides

an alternative non-intrusive measurement method over pressure transducers that are placed inside the combustion chamber. In solid rocket motors that have the propellant grain bonded to the case, the thickness and therefore stiffness of the wall vary both over the length motor and the time of the burn. However, in motors with free-standing grains the chamber does not vary due to changes in thickness.

The experiment was designed to be verified in stages. First, the strain gauges were put on a piece of metal with known stiffness to test the system and verify the data acquisition system was working. Then a small section of the motor was hydrostatically tested, by pressurising it with water. This was done to check the relationship of strain with pressure in the pressure vessel during cold conditions. Then lastly a validation test would be done during a motor fire with strain gauges, pressure sensor and temperature sensors.

3.2.1. Experiment design

The experiment was derived from an experiment done by Gudu et al. [7] and can be seen in Figure 2.35. The main difference was the absence of the aft end pressure transducer next to the nozzle as this would have meant a redesign of the nozzle assembly which was not possible from a cost and risk perspective. And the addition of temperature sensors next to the measurement locations to be able to compensate for the thermal expansion of the motor.

As first of the development, the general system was thought out and some tests were done with the measuring equipment. During this process Figure 3.11 was drawn out to do a system test. It was chosen to do a quarter bridge strain gauge over a half or full bridge. A half-bridge would have been better if someplace without strain could have been found to compensate for expansion due to temperature change. However, as there is no such place on the pressure vessel to make sure you measure just one strain a quarter bridge was chosen. The circuit used is most commonly named Quarter Bridge Type I [53].

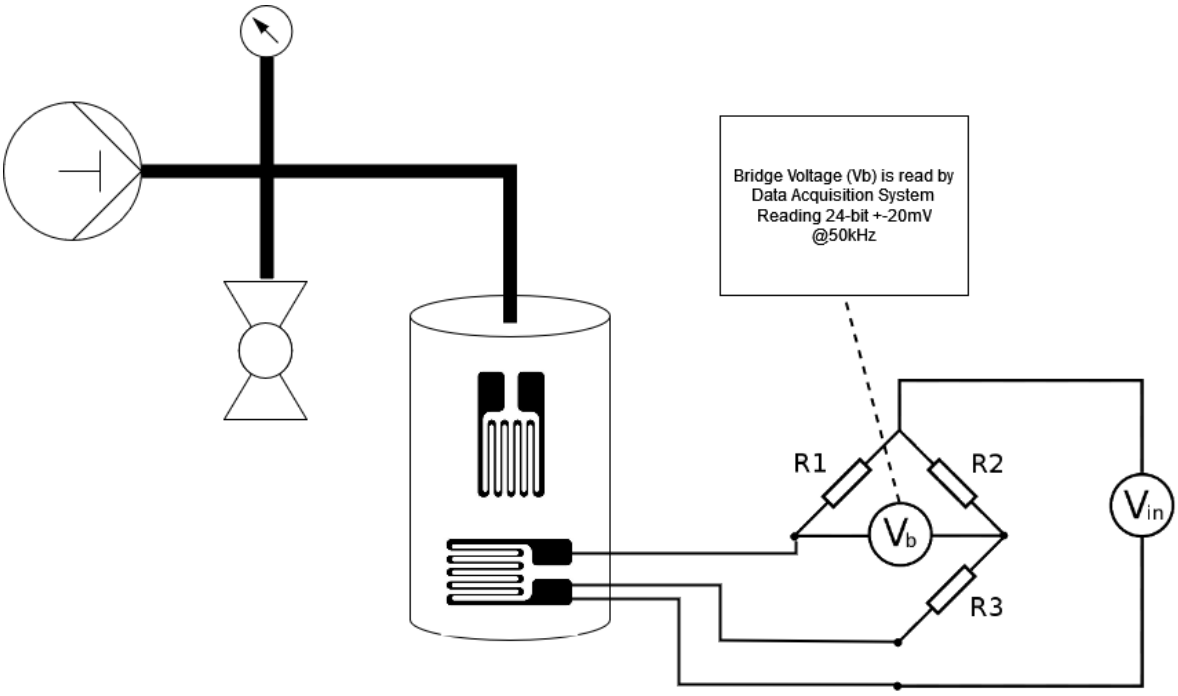

Figure 3.11: Diagram of the test setup with a hydraulic pump, pressure relieve valve, pressure gauge and pressure vessel with two strain gauges. The strain gauges are read off by a quarter Wheatstone bridge and a data acquisition system.

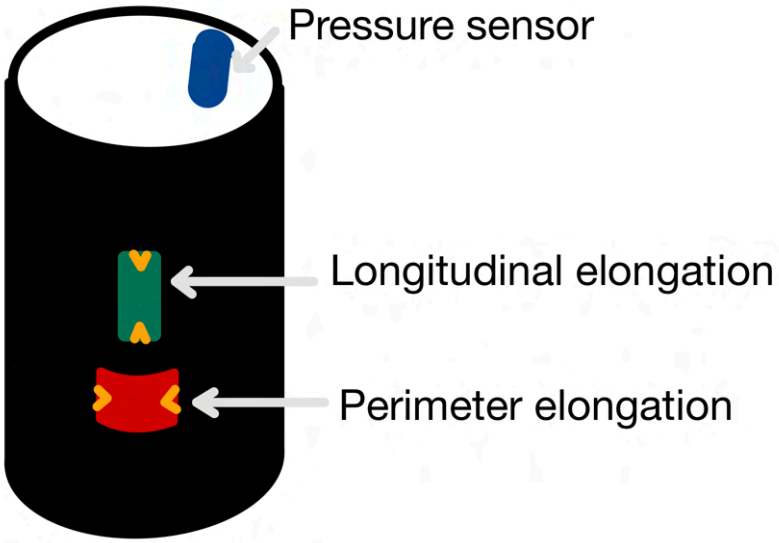

Figure 3.12: Overview of the strain gauge placement on the pressure vessel for the hydrostatic verification test.

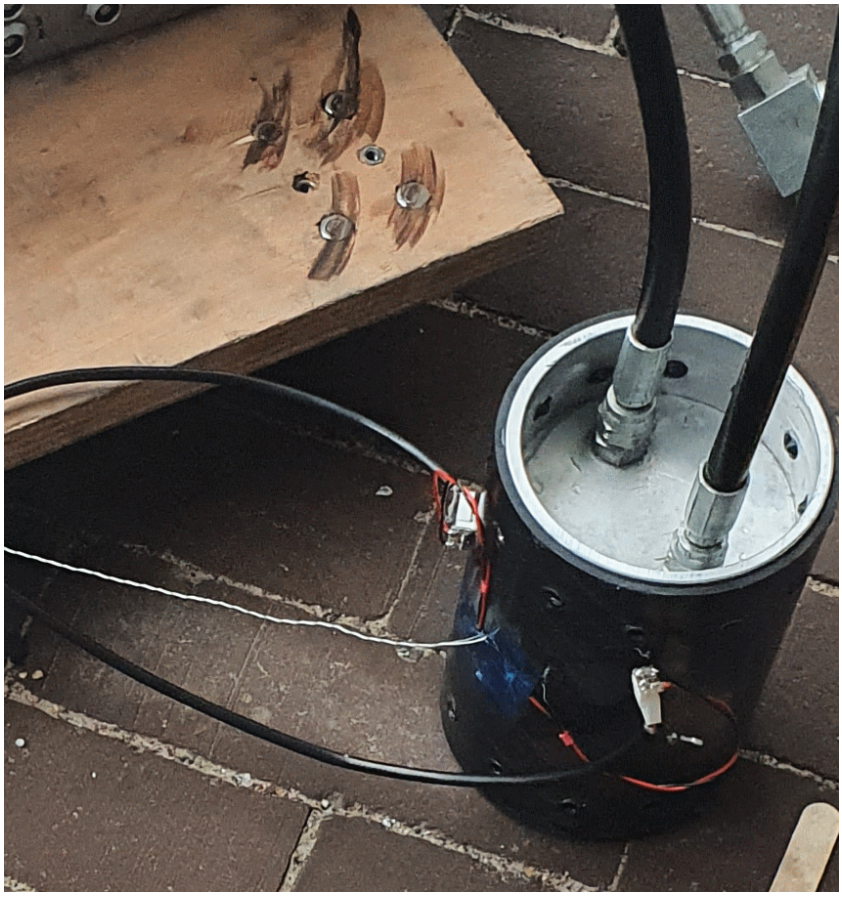

Figure 3.13: Picture of the test setup

The second step in the development of the test was to set up 4 strain gauge measurement locations and bring the measuring speed up to 50.000Hz in order to capture the reflections from ignition between the forward closure and nozzle. This was above the estimated minimum of 5.000Hz found by dividing the distance in between the four stations on the motor by the speed of sound of the hot gas, see Equation 3.27. The main goal of this high sampling speed was to validate the gas dynamic model

during start-up. This did not fit in the scope of this thesis, however, this verification data is valuable for further attempts to modelling ignition transients.

$$\left(\frac{\Delta z_{station}}{\sqrt{\gamma RT}}\right)^{-1} = \text{Minimumsamplingspeed} \tag{3.27}$$

In order to achieve this high sampling rate, a compact remote input-output (cRIO) was used by National Instruments (NI) using their FPGA interface to acquire the voltage readings from the analogue to digital converters and put in a First in First out buffer (FIFO buffer). The microcontroller then collected this in batches and wrote this away into non-volatile memory. This is described in more detail in the documentation from NI **NI FPGA**.

Another part of the second step was making the test setup ruggedized to be used in a muddy field instead of lab conditions. All the cables were made longer to make sure the data acquisition system was at safe distance from the motor while taking into account that the added resistance of the cable would not cause the measurement to be too noisy or outside of the measurement range. Network cables were low resistance enough and have the added benefit of already being shielded, some connectors were made and resistors selected. Due to the large measuring range of the data acquisition of +-20mV the low accuracy resistors of 1% precision can be chosen as a lower accuracy resistor in the Wheatstone bridge will put a DC offset on the measured signal.

Lastly, for the actual test, the addition of a generator increased the noise significantly and thus needed proper grounding to reduce this slightly. The noise produced by the generator was at around 20kHz which is above the timescale that is of most interest. Therefore, the data is put into a moving mean filter to keep the magnitude and gradient of the physical rise intact while smoothing most of the noise out, as a stopband or lowpass filter could decrease the gradient of the slope.

3.2.2. Test setup

The test setup is not changed from a test without strain gauges other than attaching the strain gauges with superglue with a piece of tape on top of it for protection and easier alignment, this can best be seen in Figure 3.16. The general setup can be seen in Figure 3.15. It is made from a truss that is put in the ground with some spikes and tensioned with ground ankers at 3 places with tension straps. The pressure sensor is placed in the forward closure located next to the load cell that measures the thrust. The strain gauges run to the data acquisition system with each their own cable. Figure 3.14 shows the locations of the pressure sensor and strain gauges, with the exact location along the length of the casing given in Table 3.1.

Location	% of length
Location 1	0 %
Location 2	33%
Location 3	77%
Location 4	100%

Table 3.1: The location along the length of the motor as a percentage of the total length of the motor.

Figure 3.14: Schematic of the placement of the sensors, note that all locations are chosen next to spacing in between the propellant segments or grains.

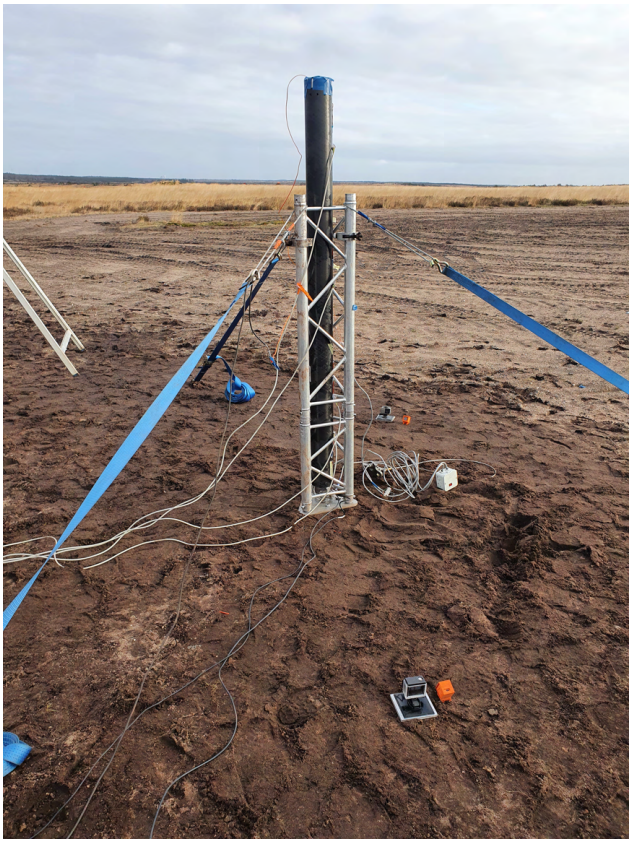

Figure 3.15: Overview of the test setup showing the cables that run from the strain gauges to the data acquisition system.

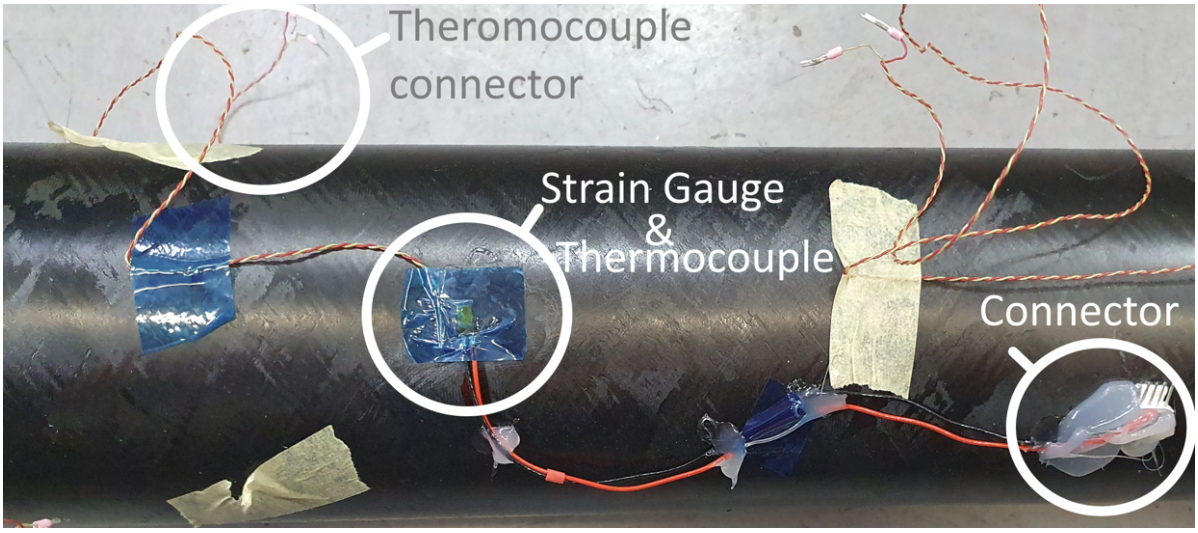

Figure 3.16: Details of the strain gauge and thermocouple with connectors on the casing of the solid rocket motor.

3.2.3. Non-dimensionalisation

Due to the confidentiality of the exact performance of the solid rocket motors of T-Minus Engineering, the burn time and pressure are non-dimensionalised. This is done by dividing for the time by dividing the time by the total burn time. And by dividing the pressure over the peak pressure of the single grain presented in Figure 2.31 as this is the maximum pressure expected when no longitudinal effects are present, will give a good overview of the effect of these longitudinal effects.

4

Verification

This chapter will verify the method and associated code by comparing intermediate results with analytical solutions and experiments.

4.1. Grain burn back

First the grain burn back model is compared to the analytical solution of a BATES grain with uniform burn rate given in Equation 4.1.

$$\begin{aligned} A_{side} &= \pi \cdot (R_{outer} - (r_{inner} + w_{burned}))^2 \\ A_{core} &= 2 \cdot \pi \cdot (R_{inner} + w_{burned})^2 \cdot (L_{grain} - w_{burned}) A \quad = A_{core} + 2 \cdot A_{side} \end{aligned} \tag{4.1}$$

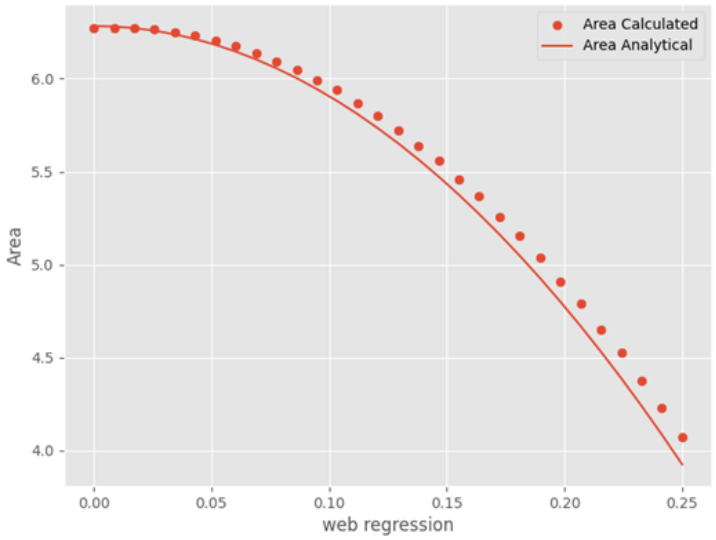

Figure 4.1: Area calculated analytically compared to the grain burn back model with a resolution of 150x450

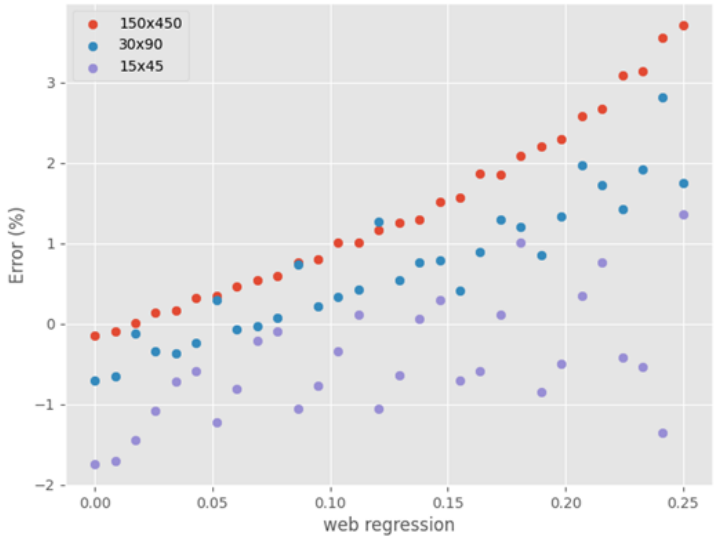

Figure 4.2: Error of the grain burn back model compared to the analytical solution for different grid sizes

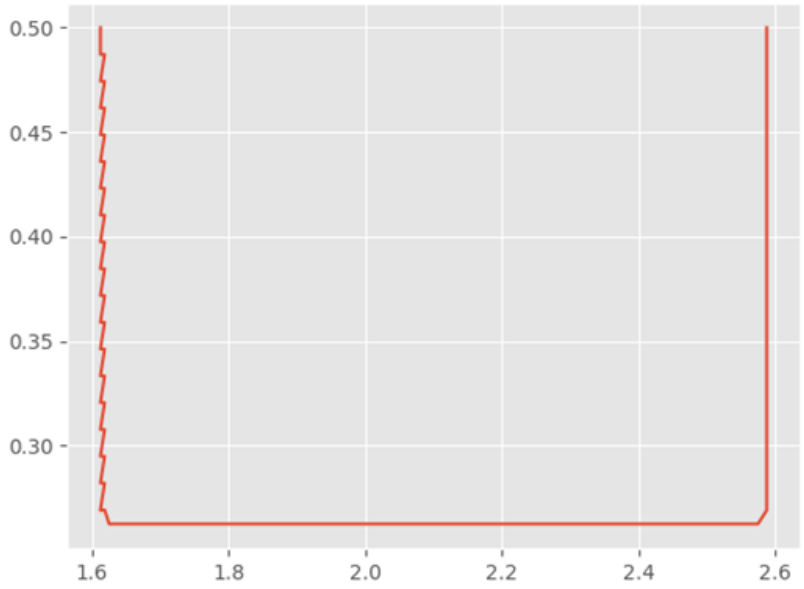

Figure 4.3: Cross section of the grain surface showing the zigzag effect exaggerated as a source of inaccuracy when increasing mesh size.

Figure 4.1 shows the error with respect to the analytical equations. It must be noted that the relative error increased as the surface regresses, this is due too the grain occupying a smaller amount of grid points and this effectively decreases the resolution. Furthermore, the error increases when the amount of mesh points increases, this is due to slight zig-zagging that occurs when there are more grid points, see Figure 4.3 where the effect is exaggerated. For the intended use a coarse mesh of about 15x45 per grain is acceptable, but it is recommended that this is reevaluated for 3 dimensional grain burn back.

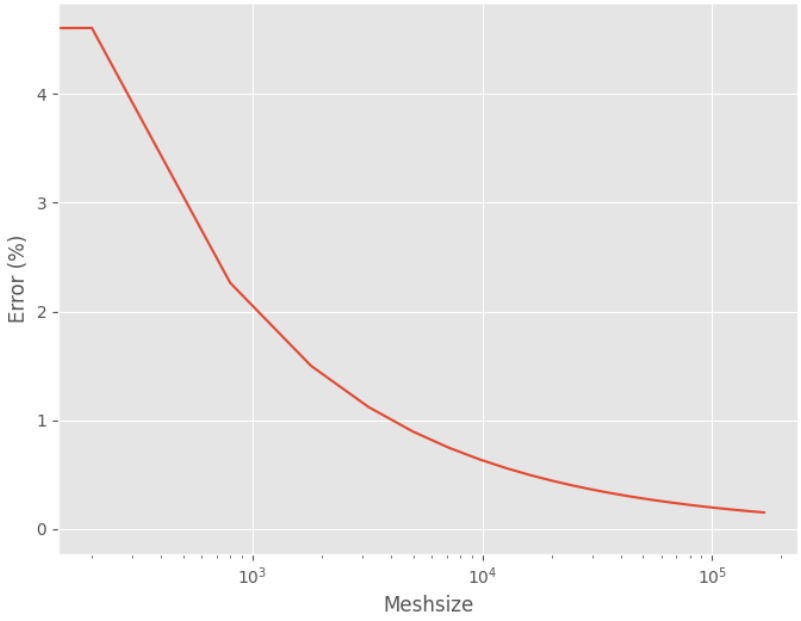

Figure 4.4: Burn area error before any surface regression versus the amount of mesh points.

Figure 4.4 shows the accuracy of the burn area when no surface regression has occurred yet. It can be seen that the error tends to zero and that for an error of below 1% a mesh size of 30x90. The mesh size along the motor must be bigger

4.2. Verification case short motor

The gas dynamics without burn rate modifiers is best validated with a short motor where the burn rate is only a function of pressure. The most standard way to do this is with a BATES (BAlistic Test and Evaluation System) grain setup, which burns at a near constant pressure to evaluate propellant performance.

In Figure 4.5 the model shows fair agreement with the experimental data, with a small undershoot in the first half of the burn and overshoot at the second half. The igniter which burns considerably hotter than the propellant could have accelerated the burn rate in the start of the burn resulting in this shift. The model does not consider the ignition in much detail as it assumes a burning/no-burning state which accelerates form no-burning to burning state form the forward closure to the nozzle.

4.3. Verification case long motor

In order to verify all the effects that are modelled a longer motor must be verified. Two cases are ran with the exact same input parameters except for geometry and throat size. The DART is shown in Figure 4.6 and in the model the initial rise up is higher due to erosive burning but then follows the pressure trace very closely and also translates into tail off at a the same time. The tail-off of the experiment is at a higher pressure and continues for slightly longer than the model predicts.

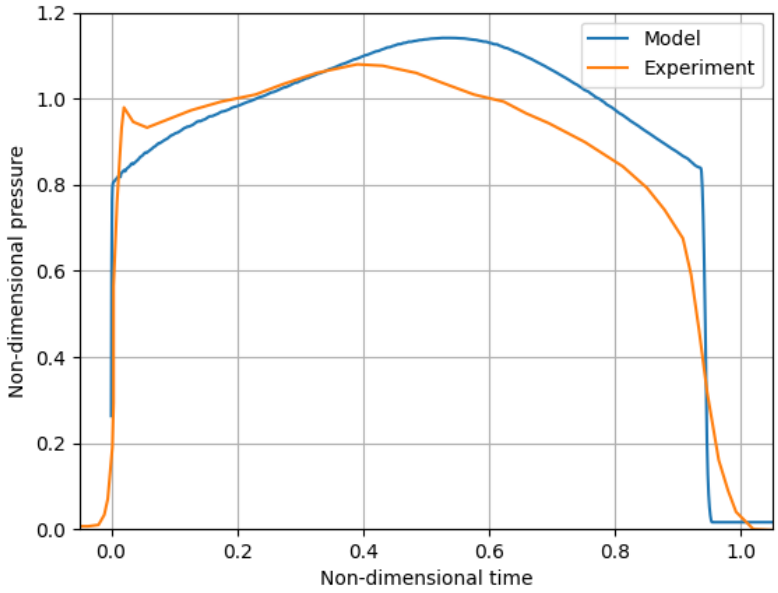

Figure 4.5: Test with a single BATES propellant segment

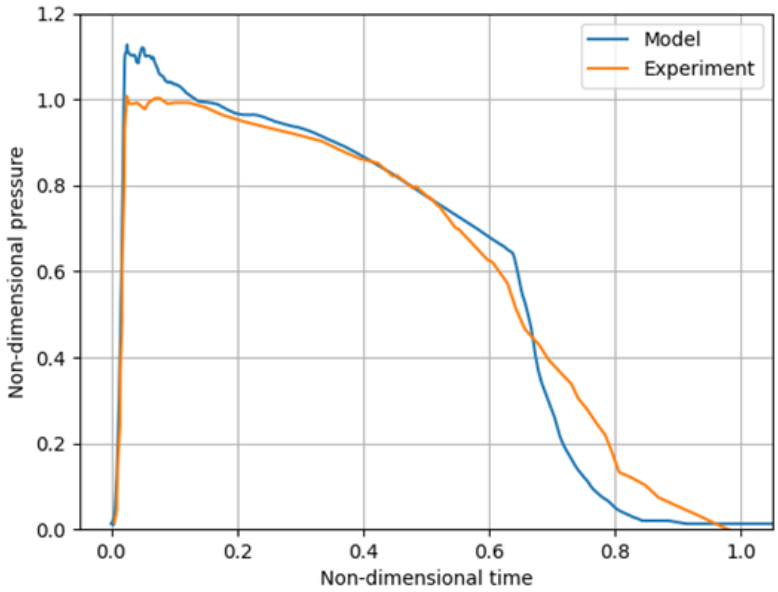

Figure 4.6: DART full scale motor comparison. Grain length over diameter ratio of 1.7.

4.4. Conclusion

The model is considered validated for the purposes of this study. As this study aims to see the effect of geometry changes especially in motors prone to erosive burning, it is important that the validation case with longitudinal effects is in agreement with the model. The model has discrepancies in the start and end of the burn, which may be significant enough to impact motor design, but are considered to be not significant to determine trends and optimal geometry properties.

5

Results

This chapter on results shows the predictions for different geometry simulations and displays the results of the longitudinal strain measurements. The geometries will show pressure traces and grain burn back for motors with different grain aspect ratios showing. The longitudinal strain measurements on the DART Full Scale Motor are shown together with the temperature at the sensors.

5.1. Grain ratio constant throat

In Figure 5.1 different grain ratios are shown in order to see what the length over diameter ratio effect is. Table 5.1 shows the aspect ratio's that were modelled. The choice for these aspect ratios was made to be around the nominal design of the DART booster. The inner diameter on the first half of the motor has a bigger diameter than the second half (near the nozzle) as this will cause the motor to burn out more evenly with erosive burning. All the aspect ratio motors shown in Table 5.1 have the same propellant mass.

Aspect Ratio	**Amount of Grains**	**Maximum Pressure (P/P_{ref})**	**Mean Pressure (P/P_{ref})**
36.0	1	1.38314	0.61696
18.0	2	1.28166	0.61553
9.0	4	1.14470	0.61375
6.0	6	1.06030	0.61308
4.5	8	1.02116	0.60689
3.6	10	1.06020	0.60654
3.0	12	1.20709	0.61781
2.57	14	1.76490	0.67857
2.25	16	2.91499	0.77369

Table 5.1: Table showing the aspect ratio and amount of grains in the DART sized booster

Figure 5.1 shows that for lower aspect ratios the pressure trace becomes more regressive and higher aspect ratios progressive. Figure 5.2 shows the effect of erosive burning the best with the maximum pressure being maximum for low aspect ratios. At higher aspect ratios the peak is in the second half of the burn and decreases until the pressure trace is mostly flat after which the maximum pressure starts rising steeply.

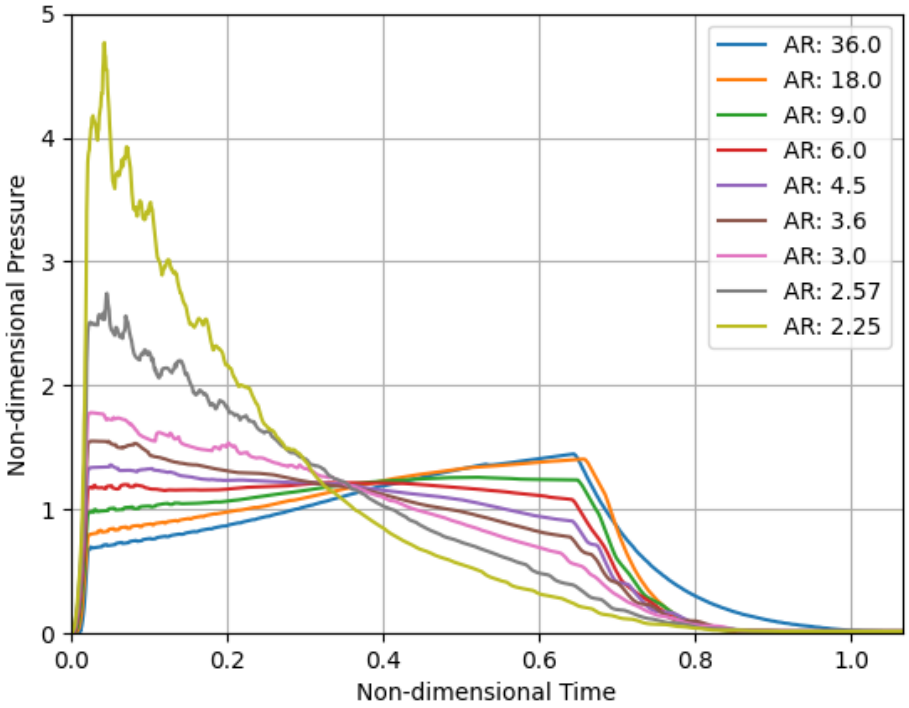

Figure 5.1: The effect of different grain ratio's on the pressure curve

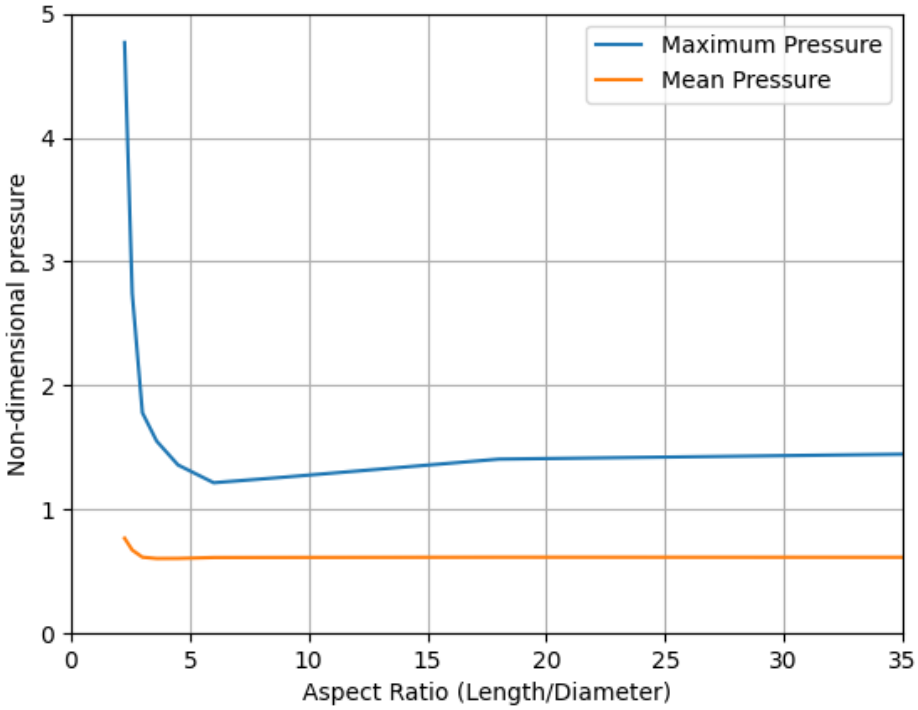

Figure 5.2: The effect of different grain ratio's on the mean and maximum pressure

5.2. Motor length constant throat

By adding grain segments and making the motor longer the effect of erosive burning is much less visible. The pressure does increase due to the increase in burning area but the erosive burning effect does not change the shape of the pressure trace as much. The main driver for this change is the change of burn area over throat area as for example more gas due to more burn area through the same throat area increases pressure.

Amount of Grains	Maximum Pressure (P/P_{ref})	Mean Pressure (P/P_{ref})
5	0.47941	0.32305
6	0.66577	0.39277
7	0.89304	0.46216
8	1.15695	0.53124
9	1.45168	0.60012
10	1.77954	0.66887
11	2.14386	0.73749
12	2.55383	0.80604

Table 5.2: Table with mean and maximum pressure for a shorter and longer engine with a constant throat area

Figure 5.3 shows the pressure traces and what can be noted in general removing grains makes the trace flatter, lower pressure and longer burn time and adding grains has the opposite effect. When looking at Figure 5.5 it shows the difference between the maximum and mean pressure rise, here it can be seen that the

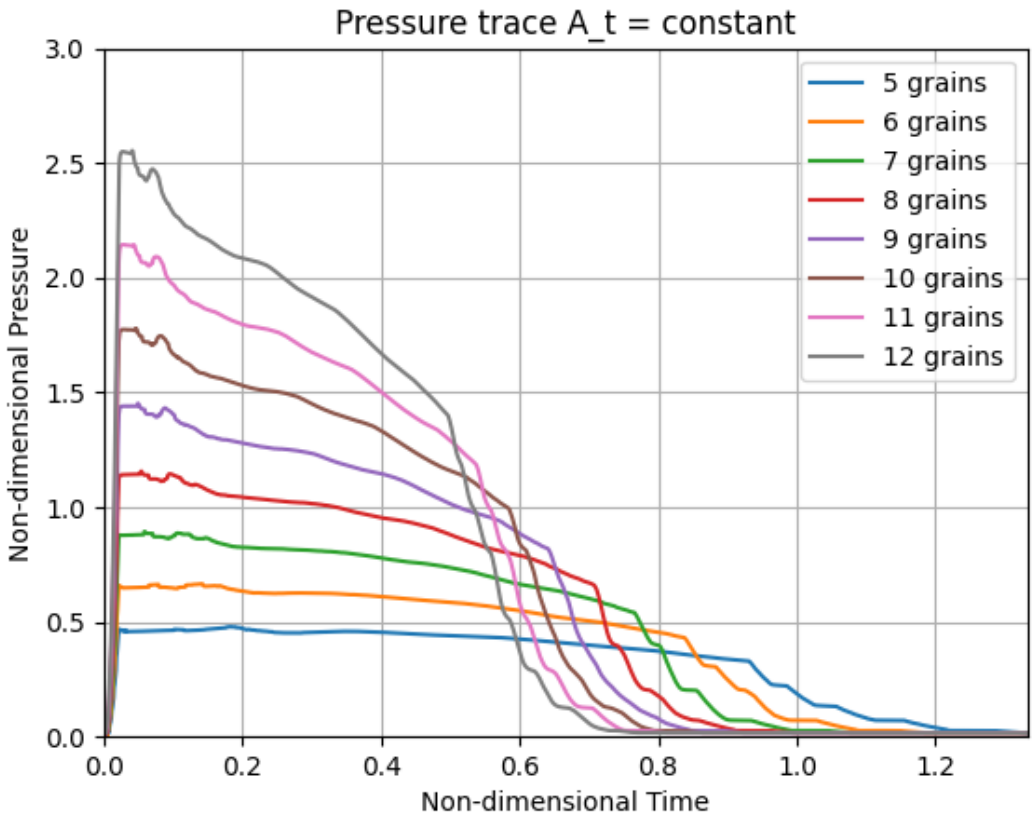

Figure 5.3: The effect of adding and removing grain segments on the pressure trace

5.3. Motor length constant burn area to throat area ratio

Different amounts of propellant segments were modelled while keeping the initial burn area over the throat area constant, also known as Klemmung. The Klemmung determined the mean pressure mostly in the study with constant throat. With a constant Klemmung, the mean pressure is almost constant. Elongation of the motor increases the mass flux in the core, which increases erosive burning causing a peak pressure at the beginning of the burn. Due to the higher burn rate during this pressure peak, the total burn time decreases and creates a longer tail-off. Figure 5.5 shows the pressure trace for different motor truncations and elongations and it can be seen here that the peak at the beginning of the burn increases and the tail elongates.

Amount of Grains	**Maximum Pressure (P/P_{ref})**	**Mean Pressure (P/P_{ref})**
5	1.19339	0.58760
6	1.23476	0.59247
7	1.28712	0.59586
8	1.36572	0.59831
9	1.45168	0.60012
10	1.54551	0.60160
11	1.64170	0.60273
12	1.74972	0.60360

Table 5.3: Table with mean and maximum pressure for a shorter and longer engine with a constant burn area over the throat area.

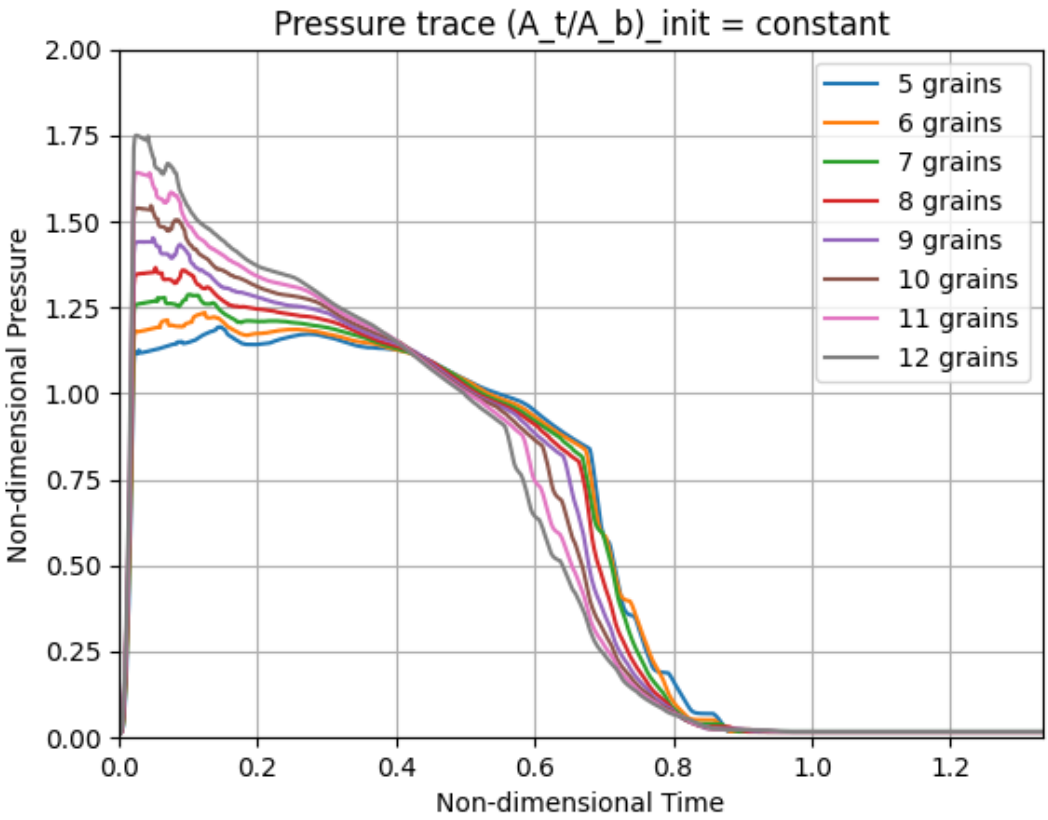

Figure 5.4: The effect of adding and removing grain segments on the pressure trace with a constant initial burn area to the throat area.

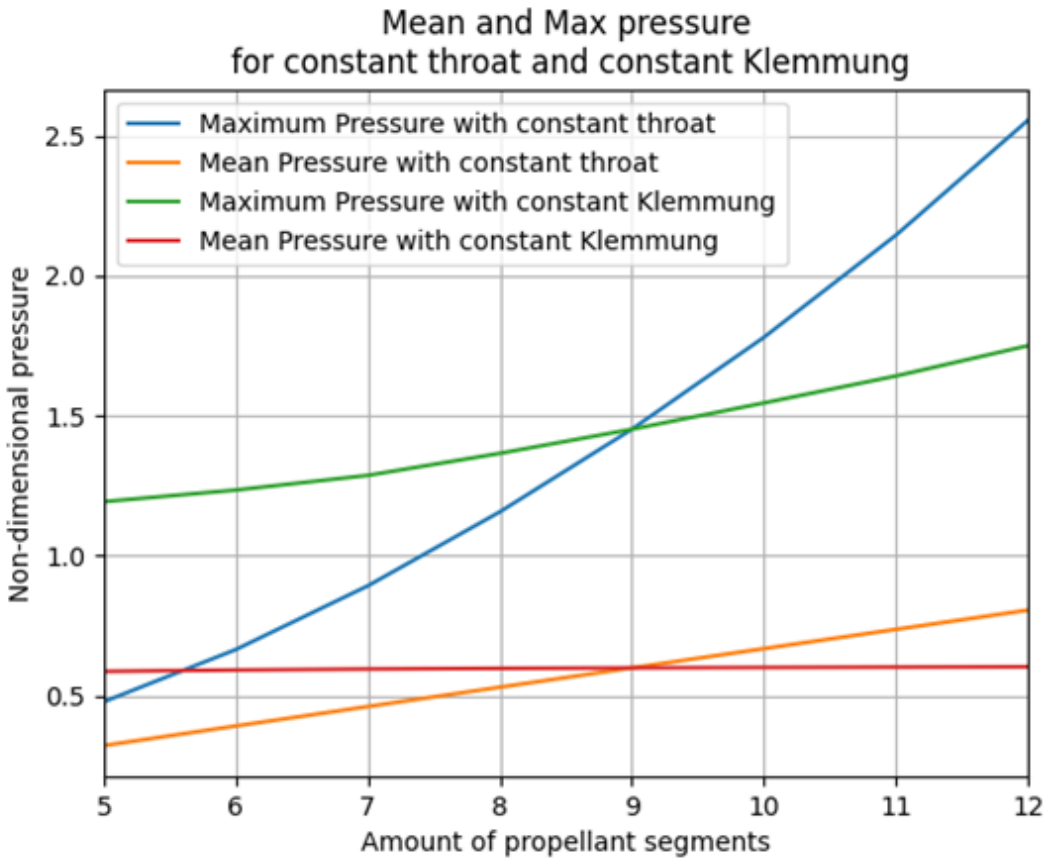

Figure 5.5: The effect of adding and removing grain segments on the mean and maximum pressure with a constant throat and constant Klemmung (initial burn area to throat area)

5.4. Experiment

This section will show the results of the tests done with strain gauges on the motor casing for both the cold and hot tests.

5.4.1. Cold hydrostatic test

The hydrostatic test showed promising results with respect to pressure measurement accuracy when increasing the pressure both along the length and perimeter strain measurements. However, during the depressurisation of the vessel, the sensors gave a negative signal that could not be physically explained. This effect can be seen in Figure 5.6 after the first peak of 100 bar the pressure sensor drops back down to zero, but the strain gauge in the hoop direction overshoots into compression. Furthermore, it can be seen that the hoop strain is 50% higher than the longitudinal strain and therefore has a better amplitude to noise ratio. The 50% instead of 100% increase for hoop strain for pressure vessels with uniform properties is explained by the non-uniformity of the carbon fibre which is stiffer in the hoop direction.

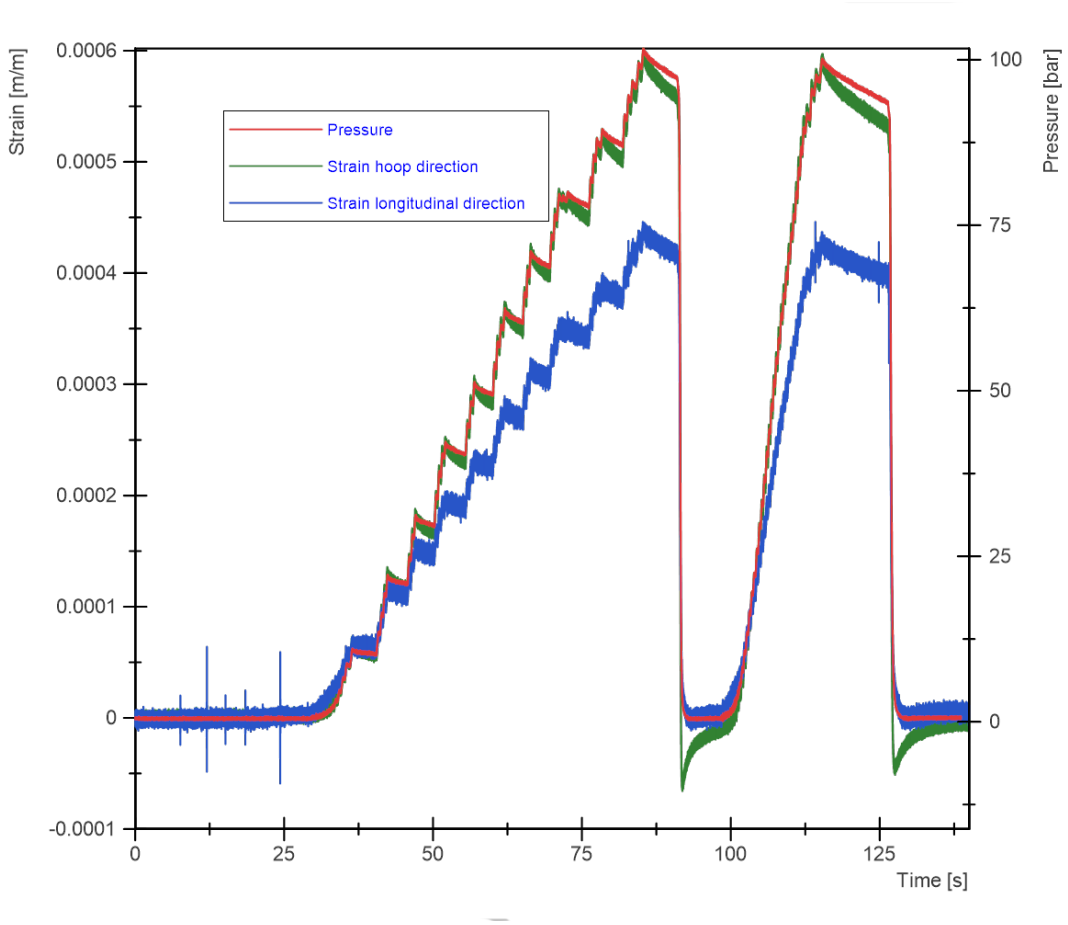

Figure 5.6: Hoop and longitudinal strain versus the pressure of the water in the chamber. The graph shows first manual pressurisation with a hydraulic pump in steps, then rapid depressurisation with a valve and lastly rapid manual pressurisation and depressurisation.

5.4.2. Hot fire 1: Regression extinguished propellant

Hot fire 1 had all the sensors attached to the motor casing, however, due to a failure in the forward closure the data was corrupted, see leakage in Figure 5.11. This meant that there was no validation data for this test approach, but it did come with the rare opportunity where the propellant was extinguished before the end of the burn. Some of this propellant was found, see Figure 5.8 and measured afterwards to find the actual regression.

Figure 5.7: Overview of the setup during hot fire, note the smoke on the side of the forward closure causing the sudden depressurisation.

Figure 5.8: Grains after the forward closure ruptured and a rapid depressurisation caused them to extinguish.

This extinguish event was very early in the burn and therefore the burning that occurred was influenced for a large part by erosive burning, this can therefore be used to verify the burn back model. In Table 5.4 these measurements are given with their locations shown in Figure 5.9.

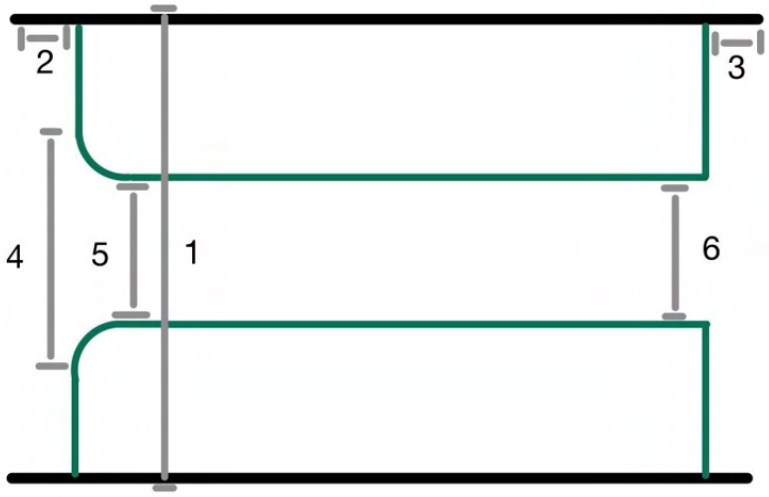

Figure 5.9: Measurement locations for the burn rate

Location	Regression Grain 7	Regression Grain 6
Position 5	-2.41 mm	-1.84 mm
Position 6	-3.3 mm	-2.9 mm
Position 2	-3.4 mm	-3.6 mm
Position 3	-3.3 mm	-3.4 mm

Table 5.4: Table showing the regression at different locations after the extinguishing of the grain

Figure 5.10 shows that the burn back of the top and bottom of the propellant segment matches well with the regression in the core. However, the divergent shape of the core is less pronounced in the burn back model than in the measured

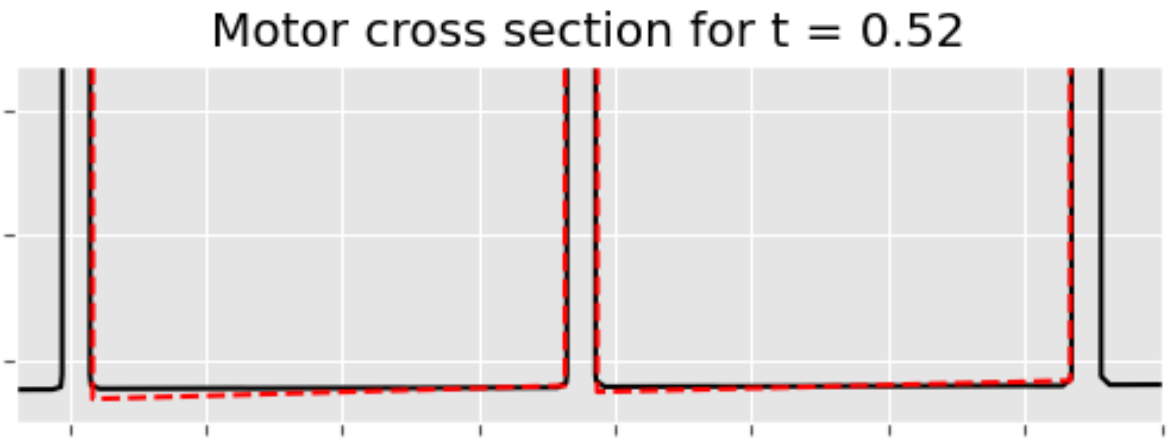

Figure 5.10: Comparison of the propellant segment in the grain burn back model and the measured extinguished segments. The red striped lines are the measured values and the black line is the modelled regression.

5.4.3. Hot fire 2: Strain over the casing

For the second hot fire, all data was collected in good order and even sound data was recorded. The pressure data are presented in non-dimensional form with the maximum operating pressure being the reference pressure. A view of the second hot fire can be found in Figure 5.11. The stain gauge closest to the nozzle was not attached well and this shows as the signal first fails to follow the expected rise up and then increases to twice the magnitude when compared to the other measurement locations. As the signal does not do its initial rise it is not plausible to be temperature-related effects.

Figure 5.11: Overview of the setup during hot fire

Figure 5.12 shows the detachment of strain gauge 4 and the contraction of the strain gauges after the burn with a bigger magnitude than due to initial pressure.

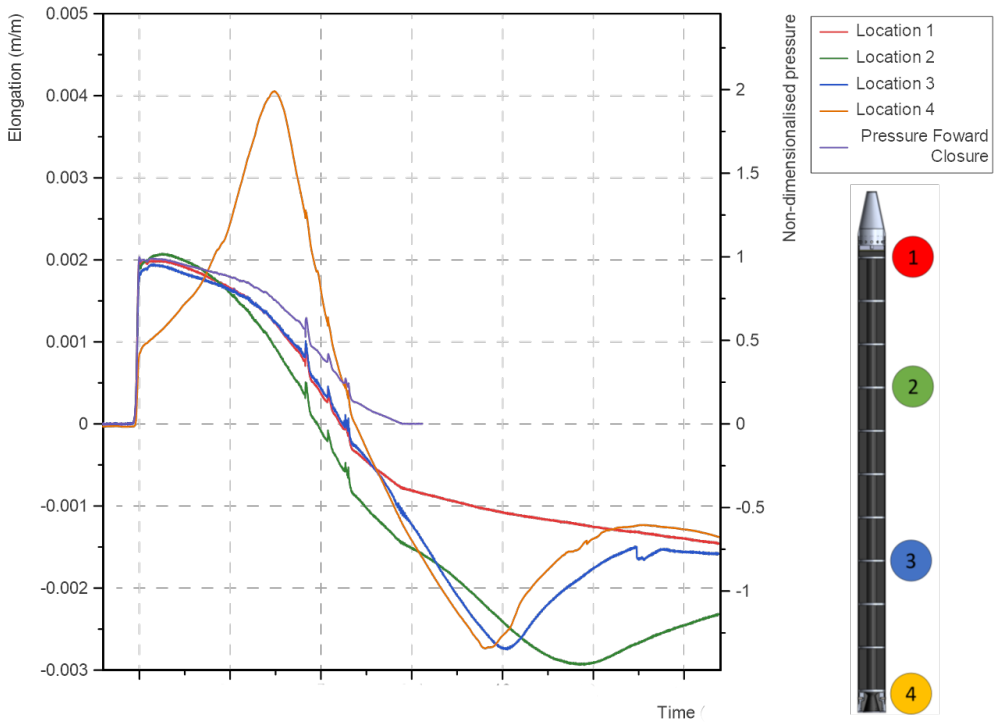

Figure 5.12: Complete response of the strain gauges including the negative signal during tail off and after the burn.

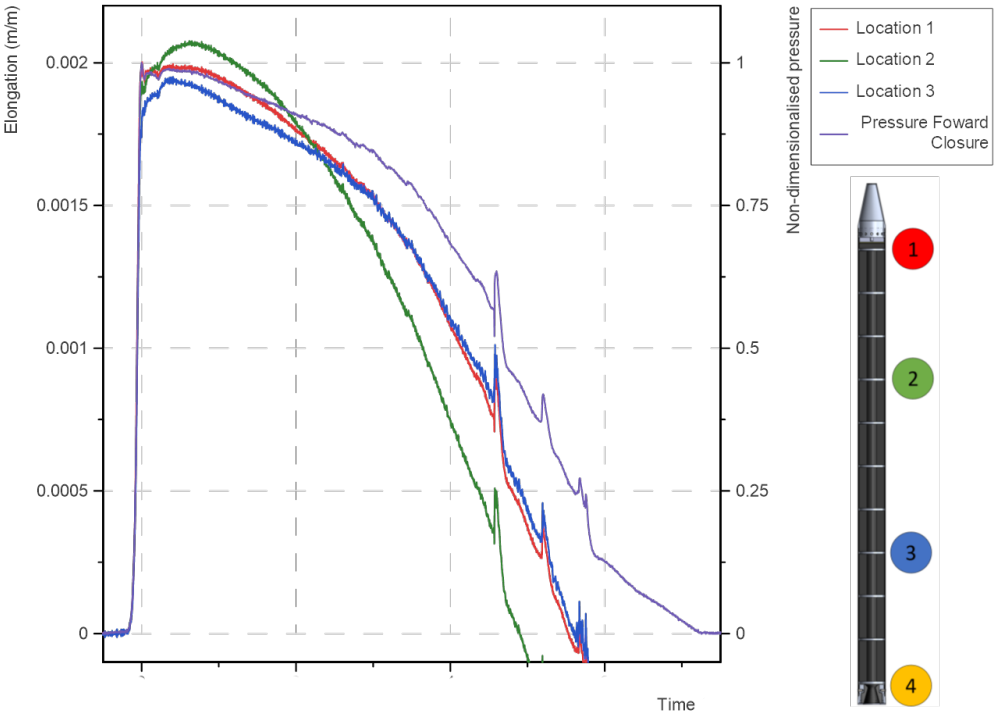

Figure 5.13: Strain measurements during the burn show the initial rise but also the local pressure spikes in the stain gauges matching in time.

Figure 5.13 shows the signal over the burn and shows the need for compensation of secondary effects to the pressure as the signal dramatically decreases. This effect does not appear to be similar nor related to temperature when the temperature data in Figure 5.15 is taken into consideration. When the signal of the pressure in the forward closure and the strain in location 1 is compared it can be seen that they diverge after 1.5 seconds.

Figure 5.14 shows that the pressure signal at the forward closure and the strain gauge at location one are in good agreement during the startup

Location **Pressure drop by Gudu et al.)**	**Length of total motor**	**Pressure drop (t=0)**	**Pressure drop (t=0.5)**
Location 1	0 %	0%	0%
Location 2	33%	4%	-3.5% (increase)
Location 3	77%	10%	2.5%
Location 4	100%	NA	NA

Table 5.5: Observed pressure drop at pressure peak and half a second after the initial peak.

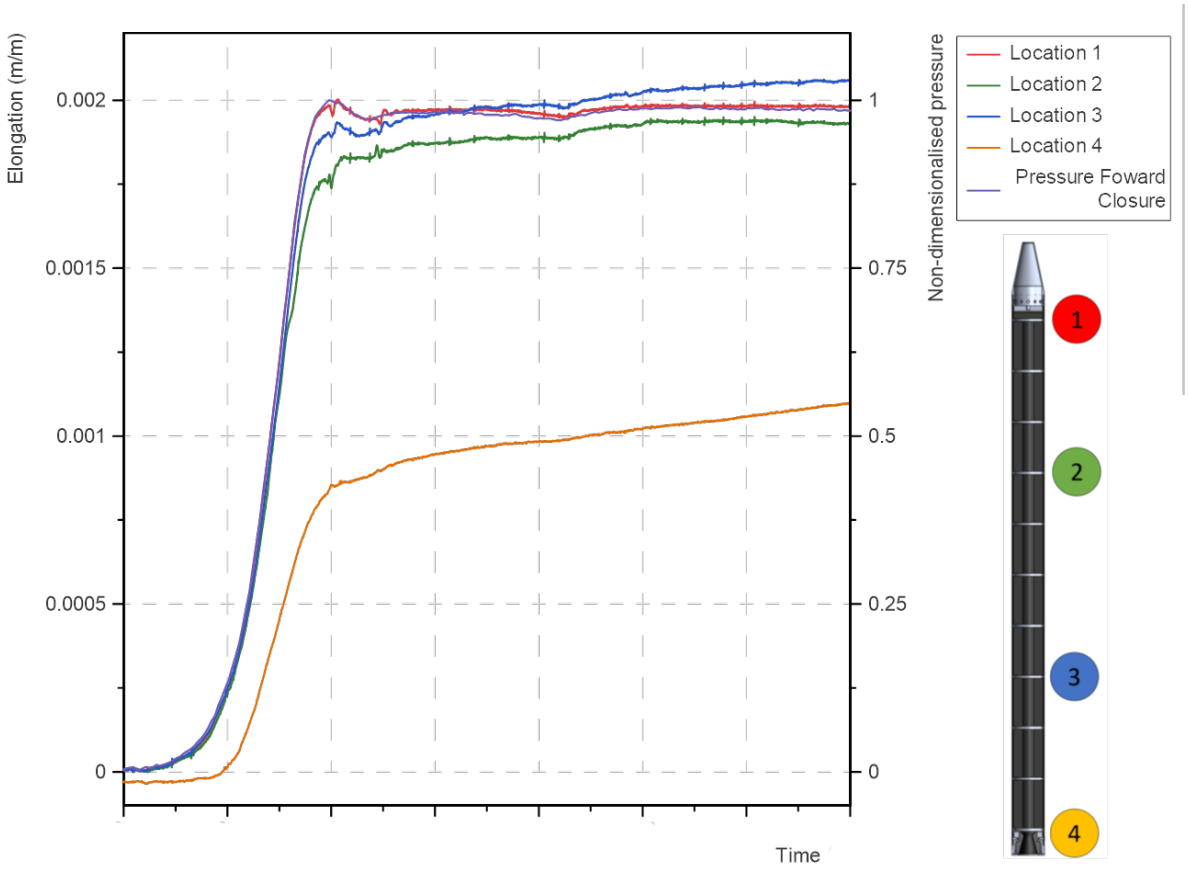

Figure 5.14: Detailed view of the strain during engine startup where the sequence of pressurisation can be seen.

Figure 5.15 shows that the temperature rise in location two is the highest and the heat in 1 and 2 is initially similar. However, when the temperature rises at location 4 where the nozzle is located this seems to influence location 3 more than location 1. All locations should be located in between propellant segments.

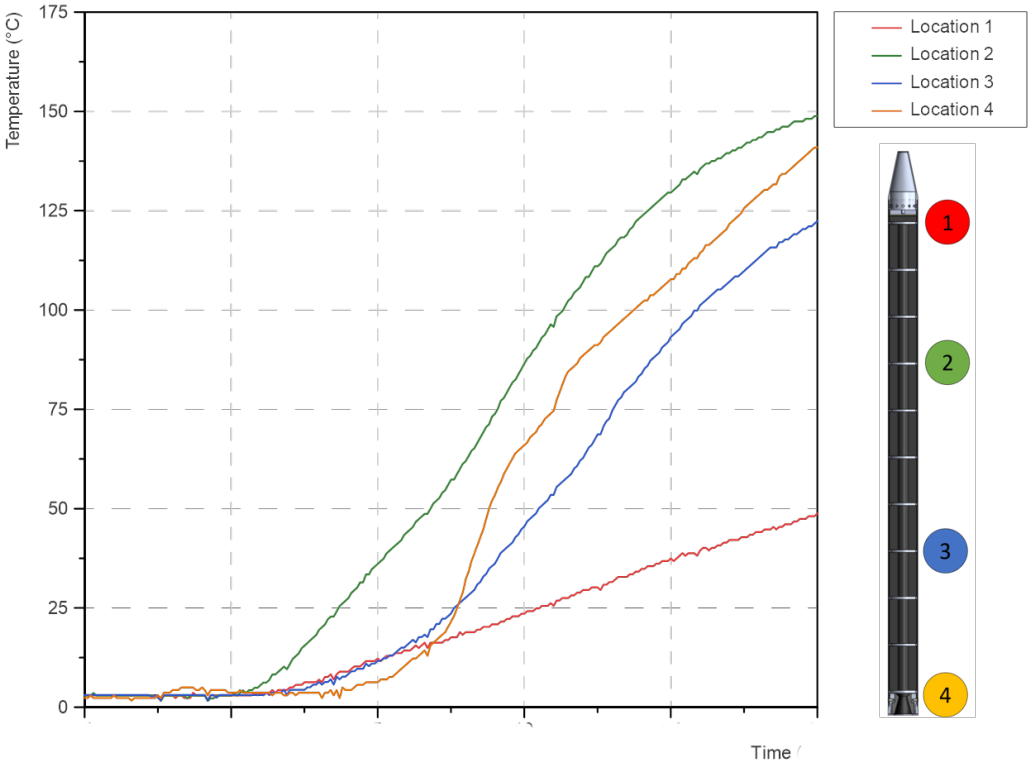

Figure 5.15: The temperature was measured at the locations along the engine length. Shows the strain gauges to themselves only reaching significant higher pressures after the first half of the burn. However, the casing heats up and expands earlier.

The expected strain by pressure was estimated by using a linear factor between the pressure measured at the forward closure and the associated peak at the beginning of the strain measurement. This gave the following correlation between temperature and strain seen in Figure 5.16. While the strain due to temperature seems similar for locations 1 and 3, the strain due to temperature of location 2 is significantly different. In addition, it must be noted that locations 1 and 2 have a similar temperature profile as can be seen in Figure 5.15 and similar strain over the burn as can be seen in Figure 5.13.

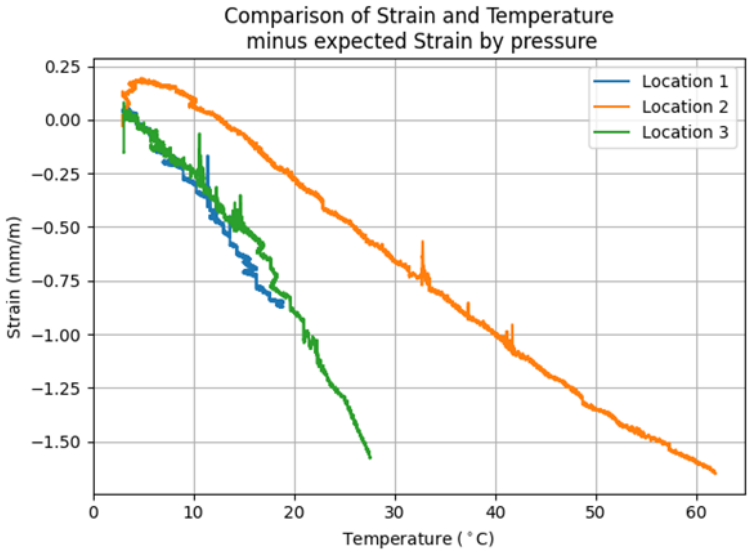

Figure 5.16: Strain versus temperature after the expected strain by pressure was subtracted.

6

Discussion

This chapter discusses the results presented before and it is structured based on the subjects approached in the previous sections. With the first three sections discussing the results of the sensitivity study on three different variables, aspect ratio in section 6.1, elongation with constant throat in section 6.2 and elongation with constant Klemmung in subsection 6.2.2. And lastly discussing the experimental results in section 6.4.

6.1. Aspect ratio

The main question on what the effect is of changing the geometry of the motor with respect to aspect ratio is mostly answered by the pressure traces shown in Figure 5.1. Very low aspect ratio's tend to have very high pressures. A lower aspect ratio for a given amount of propellant increases the initial burning surface which increases the mass flux in the core of the motor and increases the burn rate modification due to erosive burning. As both the initial burn area and the burn rate increases the chamber pressure at the start of the burn increases.

The secondary effect that erosive burning has is to make the core of the propellant segments divergent, which influences the tail-off. More erosive burning makes the core more divergent and this causes the surface to burn out more gradually and cause a more gradual longer tail off.

It is important to know when the aspect ratio is low to where runaway of the pressure occurs. As a maximum pressure that is too high will cause the casing to fail. This limits you in your design choices and dictates what size of propellant segments you can make when using several BATES configuration propellant segments. Making propellant segments or grains as big as the production facility allows can reduce logistic and production efforts on steps that need to be taken for each propellant segment or grain.

In addition, the erosive burning secondary effect has a big impact on the thrust profile tail-off, which is when the booster is at the lightest and generally highest altitude. The tail-off has a big impact on the acceleration because of low drag at high altitudes and vehicle being close empty its weight. When predicting the trajectory of rockets accurate knowledge of accelerations are needed. As changes in attitude due to wind and gravity compound over time deviate passively stabilised rockets from the desired attitude, a long tail-off can be undesirable as it can increase the spread of possible impact points.

These results are mostly bound by the specific propellant and design configuration properties. Where only the general trend would be recognisable for motors with different dimensions. But when the methodology is followed with altered properties there should be a good preliminary pressure trace. One of the biggest uncertainties is if different ignition methods are used as this ties into the biggest limitation of the model as the ignition model is very simplified and does not consider any heat or mass addition from the igniter but just ignites the surfaces at a set timing.

A limitation that is more specific to the BATES propellant segments aspect ratio is the quasi-one-dimensional approach to the flow field. As any vortexes or interactions between different segments are completely neglected effects, which for specific situations are significant and will likely change with

aspect ratio.

This initial peak can be beneficial for passively stabilised rockets that need a high tower exit velocity for their fins to be effective. At the same time, the variety in motor chamber pressure makes nozzle optimisation harder as you would want a higher pressure drop over the divergent section of your nozzle with high chamber pressure. When looking at the longer tail-off this means you have a much lower chamber pressure and this could cause the nozzle to over-expand the exhaust gas, however, this is suppressed by the decrease in atmospheric pressure in later stages of the flight.

6.2. Motor elongation truncation

On the effect that motor elongation has it matters greatly if the nozzle is kept constant or the Klemmung ($\frac{A_b}{A_t}$) is kept constant. The elongation of the motor with extra grain segments also increases the burn area which will increase the pressure in the combustion chamber. Keeping a constant ratio between the initial burn area and throat area will prevent this increase due to higher burn area, which should give a better idea of other effects like erosive burning.

6.2.1. Constant throat area

When the throat is kept at a constant area Figure 5.3shows that in general the pressure increases with more propellant segments and this decreases the burn time. The general shape of the pressure trace becomes flatter for a lower amount of grains and slanted for a higher amount of grains. This sloped pressure trace is due to the higher mass flux through the core in the first part of the burn. Fewer grains cause a smaller mass flux and this makes for a pressure trace whose shape is only dependent on burn area which for the DART booster Figure 5.3is almost flat, similar to the single grain see **??**, and is achieved in the limit when shortening the motor. This shows that for short motors the pressure trace is dependent on the Klemmung over web thickness (like shown in Figure 2.8). For all cases shown in Figure 5.3 the critical mass flux is reached during the burn and shows significant influence. This influence can be seen as stated before sloped pressure trace, but also a secondary effect of shortening the tail.

The results of propellant segments or grains shows the effect of elongating the motor by only adding or removing a segment, which is one of the cheapest modifications. This is why the effect of simple elongation or truncation with constant throat area is relevant when tailoring the thrust profile/level to a specific mission to achieve the wanted trajectory.

The results of truncation and elongation with constant area are at very different pressures and the burn coefficients for Vieille's law were not verified at these pressures which makes the burn rate uncertain. Furthermore, the ignition time is kept constant for each case so no change in the ignition stage can be modelled due to engine truncation or elongation. The combustion of aluminium in shorter engines might not be complete, in the model one of the assumptions is that the aluminium combusts completely.

6.2.2. Constant Klemmung

When the engine is truncated or elongated while changing the throat area to keep a constant Klemmung the main effect altering the pressure trace is erosive burning. The initial peak is increased which makes the propellant core more divergent which causes a longer tail-off. A longer motor with more propellant segments or grains has a higher initial pressure peak and a longer tail-off. The magnitude of this initial pressure peak increases with 6% for each grain added.

During preliminary engine design the Klemmung is free to be chosen such that the motor performs at a pressure best for the propellant performance. However, due to erosive burning not only the Klemmung determines the maximum pressure. The maximum pressure is important for the design of the motor casing, as this should withstand the maximum pressure mechanically. The maximum pressure is an important factor for the mass of the casing and therefore the empty weight of the motor, which partly determines the system performance of the entire motor.

The accuracy of the results with varying motor length for constant Klemmung depends highly on the

accuracy of the erosive burning model. This model again depends highly on an experimentally found coefficient. One of the main inputs of this model is mass flux, this property is gotten in a greatly simplified manner by taking the mass-produced from all surfaces before the point of interest and dividing this by the port area at this point. This neglects any non-homogeneity of the gas flowing through the channel, and it also assumes steady flow so no dynamic instabilities can be analysed.

6.3. Motor design

When considering these results in the motor design there is a distinction between starting from scratch or modification. The motor diameter and interfaces of the nozzle and forward closure are the most fixed, the nozzle and propellant geometry is relatively free. Without changing any of the tooling or parts the grain segments or grains can be split into segments with a lower aspect ratio. This parameter is therefore most relevant for modifications, right after elongation or truncation with constant throat area. Making changes in truncation with variable throat for constant Klemmung the best pressure can be kept, but when elongating the motor in a similar way the peak pressure increase which may require changes in the strength of the casing. The longer tail-off can be problematic for the insulation of the casing as it is exposed to the combustion gasses for a longer period of time when the tail-off starts some part of the casing insulation is exposed.

When considering the acceleration loads on a rocket it comes down to the thrust and mass, where the thrust is generally proportional to the pressure in the combustion chamber. This means that long tail-offs reduce the thrust of the rocket when the rocket is at its lightest, close to burn-out. From that perspective a long tail-off is good, in addition, a shorter burn time is also better as it decreases the number of time disturbances, like wind or gravity, which have an effect on the thrust vector. However, the efficiency of the combustion may go down when the pressure decreases.

6.4. Experiment

It was found that using strain gauges to acquire the expansion of the casing as an analogue for pressure over the length of the motor was effective when the temperature of the sensor was ambient. This can be seen from Figure 5.14 where the strain measurements show good agreement with the pressure measurements for location 1. Furthermore, the hydraulically pressurised test in Figure 5.6 showed repeatable results in good agreement with the pressure sensor. The strain measurement was found to be linearly correlated with the static pressure. As soon as the temperatures depart from ambient at t=1.5, see Figure 5.15, the agreement between the strain gauge and pressure sensor seizes, seeFigure 5.13.

At the same time, the experiment showed that during the burn the measurement of the strain gauge's resistance decreased which would be associated with compression. By looking at Figure 5.16 there does not appear to be a useful correlation between surface temperature and the decrease of the strain. Therefore, using thermocouples to compensate the signal is not sufficient. The high-frequency dynamic changes in the strain data can still be attributed to the pressure as effects seen in the pressure measurements can be seen back in the strain.

Assuming the strain is linearly correlated with pressure for the first tenth of a second of the burn. The pressure drop at 33% initially is 4% and increases to 10% at 77% of the motor with a possible further decrease in pressure next to the nozzle. This pressure drop is in the same order of magnitude as the findings form similar experiment done by Gudu[7] (2% at 33%, 6% at 77% and 10% at 100%) and some numerical work by Laubacher [54]. The pressure drop seen by Gudu is half a second later with an increase of 3.5% in pressure at 33% of the motor and a much lower 2.5% drop at 77%. As there would be no good physical explanation for this behaviour as the gas is flowing outwards which would require a pressure drop, combined with the sharp increase in temperature at location 2 it seems implausible that there is an increase in pressure.

The pressure drop over the motor can be used to determine the velocity of the gasses in the chamber. When comparing this to a model the actual pressure drop versus the theoretical can be used to determine the friction coefficient along with the motor. When the flow field is derived from the pressure drop it can be used to characterise erosive burning. Strain gauges can be a very cost-effective way to measure the pressure in the motor during motor filling. Additionally, they can show how shock waves travel through a motor like when a burst disk in the nozzle ruptures. These shock waves can also locate the source of anomalies. Strain gauges are not intrusive and can be placed on the engine

casing even on a production unit without measurement ports and therefore allow last-minute placement.

The results for pressure over the motor are only valid for the start-up. A better understanding of the error's due to temperature is needed to use this method for more than just the initial start-up. Not enough evidence is present to use this method without a pressure sensor near the throat as it was not verified at that side. Gudu [7] claimed good agreement at the nozzle after proper compensation of the temperature error, but his results show a significant shift in time for the forward closure and nozzle measurements which was not found during the experiment. The expansion of the casing with pressure depends on its stiffness which for case-bonded grains depends on the propellant geometry which is changing over time, therefore, the use of strain gauges on a casing is best used on motors where the grains are free-standing. Furthermore, the casing often has ablative layers to insulate the casing from the intense heat of the propellant when these ablate they change the stiffness of the motor changing the elongation for a given pressure which is dependent on when the flame front reaches the ablative layer.

Some modelling of the expansion due to the temperature of the casing might be needed to compensate for the error due to temperature change using the temperature from the surface as the boundary condition. Using a casing with isotropic properties is recommended as the hoop and longitudinal strain are then clearly correlated. It would also be better to use a quarter Wheatstone bridge type 2 or half Weathstone bridge type 1 as these compensate for temperature, however, the second strain gauge needs to be free of mechanically induced strain to do so which is not possible for a cylindrical pressure vessel.

It is recommended to not use a generator with an internal combustion engine but power the data acquisition system with a battery to reduce the noise by 2 orders of magnitude. And if possible hydraulically pressurise the motor before the hot fire to check the signal and adhesion of all the strain gauges.

Furthermore, placing a pressure sensor near the nozzle will allow verification of the aft-most stain gauge and give the pressure drop, an array of strain gauges can then show the profile of the pressure drop over the motor and the propagation of shock waves.

7

Conclusion

The design of multiple BATES grain motors is not often evaluated, as most motors in the industry adhere multiple grain segments to each other. Often avoiding this propellant geometry due to insulation issues and lower packing density they forgo the advantages of modularity, easy production and thrust profile control without complex core geometry. This left questions on geometry changes in the aspect ratio of propellant segments or grains and truncation or elongation when taking into account longitudinal effects like erosive burning. And as a connection to reality, test if strain gauges can be used to provide validation data for flow field models, non-intrusively without changing anything on the motor and keeping costs low?

Firstly, based on the results of a sensitivity study on aspect ratio, elongation or truncation with constant Klemmung or constant throat area. It can be said that motor elongation generally increases peak pressure and elongates the tail-off. Smaller aspect ratios have a similar effect due to erosive burning, which is amplified by their underlying regressive nature without longitudinal effects. Only by changing the Klemmung, the mean pressure changes significantly.

Secondly, by evaluating the results of the experiment done on the DART booster with strain gauges placed along the motor length. It was found only to be able to measure the pressure drop during the start-up before the surface temperature started rising. Temperature compensation was found to be non-trivial, and the system proved to be low-cost and non-intrusive. The pressure drop at 77% of the motor length at the initial pressure peak showed to be 10%.

The results for the sensitivity study are modelled using a quasi-one-dimensional gas dynamics model and two-dimensional grain burn back model. This catches erosive burning via the model proposed by Dickinson [48] with its primary effect of increased burn rate giving a higher pressure during start-up and elongated tail-off. The two-dimensional grain burn back model is important to model the tail-off as it tracks the sloped core surface due to the non-homogeneous regression speed to the gradual burn out. This approach is good for keeping track of non-homogeneous burning for decent tail-off prediction. But it simplifies the flow field and flame spreading greatly which leaves high uncertainty in the start-up and that carries on to the tail-off as it inherits the grain geometry left by the start-up.

The implication for motor design is that aspect ratio is the easiest to change, but when decreasing the aspect ratio the peak pressure becomes a factor 2 higher which becomes problematic quickly. Elongation is a different modification as it adds more propellant in addition to changing the pressure trace, here elongation with constant throat has a pressure increase much worse than when the Klemmung is constant as the Klemmung is the main factor in determining mean pressure.

The experimental work was done on one subscale hydraulically pressurised motor and two hot-fire tests at full scale. The results from the cold test showed a good linear correlation between pressure and both longitudinal and circumferential direction, with some overshoot for big negative gradients. During the first hot fire, the data acquisition failed, and the second had one of the four strain gauges detach which would suggest that the reliability of this method is insufficient for static motor tests.

As the surface temperature was seen rising in half a second at some measurement locations a proper compensation for this error is required to be able to use the magnitude of the strain. The higher frequency dynamic changes in strain can still be attributed to the change in pressure.

Comparing the results to the work from Gudu et al. [7] a much smaller delay in pressure was found between the forward closure and the nozzle, with a pressure drop in the same order of magnitude 6% and 10% at 77% of the length for Gudu et al. and the work of the author respectively. Most likely the difference is due to the highly dependent on the area of the port, however, this can not be verified as this data was not provided in the work of Gudu et al..

Since the current aspect ratio of 4 decreases in pressure slowly over the burn, a small aspect ratio increase will make the pressure trace flatter, reduce peak pressure and shorten the tail-off it is therefore recommended to increase the aspect ratio from 4 to 4.5 keeping constant chamber pressure during the majority of the burn. A big aspect ratio increase would increase the pressure over time with a peak at the end of the burn leading to an increase in acceleration loads as thrust increases with pressure and the vehicles mass decreases over time.

On using strain gauges to determine the pressure drop over a solid rocket motor, since no verification data at the nozzle was acquired further research is required in order to confidently use this technique. The technique has limited use to locate anomalies and gain insight on the pressure magnitude during start-up before the surface temperature rises.

8

Recommendations

In order to present some recommendations on improvements to the model and experiment some brief enumerations are presented below, with some explanation of what they can improve. The first recommendation would be to finish the road map presented in the introduction in Figure 1.1 starting with:

1. **Thermal compensation strain gauges** It is recommended further research is done in how to compensate for the temperature increase of the combustion chamber. A model for the potential stiffness change of the composite chamber and using a half-bridge type 1 Wheatstone bridge are good starting points. As part of the combustion chamber partially or fully loses its strength during the burn some model to compensate for this lose in strength could relate different strain levels to static pressures better. Strain gauges in the half-bridge configuration use a second unstrained gauge that is at the same temperature to compensate for the resistance change due to temperature of the first strained gauge.
2. **Model geometry in 3D** The current model can keep track of a 3D geometry, however, this makes it really slow as it requires a better designed mesh. Further research and development can be done to make the 3D grain burn back model faster by taking advantage of point symmetry of geometry and developing better algorithms for tracing burning along the motors longitudinal axis. This would enable to research the effect of internal geometry that can only be tracked in three dimensions.

Then some recommendations on the potential benefits of the experimental technique shown in section 6.4.

3. **Potential for in flight measurements** The technique is low in cost and can work with disposable hardware in a small envelope. This could have the potential to measure the pressure in the combustion chamber during a rocket launch. This potentially can help in assessing the effects of accelerations on the motor performance or rule out motor failures during anomalies.
4. **Potential for high detail startup measurements** As during the start-up the relation between pressure and strain is very concrete this makes possibilities in researching ignition behaviour for different igniters and characterise induction interval, flame spreading and chamber filling..

Lastly, the recommendations associated to the model which help improve it and show its future uses.

5. **Characterise burn rate in a broader pressure range** Currently the burn rate was characterised between 0.8 and 1.4 of the nominal peak pressure. However during the tail-off the pressure drops well below this. Due to the absence of burn rate data for these pressures the fit currently used might be off.
6. **Model pressure drop and split pressure drop and erosive burning.** Pressure drop and erosive burning effects are hard to split as they are caused by coupled flow properties. Modelling the pressure drop by adding some friction to the model and taking into account static pressure from the velocity of the gasses will give lower pressure for the flame front. At the same time, this flow usually has a higher mass flux which would increase mixing in the flame front.

Bibliography

[1] Stanley C. Solomon, Han Li Liu, Daniel R. Marsh, et al. “Whole Atmosphere Simulation of Anthropogenic Climate Change”. In: *Geophysical Research Letters* 45.3 (Feb. 2018), pp. 1567–1576. ISSN: 19448007. DOI: 10.1002/2017GL076950.

[2] Ellis M. Landsbaum. “Erosive burning of solid rocket propellants - A revisit”. In: *Journal of Propulsion and Power* 21.3 (2005), pp. 470–477. ISSN: 15333876. DOI: 10.2514/1.5234.

[3] J. Kreidler. “Erosive burning- new experimental techniques and methods of analysis”. In: *AIAA Journal* (Jan. 1964). DOI: 10.2514/6.1964-155.

[4] D. E. Coats, J. C. French, S. S. Dunn, et al. “Improvements to the Solid Performance Program (SPP)”. In: *39th AIAA/ASME/SAE/ASEE Joint Propulsion Conference and Exhibit* 39 (2003). ISSN: 2003-4504. DOI: 10.2514/6.2003-4504. URL: https://arc.aiaa.org/doi/abs/10.2514/6.2003-4504.

[5] E Cavallini, B Favini, M Di Giacinto, et al. “SRM Internal Ballistic Numerical Simulation by SPINBALL Model”. In: (). ISSN: 2009-5512.

[6] Ferruccio Serraglia. “Modeling and Numerical Simulation of Ignition Transient of Large Solid Rocket Motors”. PhD thesis. Rome: Sapienza University of Rome, 2002. URL: http://www.ingaero.uniroma1.it/attachments/874_Tesi.pdf.

[7] T. Güdü, H. Vural, and M. A. Ak. “Estimation of erosive combustion in solid propellant rocket motor by detailed strain gage measurement”. In: *33rd Joint Propulsion Conference and Exhibit*. American Institute of Aeronautics and Astronautics Inc, AIAA, 1997. DOI: 10.2514/6.1997-3108.

[8] Michael A. Willcox, M. Quinn Brewster, K. C. Tang, et al. “Solid rocket motor internal ballistics simulation using three-dimensional grain burnback”. In: *Journal of Propulsion and Power* 23.3 (2007), pp. 575–584. ISSN: 15333876. DOI: 10.2514/1.22971.

[9] M. Radzan and K. Kuo. “Erosive Burning of Solid Propellant”. In: *Fundamentals of Solid-Propellant Combustion*. Ed. by Kenneth K. Kuo. New York: American Institute of Aeronautics and Astronautics, Jan. 1984. ISBN: 978-0-915928-84-2. DOI: 10.2514/4.865671.

[10] Luigi T. DeLuca. “Highlights of Solid Rocket Propulsion History”. In: *Springer Aerospace Technology*. Ed. by Luigi T. De Luca, Toru Shimada, Valery P. Sinditskii, et al. Springer Nature, 2017, pp. 1015–1032. DOI: 10.1007/978-3-319-27748-6.

[11] K. Kuo and M. Summerfield. *Fundamentals of Solid-Propellant Combustion*. Vol. 90. AIAA, 1984. ISBN: 0915928841. DOI: 10.2514/4.865671.

[12] National Aeronautics and Space Administration. *Solid Rocket Motor Performance Analysis and Prediction NASA SP-8039*. Tech. rep. 1971. URL: http://everyspec.com/NASA/NASA-SP-PUBS/NASA_SP-8039_MAY1971_55546/.

[13] B.T.C. Zandbergen. *Thermal Rocket Propulsion (course reader AE4S01_I TUDelft)*. Tech. rep. Delft: Delft University of Technology, 2018.

[14] Loki Research. *Rocket Motors and accesories*. Aug. 2021. URL: https://lokiresearch.com/secure/storeDetail.asp?id=112020138595789.

[15] G. P. Sutton and O. Biblarz. *Rocket Propulsion Elements*. Wiley, 2016. ISBN: 9781118753880. URL: https://books.google.nl/books?id=2qehDQAAQBAJ.

[16] R. L. Geisler and C. W. Beckman. “The history of the bates motors at the air force rocket propulsion laboratory”. In: *34th AIAA/ASME/SAE/ASEE Joint Propulsion Conference and Exhibit* (1998). DOI: 10.2514/6.1998-3981. URL: https://arc.aiaa.org/doi/abs/10.2514/6.1998-3981.

[17] Richard Nakka. *Solid Rocket Motor Theory – Propellant Grain*. 2001. URL: https://www.nakka-rocketry.net/th_grain.html.

[18] National Aeronautics and Space Administration. *Solid Propellant Grain Design and Internal Ballistics NASA_SP-8076*. Tech. rep. 1972. URL: http://everyspec.com/NASA/NASA-SP-PUBS/NASA_SP-8076_42630/.

[19] Troy Prideaux. *Software, Simulations etc. - Grain-2*. URL: http://www.spl.ch/old/.

[20] Thomas D. Economon, Francisco Palacios, Sean R. Copeland, et al. “SU2: An open-source suite for multiphysics simulation and design”. In: *AIAA Journal* 54.3 (2016), pp. 828–846. ISSN: 00011452. DOI: 10.2514/1.J053813.

[21] H. G. Weller, G. Tabor, H. Jasak, et al. “A tensorial approach to computational continuum mechanics using object-oriented techniques”. In: *Computers in Physics* 12.6 (1998), p. 620. ISSN: 08941866. DOI: 10.1063/1.168744.

[22] B.V. Novozhilov. “Theory of Nonsteady Burning and Combustion Stability of Solid Propellants by the Zeldovich-Novozhilov Method”. In: *Nonsteady Burning and Combustion Stability of Solid Propellants*. 1992. Chap. 15, pp. 601–641. DOI: 10.2514/5.9781600866159.0601.0641. URL: https://arc.aiaa.org/doi/abs/10.2514/5.9781600866159.0601.0641.

[23] E. Cavallini. “Modeling and Numerical Simulation of Solid Rocket Motors Internal Ballistics”. PhD thesis. Rome: Sapienza Universita Di Roma, 2008. URL: https://core.ac.uk/download/pdf/74323997.pdf.

[24] Varada Anil Hemanth and U. S. Jyothi. “CFD Analysis of a Solid Propellant Retro Rocket Motor using Ansys Fluent”. In: *E3S Web of Conferences*. Vol. 184. EDP Sciences, Aug. 2020. DOI: 10.1051/e3sconf/202018401054.

[25] M. W. Beckstead. “An overview of combustion mechanisms and flame structures for advanced solid propellants”. In: *35th Intersociety Energy Conversion Engineering Conference and Exhibit* (2000). DOI: 10.2514/5.9781600866562.0267.0285. URL: https://arc.aiaa.org/doi/abs/10.2514/5.9781600866562.0267.0285.

[26] Merrill W. Beckstead. “Solid propellant combustion mechanisms and flame structure”. In: *Pure & Appl. Chem* 65.2 (1993), pp. 297–307. DOI: 10.1351/pac199365020297. URL: https://www.researchgate.net/publication/242235918.

[27] E.W. Price. “Combustion of Metalized Propellants”. In: *Fundamentals of Solid-Propelant Combustion*. Vol. 90. 1984, pp. 479–513. DOI: 10.2514/5.9781600865671.0479.0513. URL: https://arc.aiaa.org/doi/abs/10.2514/5.9781600865671.0479.0513.

[28] Yves Fabignon, Jean-François Trubert, Dominique Lambert, et al. “Combustion of Aluminum Particles in Solid Rocket Motors”. In: *39th AIAA/ASME/SAE/ASEE Joint Propulsion Conference and Exhibit*. July 2003. ISBN: 978-1-62410-098-7. DOI: 10.2514/6.2003-4807.

[29] T. Parr and D. Hanson-Parr. “Optical Diagnostics of Solid-Propellant Flame Structures”. In: *Solid Propellant Chemistry, Combustion, and Motor Interior Ballistics*. American Institute of Aeronautics and Astronautics, Jan. 2000, pp. 381–411. DOI: 10.2514/5.9781600866562.0381.0411.

[30] Sean P. Kearney and Daniel R. Guildenbecher. “Temperature measurements in metalized propellant combustion using hybrid fs/ps coherent anti-Stokes Raman scattering”. In: *Applied Optics* 55.18 (June 2016), pp. 44958–4966. ISSN: 0003-6935. DOI: 10.1364/ao.55.004958.

[31] F. Cauty, C. Eradès, and J.-M. Desse. “Light deviation based optical techniques applied to solid propellant combustion”. In: *Progress in Propulsion Physics*. EDP Sciences, 2011, pp. 121–134. DOI: 10.1051/eucass/201102121. URL: https://www.eucass-proceedings.eu/articles/eucass/abs/2012/01/eucass2p121/eucass2p121.html.

[32] F. Cauty. “Investigation in energetic materials combustion: A strategy for numerical simulation validation”. In: *AIAA/ASME/SAE/ASEE 42nd Joint Propulsion Conference* 5 (Jan. 2006), pp. 4177–4188. DOI: 10.2514/6.2006-4742. URL: https://arc.aiaa.org/doi/abs/10.2514/6.2006-4742.

[33] Clarke E. Hermance. “Solid-Propellant Ignition Theories and Experiments”. In: *Fundamentals of Solid-Propellant Combustion*. Vol. 90. 1984. Chap. 5, pp. 239–309. DOI: 10.2514/5.9781600865671.0239.0304. URL: https://arc.aiaa.org/doi/abs/10.2514/5.9781600865671.0239.0304.

[34] Mridul Kumar and Kenneth K Kuo. “Flame Spreading and Overall Ignition Transient”. In: *Fundamentals of Solid-Propelant Combustion*. Vol. 90. American Institute of Aeronautics and Astronautics, 1984. Chap. 6, pp. 305–360. DOI: 10.2514/5.9781600865671.0305.0360. URL: https://arc.aiaa.org/doi/abs/10.2514/5.9781600865671.0305.0360.

[35] A. Peretz, K. K. Kuo, L. H. Caveny, et al. “Starting transient of solid-propellant ocket motors with high internal gas velocities”. In: *AIAA Journal* 11.12 (1973), pp. 1719–1727. ISSN: 00011452. DOI: 10.2514/3.50676.

[36] G Uhrig, D Ribereau, A Hiss, et al. *Processing Effects on Ballistic Response of Composite Solid Propellant Grains AIAA-95-2585 Processing Effects on Ballistic Response of Composite Solid Propellant Grains*. Tech. rep. 1995.

[37] Cm Brauner, Gawtum Namah, Paul C Fife, et al. “Solid propellant combustion in striated media with application to the hump effect”. In: 1992.

[38] Gawtum Namah and Jean Michel Roquejoffre. “The ’hump’ effect in solid propellant combustion”. In: *Interfaces and Free Boundaries* 2.4 (2000), pp. 449–467. ISSN: 14639963. DOI: 10.4171/IFB/29.

[39] P. Le Breton and D. Ribéreau. “Casting process impact on small-scale solid rocket motor ballistic performance”. In: *Journal of Propulsion and Power* 18.6 (2002), pp. 1211–1217. ISSN: 15333876. DOI: 10.2514/2.6055.

[40] K. Kuo, J. Gore, and M. Summerfield. “Transient Burning of Solid Propellants”. In: *Fundamentals of Solid-Propellant Combustion*. Ed. by Kenneth K. Kuo. New York: American Institute of Aeronautics and Astronautics, Jan. 1984. ISBN: 978-0-915928-84-2. DOI: 10.2514/4.865671.

[41] Ellis M. Landsbaum. “Erosive burning of solid rocket propellants - A revisit”. In: *Journal of Propulsion and Power* 21.3 (2005), pp. 470–477. ISSN: 15333876. DOI: 10.2514/1.5234.

[42] H. S. Mukunda and P. J. Paul. “Universal Behaviour in Erosive Burning of Solid Propellants”. In: *Combustion and Flame* 109.1-2 (Apr. 1997), pp. 224–236. DOI: 10.1016/S0010-2180(96)00150-2. URL: https://core.ac.uk/download/pdf/291516212.pdf.

[43] M.K. Razdan and K.K. Kuo. “Erosive Burning of Solid Propellants”. In: *Fundamentals of Solid-Propelant Combustion*. 1984. DOI: 10.2514/5.9781600865671.0515.0598.

[44] G. Lengellé. “Model describing the erosive combustion and velocity response of composite propellants”. In: *AIAA Journal* 13.3 (1975), pp. 315–322. ISSN: 00011452. DOI: 10.2514/3.49697.

[45] Merrill K. King. “A model of erosive burning of composite propellants”. In: *Journal of Spacecraft and Rockets* 15.3 (1978), pp. 139–146. ISSN: 00224650. DOI: 10.2514/3.57298.

[46] M. K. Razdan and K. K. Kuo. “Erosive burning study of composite solid propellants by turbulent boundary-layer approach”. In: *AIAA Journal* 17.11 (1979), pp. 1225–1233. ISSN: 00011452. DOI: 10.2514/3.61303.

[47] Brian A. McDonald and Suresh Menon. “Direct numerical simulation of solid propellant combustion in crossflow”. In: *Journal of Propulsion and Power* 21.3 (2005), pp. 460–469. ISSN: 15333876. DOI: 10.2514/1.10049.

[48] L. A. Dickinson, F. Jackson, and A. L. Odgers. “Erosive burning of polyurethane propellants in rocket engines”. In: *Symposium (International) on Combustion* 8.1 (1961), pp. 754–759. DOI: 10.1016/S0082-0784(06)80569-2.

[49] Hiroshi Hasegawa, Masahisa Hanzawa, Shin Ichiro Tokudome, et al. “Erosive burning of aluminized composite propellants: X-ray absorption measurement, correlation, and application”. In: *Journal of Propulsion and Power* 22.5 (2006), pp. 975–983. ISSN: 15333876. DOI: 10.2514/1.7950.

[50] H. Kamath, R. Arora, and K. K. Kuo. “Erosive Burning Measurements and Predictions for a Highly Aluminized Composite Solid Propellant”. In: *AIAA Paper* (1982). DOI: 10.2514/6.1982-1111. URL: https://arc.aiaa.org/doi/abs/10.2514/6.1982-1111.

[51] Hein Olthof. *DART solid rocket motor final design document*. Tech. rep. T-Minus Engineering B.V, 2020.

[52] R.H. Perry, D.W. Green, and J.O. Maloney. *Perry’s Chemical Engineers Handbook*. 1999. ISBN: 9780071355407. URL: https://books.google.nl/books?id=go%5C_NjwEACAAJ.

[53] Transducer Techniques. *Wheatstone Bridge*. 2022. URL: https://www.transducertechniques.com/wheatstone-bridge.aspx.

[54] Brian A Laubacher and Von Braun Civic Center. “INTERNAL FLOW ANALYSIS OF LARGE L/D SOLID ROCKET MOTORS”. In: *Joint Propulsion Conference and Exhibit* 36 (2000). ISSN: 2000-3803.